Devices and Structures Utilizing Aerosol Jet Printing: UV Photodetectors, Transmission Lines and Ring Resonators

by

Anubha A GUPTA

THESIS PRESENTED TO ÉCOLE DE TECHNOLOGIE SUPÉRIEURE
IN PARTIAL FULFILLMENT FOR THE DEGREE OF
DOCTOR OF PHILOSOPHY
Ph.D.

MONTREAL, JULY 8TH, 2019

ÉCOLE DE TECHNOLOGIE SUPÉRIEURE
UNIVERSITÉ DU QUÉBEC

BOARD OF EXAMINERS

THIS THESIS HAS BEEN EVALUATED

BY THE FOLLOWING BOARD OF EXAMINERS

Mr. Ricardo Izquierdo, Thesis Supervisor
Department of Electrical Engineering

Mr. Sylvain G. Cloutier, Co-supervisor
Department of Electrical Engineering

Mr. Vincent Duchaine, President of the Board of Examiners
Department of Systems Engineering

Mr. Frédéric Nabki, Member of the jury
Department of Electrical Engineering

Mr. Konrad Walus, External Independent Examiner
Department of Electrical and Computer Engineering

THIS THESIS WAS PRESENTED AND DEFENDED

IN THE PRESENCE OF A BOARD OF EXAMINERS AND THE PUBLIC

ON JUNE 14TH, 2019

AT ÉCOLE DE TECHNOLOGIE SUPÉRIEURE

ACKNOWLEDGEMENTS

First and foremost, I would like to express my sincere gratitude to my supervisor Prof. Ricardo Izquierdo and co-supervisor Prof. Sylvain G. Cloutier for believing in me and giving me this opportunity. The completion of this Ph.D. would not have been possible without your guidance, motivation and knowledge. I would specially like to thank Prof. Ricardo for his encouragement, understanding and all the good conversations. I could not have imagined having a better mentor than you for my Ph.D study. This Ph.D. just not only helped me grow professionally but it also help me raise my family and build my life in this beautiful country and for that I will always remember and be grateful to you.

Beside my advisors, I would like to sincerely thanks to the rest of my thesis committee: Prof. Frédéric Nabki, Prof. Konrad Walus and Prof. Vincent Duchaine for their encouragement, time and insightful comments. I would also like to express my gratitude to the technical coordinators at UQAM and ETS laboratories who gave me access to the research facilities and training on lab equipment: Alexandre Robichaud, Gwenael Chamoulaud and Normand Gravel. Without their precious support it would not be possible to conduct this research. Everyday, I looked forward going to office because of my wonderful friends and colleagues: Shiva, Mohammad, Saurabh, Suraj, Devika, and all my other friends in Montreal. It would not be possible to be efficient all these years without your love and support.

Special thanks to my family: my parents, my grandparents, my brother and sister and my parents-in-law for supporting and encouraging me throughout this thesis and my life in general. I would specially like to thank my parents and my sister who took out precious time out of their lives at the birth of my son. They helped me take care of my son so that I could go to work everyday and complete my thesis. I could never thank them enough. I would also like to mention my son, Anay who made this success much more worthwhile. Last but not the least, I would like to thank my best friend, my mentor, my husband and to the best father, Michiel Soer. You are my biggest support. I dedicate this thesis to you.

Thanks for all your encouragement!

DISPOSITIFS ET STRUCTURES UTILISANT L'IMPRESSION PAR JET D'AÉROSOL: PHOTODÉTECTEURS UV, LIGNES DE TRANSMISSION ET RÉSONATEURS À ANNEAU

Anubha A GUPTA

RÉSUMÉ

Le marché de l'électronique imprimable est en croissance constante. Grace au procédé de fabrication peu coûteux, la faisabilité sur de grandes surfaces et le temps de traitement court, l'électronique imprimable reste très prometteuse pour les chercheurs, même si ses performances sont inférieures à celles de l'électronique conventionnelle. Certaines technologies d'impression telles que la sérigraphie et l'impression à jet d'encre sont déjà bien établies. Cependant, la technique d'impression en aérosol à méso-échelle sans masque promet des avantages uniques. En effet, cette technique permet l'impression directe de structures 2D-3D plus fines, et ce en utilisant une large gamme de matériaux de viscosité comprise entre 1 et 1000 cP. De plus, elle permet de résoudre le problème récurrent de l'obturation des buses. Cependant, l'utilisation de l'électronique imprimable pour la fabrication de composantes électroniques grand public reste un défi et les performances des dispositifs ainsi fabriqués doivent encore être améliorées. De nouvelles techniques telles que l'impression par jet d'aérosol nécessitent des recherches supplémentaires afin de remplir leurs promesses. Cette thèse aborde la problématique de la fabrication de composantes entièrement par impression et ce en utilisant la technique de jet par aérosol. Ceci a été réalisé en se concentrant sur des dispositifs pour les domaines de l'optoélectronique et de l'empaquetage pour les semi-conducteurs.

Les composants et le mécanisme de fonctionnement du système d'impression par jet d'aérosol sont décrits et une méthodologie pour l'optimisation du processus est proposée. Quatre régions distinctes pour l'optimisation des processus sont identifiées soit: L'identification de l'encre, le traitement de surface, le contrôle du processus et le post-traitement. Dans les travaux préliminaires, les possibilités du contrôle du processus d'impression par jet d'aérosol sont explorées, telles que la largeur de trait réalisable, l'épaisseur du film, la compatibilité des matériaux et les possibilités de frittage. Des structures de test sont produites afin de tester le flux de fabrication et d'observer l'interaction et la compatibilité des matériaux des multiples couches imprimées. Les défis associés à l'impression par jet d'aérosol sont identifiés, notamment le mouillage, l'alignement, la surpulvérisation et le dépôt de structures satellites.

Un photodétecteur ultraviolet entièrement imprimé avec une architecture nanoporeuse est étudié, lequel profite de la rugosité de surface du film semi-conducteur imprimé par jet d'aérosol. Les cristaux d'oxyde de zinc pré-synthétisés sont imprimés pour réduire la température de post-recuit. À une température < 150 °C, le solvant est évaporé, ce qui donne une structure poreuse présentant un rapport surface / volume élevé. Un photodétecteur entièrement imprimé présentant des performances comparables à celles de l'état de l'art est démontré, alors que le processus de fabrication à basse température maintient la compatibilité avec les substrats plastiques flexibles de grande surface.

Par la suite, une ligne de transmission microruban entièrement imprimée en utilisant le SU-8 comme diélectrique et argent comme conducteur est proposée. Cette approche peut fournir des interconnexions à large bande passante à l'intérieur des boitiers des matrices semi-conductrices. Les matériaux métalliques et diélectriques sont caractérisés à des fréquences micro-ondes allant jusqu'à 18 GHz. Il est montré qu'une bonne correspondance est atteinte entre les paramètres simulés et la structure imprimée, ce qui indique une bonne adaptation d'impédance caractéristique et à de faibles pertes de transmission. La transition de la ligne de transmission imprimée vers un circuit intégré à micro-ondes est démontrée, validant ainsi le concept de lignes de transmission imprimées par jet d'aérosol à l'intérieur du boitier.

Enfin, les lignes de transmission imprimées à base de SU-8 sont développées dans des résonateurs en anneau à micro-ondes qui ont des applications dans la détection à haute fréquence. Il est envisagé d'imprimer directement ces structures à l'intérieur du boitier, directement connectées à un amplificateur intégré à micro-ondes pour une détection à Q élevé. Par conséquent, ces résonateurs en anneau sont conçus pour des fréquences centrales hyperfréquences allant de 15,5 à 21,5 GHz pour des tailles réduites pouvant être intégrées à l'intérieur d'un boîtier. La caractérisation des matériaux métalliques et diélectriques s'effectue jusqu'à 26 GHz. Les résultats simulés ont montré une bonne correspondance avec les résultats mesurés en termes de fréquence centrale, de perte d'insertion, de facteur Q et de rejet hors bande.

Mots-clés: Électronique imprimée, Entièrement imprimée, Optoélectronique, Emballage, Jet d'aérosol, Photodétecteur UV, Lignes de transmission, Résonateurs en anneau.

DEVICES AND STRUCTURES UTILIZING AEROSOL JET PRINTING: UV PHOTODETECTORS, TRANSMISSION LINES AND RING RESONATORS

Anubha A GUPTA

ABSTRACT

The market for printed electronics is growing continuously. Its low-cost fabrication process, large-area scalability and short processing time makes it interesting for researchers, even though the performance is lower as compared to conventional electronics. Popular printing technologies such as screen printing and inkjet printing are well established, but the upcoming maskless meso-scaled aerosol printing technique promises unique advantages. It allows the direct printing of finer 2D-3D structures, using a wide range of materials with viscosity between 1-1000 cP, while resolving the exhaustive problem of nozzle clogging. However, the implementation of printed electronics in consumer electronics remains a challenge, as device performance has to be improved. New techniques such as aerosol jet printing require additional research to fulfill their promise. This thesis investigates the implementation of fully printed structures using aerosol jet printing, focusing on devices in the fields of optoelectronics and semiconductor packaging.

The system components and operation mechanism of the aerosol jet printing system are described and a methodology for process optimization is proposed. Four distinctive regions for process optimization are identified: ink selection, surface treatment, process control and post-processing. In the preliminary work, the possibilities of the aerosol jet printing process control is explored, such as achievable line width, film thickness, material compatibility and sintering possibilities. Test structures are produced in order to test the fabrication workflow, and to observe the interaction and compatibility of multiple printed layers. The challenges associated with aerosol jet printing are identified, including wetting, alignment, overspray and satellite deposition.

A fully printed ultraviolet photodetector with a nanoporous morphology is investigated. Pre-synthesized Zinc Oxide crystals are printed to reduce the post-annealing temperature. At a temperature of $< 150\ ^\circ$C, the solvent is evaporated, resulting in a porous structure having high surface area-to-volume ratio. A fully printed photodetector that has comparable performance to the state-of-the-art is demonstrated, while the low-temperature fabrication process maintains compatibility with large area flexible plastic substrates.

Next, a fully printed microstrip transmission line with SU-8 as dielectric and silver as conductor is proposed, which can provide high-bandwidth interconnections in packaged semiconductor dies. The metal and dielectric materials are characterized at microwave frequencies upto 18 GHz. It is shown that a good correspondence is reached between the simulated design parameters and the printed structure, which results in good characteristic impedance matching and low transmission losses. The transition of the printed transmission line to a microwave integrated circuit is demonstrated, thereby validating the concept of aerosol jet printed transmission lines inside the package.

Lastly, the SU-8 based printed transmission lines are extended into microwave ring resonators, with applications in high frequency sensing. It is envisioned to directly print these structures inside the package, directly connected to a microwave integrated amplifier for high-Q sensing. Therefore, these ring resonator are designed for microwave center frequencies ranging from 15.5 to 21.5 GHz for reduced size which can be integrated inside a package. The material characterization of metal and dielectric materials are carried out up to 26 GHz. The simulated results showed good correspondence with the measured results in terms of center-frequency, insertion loss and Q-factor.

Keywords: Printed electronics, Fully printed, Optoelectronics, Packaging, Aerosol Jet, UV-Photodetector, Transmission lines, Ring resonators

TABLE OF CONTENTS

LIST OF TABLES

LIST OF FIGURES

Page

LIST OF ABREVIATIONS

2D	Two dimensions
3D	Three Dimensions
AFM	Atomic Force Microscopy
Ag	Silver
AJ	Aerosol jet
AJP	Aerosol Jet Printing
Al	Aluminium
ASIC	Application-specific integrated circuit
Au	Gold
CAD	Computer Aided Design
CMOS	Complementary Metal-Oxide-Semiconductor
COB	Chip-On-Board
CPW	Co-planar waveguide
DI	Deionized
DNA	Deoxyribonucleic acid
DRS	Diffused reflectance spectroscopy
DXF	Drawing Exchange Format
FR	Focusing Ratio
Ga_2O_3	Gallium(III) Oxide

HFSS	High Frequency Electromagnetic Field Simulation
HMDS	Hexamethyldisilazane
ICs	Integrated Circuits
In_2O_3	Indium Oxide
$InGe_2O_7$	Indium Germanate
IoT	Internet of things
IPA	Isopropyl alcohol
IR	Infrared
ITO	Indium tin oxide
IV	Current–voltage
LTCC	Low Temperature Co-Fired Ceramic
MIDs	Moulded interconnect devices
MMIC	Monolithic Microwave Integrated Circuit
(M^3D)	Maskless Mesoscale Material Deposition
MS	Microstrip
MSM	Metal-Semiconductor-Metal
N_2	Nitrogen
NIR	Near infra red
NSERC	Natural Sciences and Engineering Research Council
O_2	Oxygen

OLEDs	Organic light emitting diodes
OPDs	Organic photodetectors
OSCs	Organic solar cells
OTFTs	Organic thin film transistors
P3HT	Poly(3-hexylthiophene-2,5-diyl)
PA	Pneumatic Atomizer
PCB	Printed Circuit Board
PCBM	Phenyl-C61-butyric acid methyl ester
Pd	Pallidium
PEDOT:PSS	Poly(3,4-ethylenedioxythiophene) Polystyrene sulfonate
PET	Polyethylene terephthalate
PTFE	Polytetrafluoroethylene
PMMA	Poly(methyl methacrylate)
PS-PMMA-PS	Poly(styrene-block-methylmethacrylate-block-styrene)
Pt	Platinum
PVA	Polyvinyl alcohol
PVP	Polyvinylpyrrolidone
Q	Quality Factor
QD	Quantum Dot
QFN	Quad-flat no-lead

R	Responsivity
ReSMiQ	Microsystems Strategic Alliance of Québec
RF	Radio Frequency
RFID	Radio-frequency identification
RMS	Root Mean Square
RP	Rapid prototyping
SEM	Scanning Electron Microscopy
SiO_2	Silicon Dioxide
SiP	System in package
SMA	SubMiniature version A
SnO_2	Tin(IV) Oxide
SOLT	Short Open Load Through
SRR	Split ring resonator
SU-8	Transmission Line
TL	Transmission Line
UA	Ultrasonic Atomizer
UV	Ultraviolet
VI	Virtual Impactor
VNA	Vector Network Analyzer
ZnO	Zinc Oxide
$Zn(NO)_3.6H_2O$	Zinc Nitrate Hexa Hydrate

LIST OF SYMBOLS AND UNITS OF MEASUREMENTS

dB	Decibel
M	Molar
pF	Pico Farad
nm	Nano meter
GHz	Giga Hertz
nH	nano Henry
Ω	Impedance
I_{ph}	Photocurrent
P_{opt}	Optical Power
Hz	Hertz
pA	pico Ampere
uW	micro Watt
mW	milli Watt
Z_O	Characteristic Impedance
ε_r	Relative Permittivity
um	Micrometer
^oC	Degree Celcius
sccm	standard cubic centimeters per minute
cP	CentiPoise

INTRODUCTION

Introduction to Printed Electronics

Traditionally, ’printing’ refers to pattern generation by the application of ink formulations. The simplest examples of printing are books, magazines, newspapers, textiles and labels. These are low-cost processes because of the widely used substrates such as paper, plastic and cloth. With the advancement of technology, the ability to print functional materials instead of just colored inks has led to the emergence of ’printed electronics’. In this paradigm, standard printing methods are used to build electrical devices by depositing functional materials, such as conducting, dielectric and semiconducting inks onto the substrate in successive layers, thereby forming active and passive devices.

In comparison to conventional electronics, some of the primary benefits of printed electronics are as follows:

- Digital-write techniques allow rapid prototyping by direct translation of Computer Aided Designs (CAD) into printed structures. The avoidance of intermediate steps, such as mask designing, vacuum processing and lithography can result in much shorter lead-times.
- Setting up a printing facility is orders of magnitude less expensive than building a silicon foundry. A printing facility requires a series of printers to facilitate fabrication of multi-layered structures in addition to pre- and post-treatment equipment. Printing does not necessarily require an inert atmosphere or a clean room facility to operate. Moreover, in additive printing the manufacturing cost is substantially lower due to reduced material waste.
- The recent advancement in the field of nanomaterials has led to the development of high-performance inorganic and organic functional inks. These inks can be post-cured at much

lower temperatures or by radiation exposure. This prevents the damaging of the substrate. Also, the use of radiation allows uniform and large scale curing, at a reduced curing time.

- The ability to print on recyclable, thin, lightweight and flexible substrates opens up new application areas. Flexible substrates allow the building of electronic circuits on curved surfaces. The use of flexible substrates instead of using hard and brittle substrates imparts robustness to the devices. Also, roll-to-roll printing allows the scalability of a manufacturing process to very large areas.

Many products using printed electronics are already available in the market. Roll-to-roll printing techniques such as gravure printing and screen printing have been used for a long time for the production of passive components, like capacitors, resistors, inductors and antennas. For hybrid integration, printing has been combined with silicon technology to reduce the cost of the complete manufacturing process. Screen and inkjet printing have been used to print grid lines for solar cells, batteries, smart labels, and RFID tags. Currently, ultra-fast rotary screen printing is being used in interconnect technology for soldering and wiring.

The future looks bright for printed electronics, with a projected compound annual growth rate of 14.9% per year (Markets and markets, 2018). According to IDTechEx analyst forecasts, the combined market for printed, flexible and organic electronics will grow from 31.7 billion \$ in 2018 to 77.3 billion \$ in 2029 (IDTechEx Research, 2018). The main market for printed electronics is likely to be found in low-end devices with ultra-low fabrication cost (Sondergaard *et al.*, 2013; Lupo *et al.*, 2013). Major emerging applications are expected in the field of microelectronics, medical, photonics, packaging and wearables. The prospects of large area scalability, environmentally friendliness, low weight, and flexibility in printed electronics generates a broad interest in both industry and research.

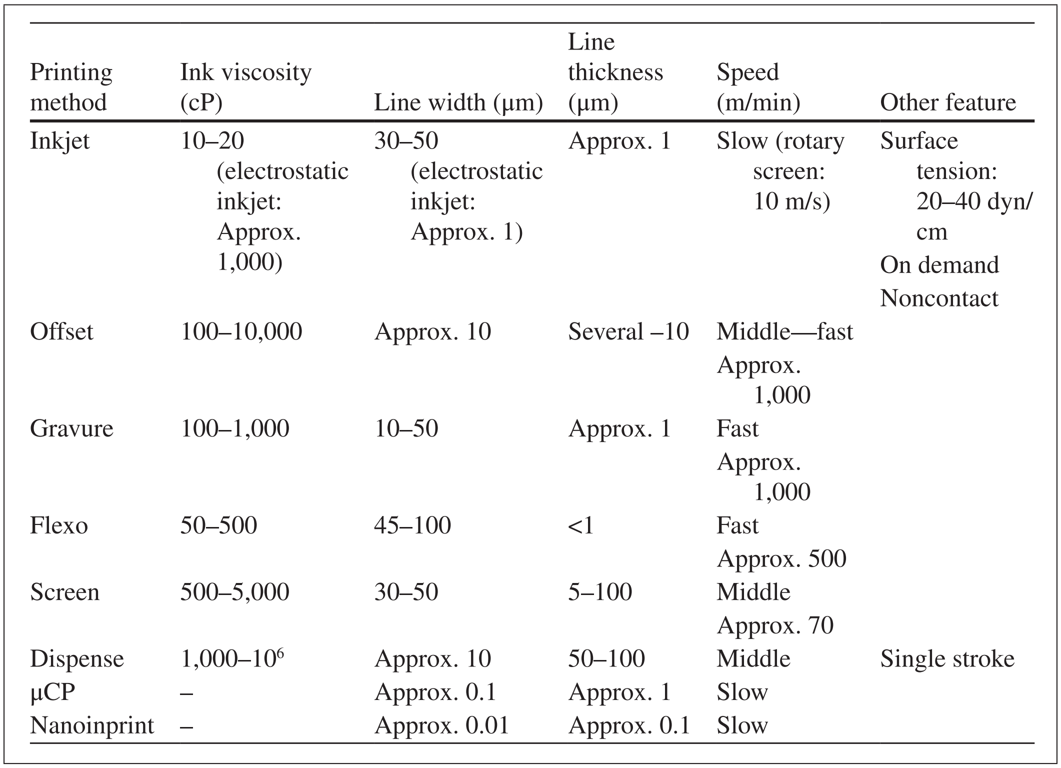

Printing method	Ink viscosity (cP)	Line width (μm)	Line thickness (μm)	Speed (m/min)	Other feature
Inkjet	10–20 (electrostatic inkjet: Approx. 1,000)	30–50 (electrostatic inkjet: Approx. 1)	Approx. 1	Slow (rotary screen: 10 m/s)	Surface tension: 20–40 dyn/cm On demand Noncontact
Offset	100–10,000	Approx. 10	Several –10	Middle—fast Approx. 1,000	
Gravure	100–1,000	10–50	Approx. 1	Fast Approx. 1,000	
Flexo	50–500	45–100	<1	Fast Approx. 500	
Screen	500–5,000	30–50	5–100	Middle Approx. 70	
Dispense	1,000–10^6	Approx. 10	50–100	Middle	Single stroke
μCP	–	Approx. 0.1	Approx. 1	Slow	
Nanoinprint	–	Approx. 0.01	Approx. 0.1	Slow	

Figure 0.1 Comparison between printing methods
Suganuma (2014)

Printing Technologies

In the last few decades, there have been significant developments in the field of printed electronics. Industries are mostly interested in developing roll-to-roll process for high-speed production over large surfaces. A wide range of printing methods are available, with a few key technologies being screen printing, gravure printing, flexo printing and offset printing. The choice of method depends on a lot of factors, such as pitch resolution, thickness, ink compatibility with system components, substrate and uniformity. A comparison of printing parameters of different technologies is shown in Figure 0.1. Whereas, Figure 0.2 shows the current state of pitch resolution that can be achieved using different printing methods.

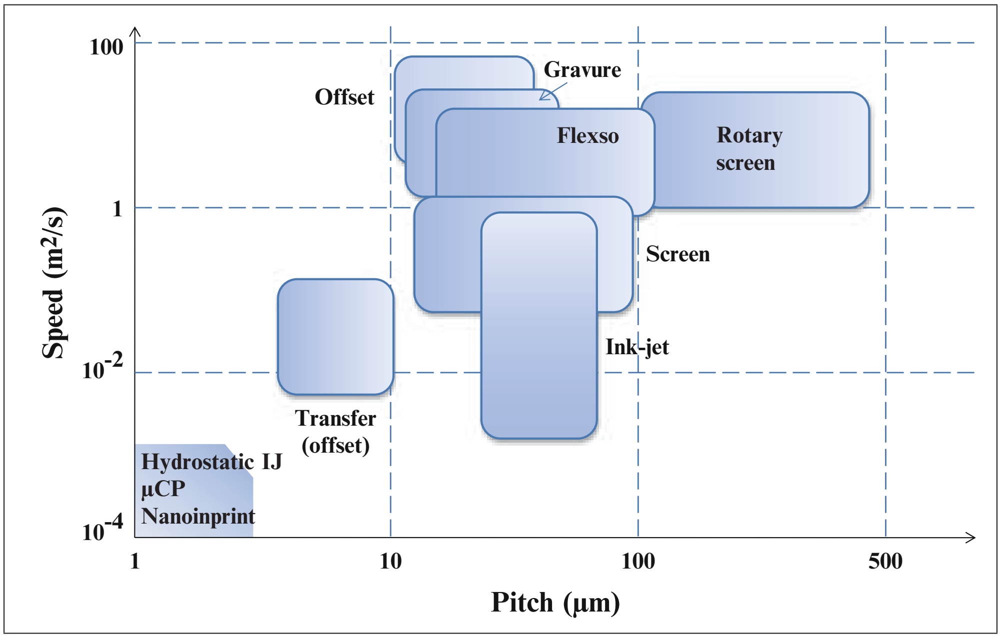

Figure 0.2 Comparison of resolution achieved using different printing methods Suganuma (2014)

Screen, flexo and gravure printing are the most commonly used printing methods for mass-production. Screen printing (flatbed or rotary) is ideal for commercial applications, where the thickness of printed conductive and dielectric layers is more important than the resolution. It is capable of printing layers more than 100 μm thick in a single trace, but is not ideal for thin coatings. For mass-production, the pitch resolution of screen printing is limited to 50 μm. Rotatory screen printing is used for quick throughput but has a lower resolution. On the contrary to screen printing, flexo and gravure give better resolution but can only be used for printing relatively low viscosity inks on large-area flexible substrates.

However, using these methods for low-volume production or preliminary development tests can be relatively wasteful of expensive or supply constrained materials. Lately, interesting research has been carried out using digital-write additive technologies, such as inkjet printing and aerosol jet printing. These printing techniques are CAD-driven manufacturing approaches that add ink to a substrate according to the design file. This has significant advantages in rapid prototyping, where the production volume is low to extremely-low (down to a single unit) and turn-around time is critical. Unlike other printing techniques such as screen-printing or gravure printing, the design can be changed and refined instantly without intermediate steps (for example, in contrast to the production of plates in offset printing).

The most commonly used digital-write printing technique is inkjet printing. A wide range of inkjet-printed products are available in the market. In this technique, a piezo-electric element ejects a droplet of ink onto the substrate in the desired design pattern. This is an inherent zero-dimensional printing technique, where designs have to be build up out of dots. The ink formulation in inkjet printing is critical, as the nozzle can be easily clogged. However, due to the limited range of usable ink viscosity with this technology, a bottleneck in the choice of materials could be present. The fabrication of multilayered-functional devices (capacitor, transistor, photodetector, etc.) requires the deposition of several layers of materials stacked one over another, each having different ink viscosity. A combination of aforementioned techniques can be used to fabricate such a device but it adversely counter-effects the process complexity and fabrication cost.

Aerosol Jet Printing (AJP) is a recently introduced digital-write system compatible with materials having an extremely wide range of viscosity (Hedges & Marin, 2012; Renn, 2007). It is a CAD driven vector based printing method that uses a sheath of an inert gas to tightly focus a beam of aerosol onto a substrate. This method offers multiple advantages in flexibility as compared to traditional printing methods: the user-friendly printing from CAD data enables electronics prototyping in small volumes without the setup costs associated with traditional techniques; the inks to be printed can have viscosities ranging from 1 to 1000 cP, which is much more extended as compared to other technologies, and covers the needs of most large scale printing techniques. Moreover, the variable printing standoff distance from the substrate in AJP allows printing on non-planar or curved surfaces. Additionally, an in-situ laser annealing tool is present which allows local sintering of conductors while protecting surrounding organic materials.

Printed Structures and Devices

This section introduces the advances in printed devices for the three applications that will be further explored in this thesis, namely photodetectors, packaging and microwave structures. The focus will be on introducing the main device operating mechanisms, an understanding of their performance metrics, as well as summarizing the state-of-the-art in the respective printed electronics field.

Photodetectors

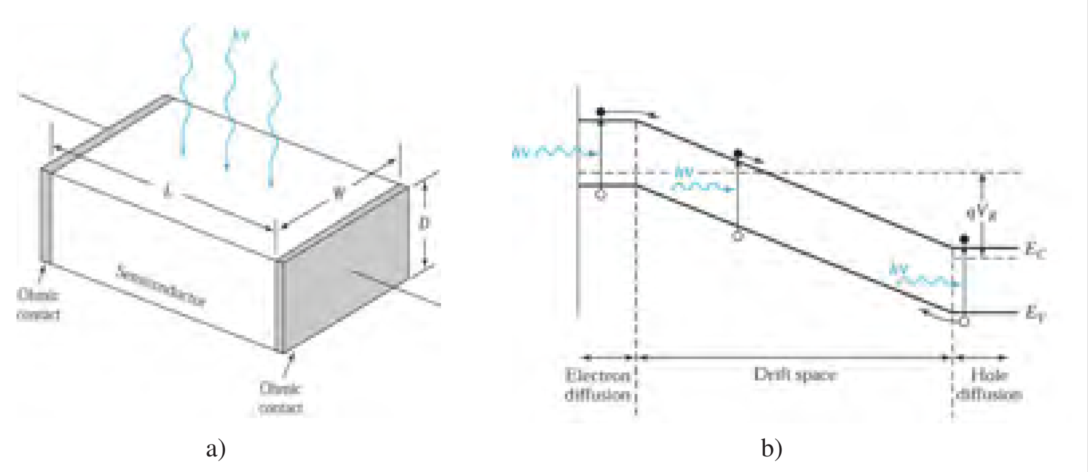

a)

b)

Figure 0.3 (a) Photoconductor principle and (b) photodiode principle
Sze & Ng (2006)

Photodetectors are semiconductor devices that capture and detect photons. The basic mechanism of these devices consists of the generation of an electron-hole pair through a band transition after photon absorption. The mechanism of charge transport and multiplication divides the photodetectors into two main categories.

In the photoconductor category (Fig. 0.3a), the photo-generated charge carriers increase the conductivity of a slab of semiconductor material. The charge carriers drift under the influence of the applied external electric field, which leads to the photocurrent. Photoconductors can exhibit photocurrent-gain, meaning that each photo-generated electron-hole pair can contribute multiple times to the current.

On the other hand, in the photodiode category (Fig. 0.3b), a build-in electric field separates the electron-hole pair, which flow as a current at the terminals. The electric field is generated by either a p-n junction between two semiconductor materials, or a metal-semiconductor junction. The photocurrent gain is less than one, as each photo generated carrier can only contribute once to the photo current.

In general, a photodiode will absorb photons in a particular absorption band below the cut-off wavelength. The device is characterized by IV measurements under a uniform light intensity of the target wavelength (Fig. 0.4a). The primary performance metric of the photodiode is the responsivity (Sze & Ng, 2006):

$$R = \frac{I_{ph}}{P_{opt}} \tag{1}$$

where I_{ph} is the photocurrent and P_{opt} is the optical power. A higher responsivity is desired such that a larger electrical signal is generated for a given light intensity.

On the other hand, a photodetector should have a small dark current, which is defined as the current under zero light intensity. The dark current is due to the thermal generation of charge carriers in the junction, and it limits the smallest light intensity that can be detected.

The speed of the photodiode is of importance in applications where the light intensity is pulsed. A wider depletion region limits speed because of the transit time of the charge carrier, but a narrower depletion region has more junction capacitance, which will result in a larger RC time

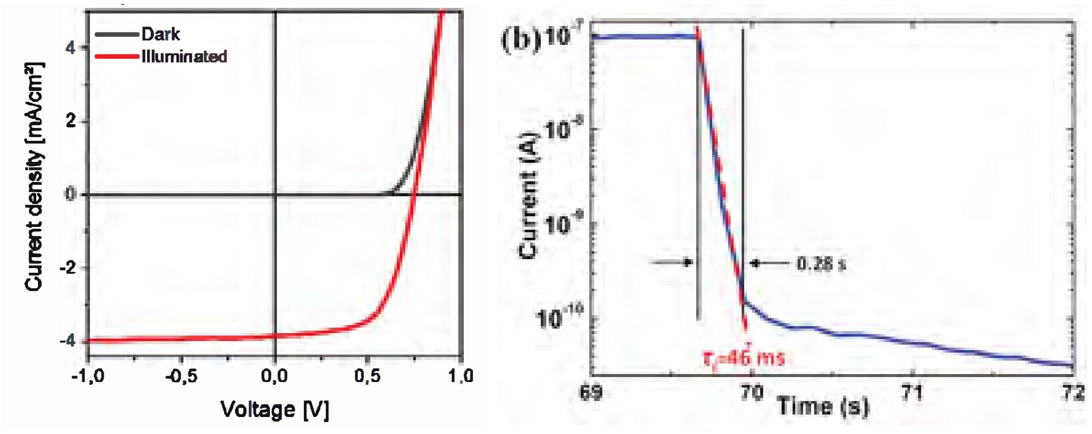

a) b)

Figure 0.4 (a) Photodiode IV curve under dark and illumination (Verilhac, 2012), and (b) time constant of falling edge (Cheng *et al.*, 2011)

constant. Under pulsed light conditions, the photocurrent rises and falls exponentially, and the photodetector speed can be expressed as the associated exponential time constants (Fig. 0.4b).

Some applications for photodetectors include light sensing, imaging, optical communications, smoke and chemical sensors. Printing technology opens up new features and can lead to disposable, expandable, bendable and light weight photodetectors.

The fabrication of a low-cost disposable multilayer polymer photodetector (with area $\approx$ 16 mm^2) using inkjet printing and AJP on a paper substrate was reported by (Aga *et al.*, 2014). Its structure comprises of Ag bottom electrode, Poly(3,4-ethylenedioxythiophene) Polystyrene sulfonate (PEDOT:PSS) buffer layer, Poly(3-hexylthiophene-2,5-diyl) Phenyl-C61-butyric acid methyl ester (P3HT:PCBM) photoactive layer, Deoxyribonucleic acid (DNA) bio-polymer as transparent surface modifying layer and conductive PEDOT:PSS as top electrode, as shown in figure 0.5. The photo response was measured at wavelengths of 405, 465, 525 and 635 nm. Possible applications include ambient light sensing and light enabled Radio-Frequency IDentification (RFID) tags.

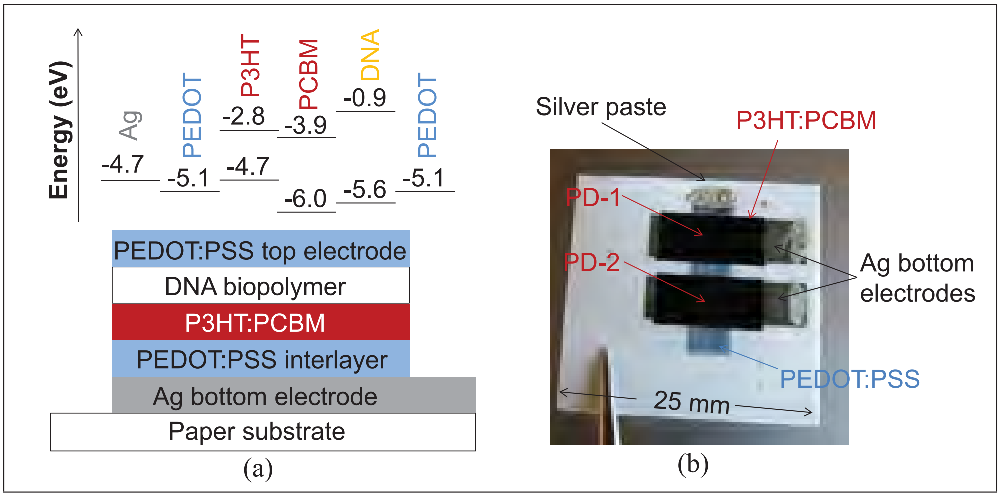

Figure 0.5 Multilayer disposable photodetector on a paper substrate Aga *et al.* (2014)

Zinc-Oxide (ZnO) is a suitable semiconductor for ultraviolet (UV) photodetector applications with its 250-400 nm band absorbance. By incorporating ZnO as a semiconductor nanowire, high performance photodetectors were reported with high photoconductive gain and responsivity (Liu *et al.*, 2014). The speed of this detector is further enhanced by the formation of Schottky barriers, which suppress the dark current of the detector. Figure 0.6a shows the device made with printed electrodes and elektro-spun nanowires.

The use of colloidal ZnO nanoparticles have been reported in a metal-semiconductor-metal UV photodetector with low dark current (Jin *et al.*, 2008). The nano-particle ink was spin-coated on a glass substrate, after which gold electrodes were evaporated (Figure 0.6b). It was concluded that the ZnO film absorbs and desorbs oxygen, which leads to low dark current and high responsivity.

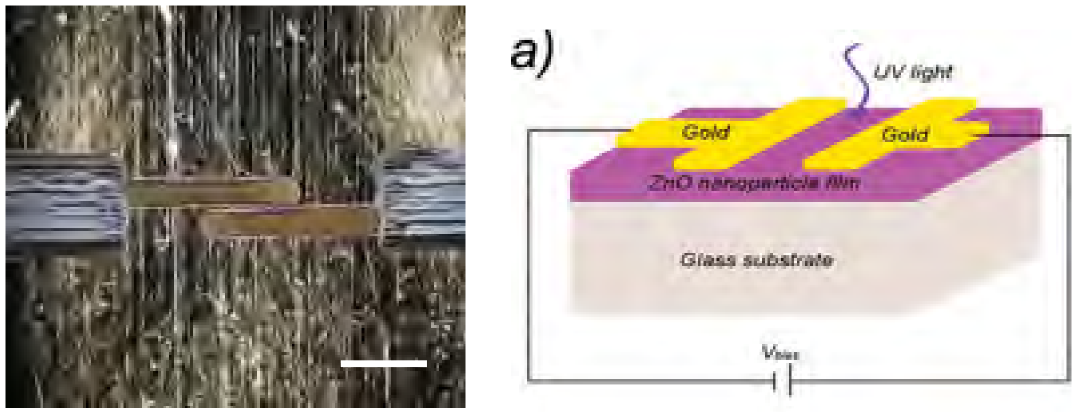

a) b)

Figure 0.6 (a) ZnO UV photodetector with elektrospun nanowires (Liu *et al.*, 2014) and (b) UV photodetector utilizing colloidal ZnO nanoparticles (Jin *et al.*, 2008)

Packaging

In integrated circuit manufacturing, packaging is the assembly step where the semiconductor die is encapsulated to prevent damage, while electrical connections are provided to the circuit board. Mainly two techniques are used in packaging: wirebonding and flip chip.

Fig. 0.7a illustrates the classical process of packaging in a wirebonded plastic leaded package. First, the die is attached to a thermal pad with an adhesive. The pads are then connected to terminal leads with conductive wires, usually gold (Fig. 0.7b). Lastly, the package is sealed with a compound mold.

In flip chip packaging, metallic bumps are deposited on the circuit pads during the wafer stage (see Fig. 0.8a). After cutting of the wafer, each die is positioned such that the bumps line up with the footprint on the package or substrate. Next, heating is applied to melt the solder bumps and form the connection to the footprint. In the final step, an insulative adhesive is pushed under the die to fill the cavity. Fig. 0.8b gives an example of the finished result.

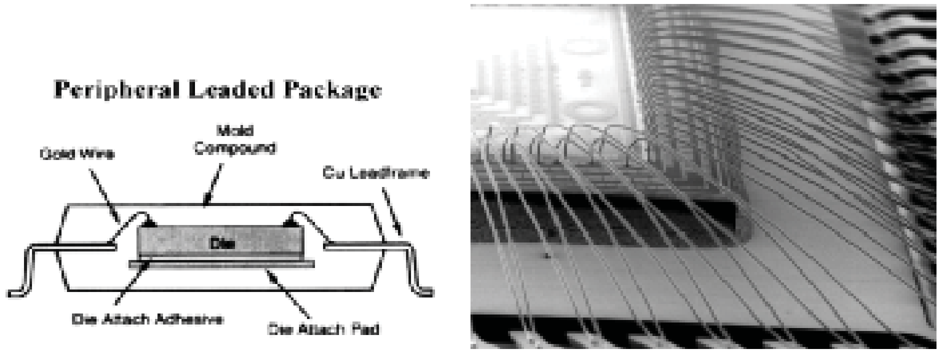

a) b)

Figure 0.7 (a) Classical packaging of a semiconductor die through (b) wirebonding
Greig (2007)

Both wirebonding and flip chip can be performed directly onto Printed Circuit Boards (PCB), which is known as Chip-On-Board (COB), as illustrated in Fig. 0.9. Alternatively, an intermediate plastic or ceramic package is used to route the signals from the wirebonded or bumped pads to exposed leads. The completed package can then be safely handled and soldered onto a PCB.

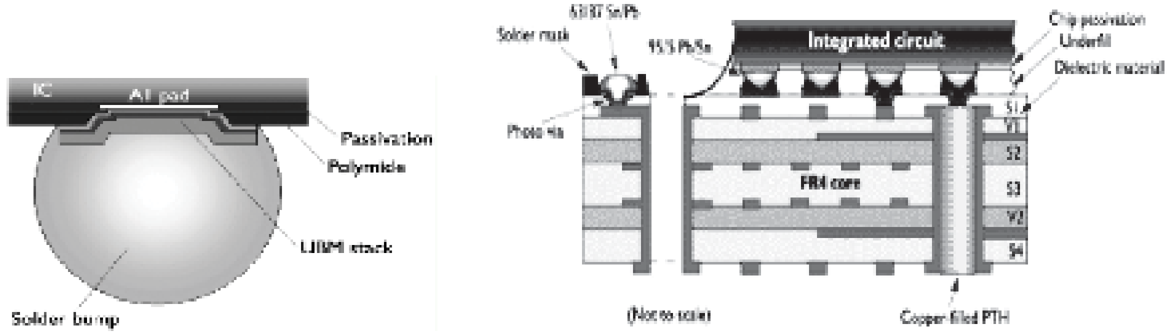

a) b)

Figure 0.8 (a) Flip chip bumping (b) assembly on substrate
Greig (2007)

In terms of electrical performance, the flipchip approach has the lowest inductance and capacitance to ground, but requires a small pitch in the footprint on the substrate or package.

Wirebonding suffers from a considerable lead inductance and capacitance, but its flexibility allows for cheap molded packages. For high-frequency applications, the wirebond length, and therefore its inductance, can be reduced by directly attaching the die on the PCB, and bonding directly to the PCB terminals without intervening package in Chip-On-Board.

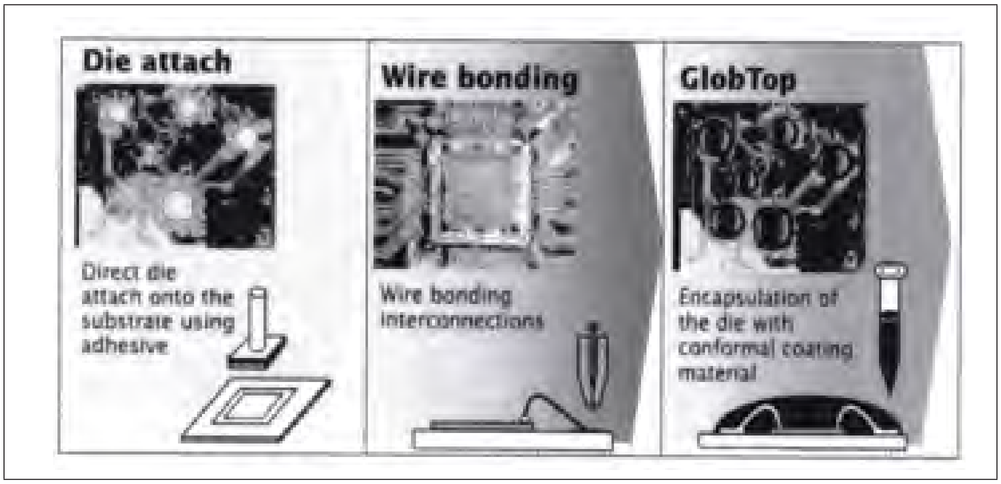

Figure 0.9 Chip-On-Board packaging
Greig (2007)

A recent trend is the stacking of multiple dies in a single package, which is also known as 3D packaging (Fig. 0.10a), in which multiples dies are stacked on top of each other into a single package. The connections can be provided either by wirebonding or Through-Silicon-Vias (TSV). In the first case, the dies are stacked with the help of adhesives and each die is individually wirebonded to the package leads. An offset is necessary to the positioning of each die, as to expose each individual bond pad. In contrast, in TSV stacking, vertical vias that go through the entire die are formed during manufacturing. These are filled during assembly and used to route the signals of upper dies to the substrate (Fig. 0.10b).

The leads in a package can be modeled with the lumped element model in Fig. 0.11a. Each pin has a self-inductance and mutual inductance to neighboring pins, which models the magnetic field. Its electric field is modeled with capacitance to ground and to neighboring pins.

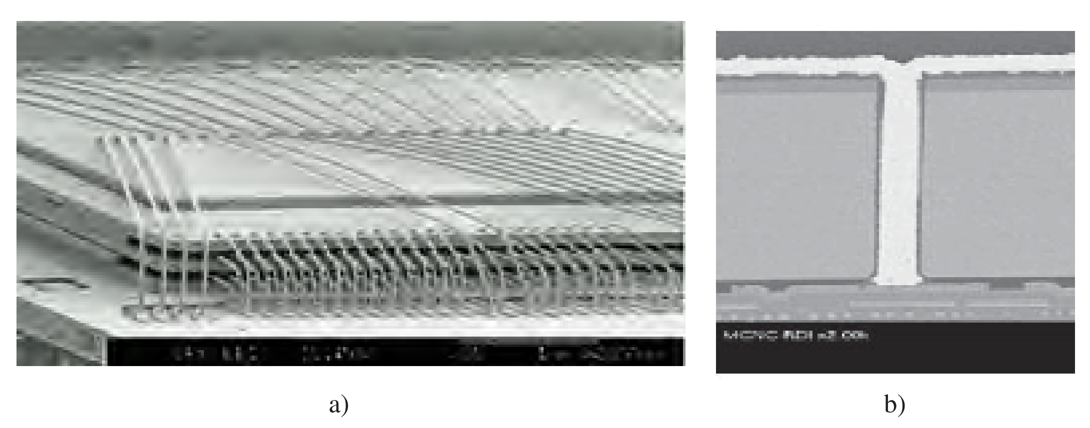

Figure 0.10 Die stacking through (a) wirebonding and (b) TSV
Greig (2007)

Of secondary importance is the resistance of the leads. This network effectively limits the frequency bandwidth of the pin, and requires careful co-design of chip and package in the case of microwave and millimeter wave applications (Liu *et al.*, 2009).

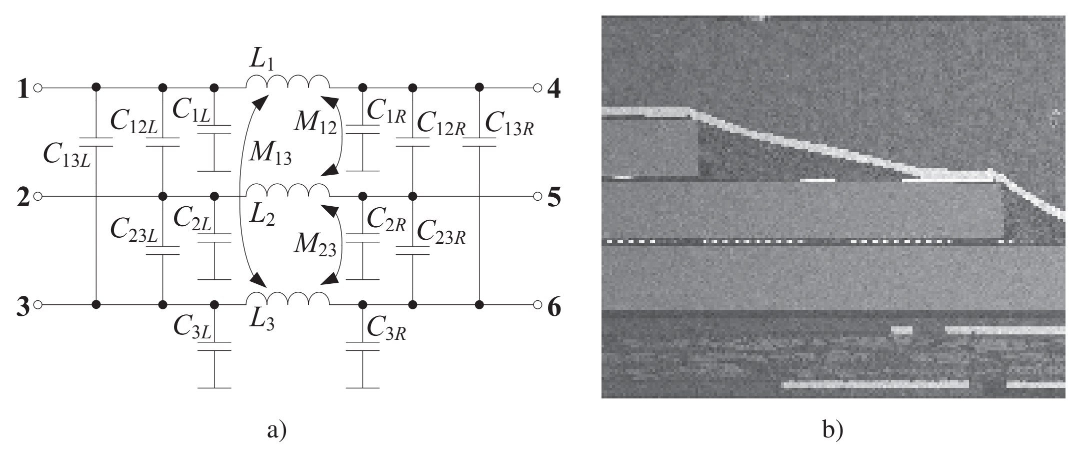

Figure 0.11 (a) Package modeling (Mandić, 2013) and (b) Aerosol jet printed 3D interconnects between stacked dies (J. Renn *et al.*, 2010)

Aerosol jet printing has been proposed as a method to replace wire bonding in certain applications. Since the aerosol stream remains focused up to several mm depth, 3D interconnects can be printed without adjustments to the Z axis (J. Renn *et al.*, 2010) . This feature has been used to print interconnects in a staggered multi-chip die, with 30 μm line width and 10 μm line height (Fig. 0.11b). After printing, thermal sintering was performed, after which the line resistance was measured to be below 1 Ω.

In another example of stacked-die 3D interconnects, aerosol jet printed lines were used to connect two dies in a stacked configuration, as well as the die-to-PCB interconnects (Fig. 0.12). An inclination of 17 degrees was applied to the substrate, resulting in a reduced distance variation of the printing head. Height differences between the dies were smoothed with a mold material, and the 50 μm sized pads were connected with 25 μm wide lines. Many defects were reported in the connected devices, as the variable height of the printing head resulted in increased line widths and shorts between die pins.

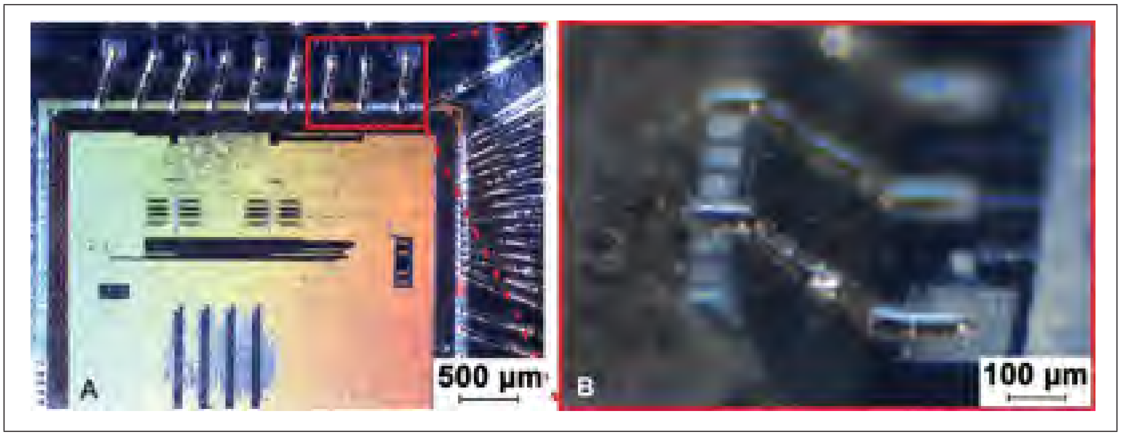

Figure 0.12 Aerosol jet printed 3D interconnects between stacked dies
Seifert *et al.* (2015)

Microwave Transmission Lines and Resonators

The microwave frequency band is loosely defined as being from 300 MHz to 300 GHz, which corresponds to a wavelength from 1 m down to 1 mm. Traditional circuit theory in electrical networks cannot be used, as the short wavelengths in this frequency band forces one to consider how the phase of a voltage or current changes with distance. Electrical signals must therefore be considered as waves, and the appropriate microwave theory has to be used (Pozar, 2004).

An important function in microwave circuits is the transport of a signal from A to B without loosing too much of the signal power. This function is provided by transmission lines, which exist in a number of shapes and forms (Fig. 0.13).

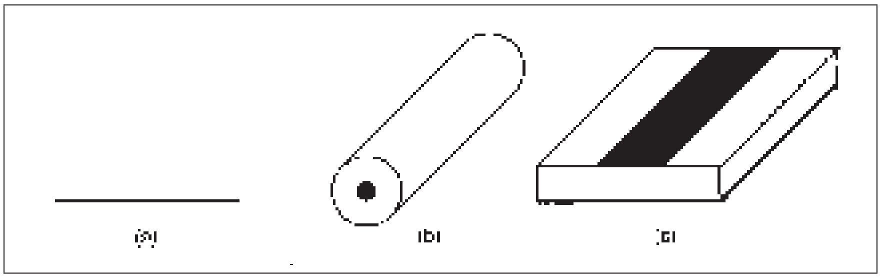

Figure 0.13 Microwave transmission line examples: (a) two wire model, (b) coaxial cable, and (c) microstrip line Gonzalez (1997)

A transmission line has two conductors, separated by an insulator, which can be schematically represented by Fig. 0.13(a). The outer conductor can be wrapped around the inner conductor in a coax cable, with a dielectric as insulator (Fig. 0.13(b)). One conductor can be a ground plane, with a narrow trace as the other conductor, with a dielectric in between to form a microstrip line (Fig. 0.13(c)).

Each transmission line with total length z can be considered as a series of smaller pieces with length Δz, where each piece can be modeled by a lumped element model (Fig. 0.14). The lumped model includes a resistance R for the resistive losses of the conductors, a conductance G for the insulator losses, an inductance L for the magnetic field, and a capacitance C modeling the electric field between the conductors.

Solving for an infinite series of lumped models with $\Delta z \rightarrow 0$, leads to the following conclusions (Pozar, 2004). First of all, the voltage $v(z,t)$ and current $i(z,t)$ vary as a function of time and

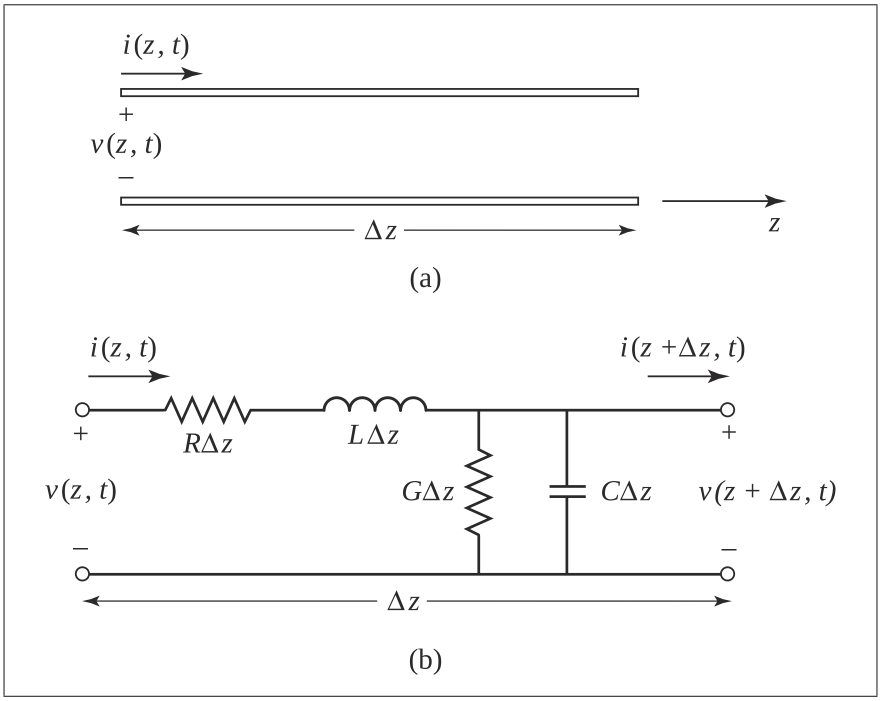

Figure 0.14 Lumped element model of a piece of transmission line
Pozar (2004)

position on the line. Second, a sinusoidal excitation on one end of the line leads to a sinusoidal voltage / current wave on the line, which decays over distance when losses are included.

In the phasor domain, the voltage and current phasor as a function of position z on the line can be expressed as a traveling wave solution:

$$V(z) = V_0^+ e^{-\gamma z} + V_0^- e^{\gamma z} \tag{2}$$

$$I(z) = I_0^+ e^{-\gamma z} + I_0^- e^{\gamma z} \tag{3}$$

where γ is the complex propagation constant, and the first term ($e^{-\gamma z}$) represents a wave traveling in the $+z$ direction, while the second term ($e^{\gamma z}$) represents wave traveling in the $-z$

direction. The complex propagation constant consists of a real and imaginary part:

$$\gamma = \alpha + j\beta \tag{4}$$

where α is the attenuation constant which dictates the dampening of the wave over distance,while β is the phase constant which is 2π divided by the wavelength. The characteristic impedance Z_0 is the ratio between voltage and current in each wave:

$$Z_0 = \frac{V_0^+}{I_0^+} = \frac{V_0^-}{I_0^-} \tag{5}$$

Microwave network analysis is performed with the concepts of incident and reflected waves, characteristic impedance and scattering parameters (S-parameters), which are illustrated in Fig. 0.15. A sinusoidal point generator with voltage V_g and impedance Z_g launches an incident wave into the transmission line. If the characteristic impedance Z_0 of the line is different to the generator impedance, part of the incident wave is reflected back. This is the concept of impedance mismatch between line and source. Next the wave travels over the line, and reduces in magnitude due to the loss of the line. The incident wave on the line is of the form $V_0^+ e^{-j\gamma z}$. At the resistor load with impedance Z_L, part of the wave can be reflected again due to mismatch between the line and load impedance, after which the remaining power is absorbed in the load. The reflected wave on the line is of the form $V_0^- e^{j\gamma z}$. The characteristic impedance Z_0 can be used to find the corresponding incident and reflected current waves.

In S-parameter modeling of the transmission line as a two-port, the S-parameter matrix relates the incident and reflected voltage waves on each port:

$$\begin{bmatrix} V_1^- \\ V_2^- \end{bmatrix} = \begin{bmatrix} S_{11} & S_{12} \\ S_{21} & S_{22} \end{bmatrix} \begin{bmatrix} V_1^+ \\ V_2^+ \end{bmatrix} \tag{6}$$

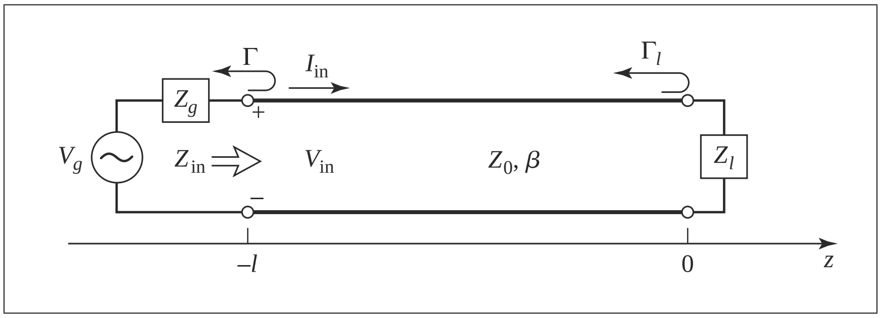

Figure 0.15 S-parameter modeling of a transmission line
Pozar (2004)

The S-parameters of a microwave circuit are measured using a Vector Network Analyzer (VNA). For a transmission line, the input mismatch, as expressed in S_{11} and S_{22}, should be low, while the insertion loss, as expressed as S_{21} and S_{12} should be close to unity.

A derivative structure of the transmission line is the ring resonator (Fig 0.16a), which is a transmission line looped in a ring on itself. The ring supports constructive interference of particular frequencies, with a wavelength that fits an integral multiple in the ring circumference. Energy is coupled into the ring from feed lines through a coupling gap. The structure therefore acts as a filter.

An example of the measured insertion loss of a ring resonator is shown in Fig. 0.16b. Multiple resonances exist, due to the multiples of wavelengths that fit inside of the ring. The performance of the ring is characterized by the insertion loss at the resonance frequency, as well as the Q-factor. The Q-factor is a measure for the fractional bandwidth of the ring:

$$Q = \frac{f_c}{BW_{-3dB}} \tag{7}$$

where f_c is the resonance frequency and BW_{-3dB} is the half-power full bandwidth of the peak.

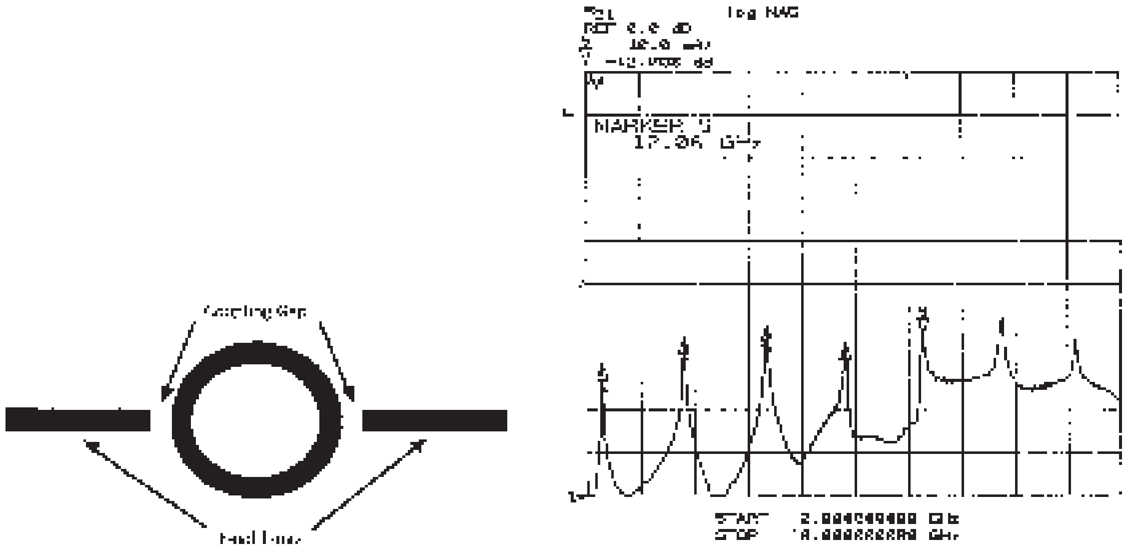

a) b)

Figure 0.16 (a) Top view of a microstrip ring resonator, with (b) measured S_{21} response Chang & Hsieh (2004)

Applications of printed microwave structures can be found in antennas, RFID tags and high speed interconnects. The printing of a low loss transmission line is important for these applications, as it forms the basis of any microwave system.

Belhaj et al. reported inkjet printed coplanar waveguides using silver ink on kapton as flexible substrate, as shown in Figure 0.17. This Coplanar waveguide (CPW) has a length of 1 *mm* and is sintered at 300 °C. A loss of 0.35 dB/mm was measured at 67 GHz, which is close to the achievable loss with traditionally fabricated copper PCBs.

In a follow-up work, Kai et al demonstrated a multi-layer printed transmission line with vertical transitions from CPW to stripline to microstrip (Fig. 0.18). The dielectric is formed by a printed polyimide, while silver is printed as the conductor. The loss was measured to be 0.33 dB/mm at 30 GHz and 0.53 dB/mm at 40 GHz. The envisioned application is in 3D millimeter wave structures for multi-chip modules.

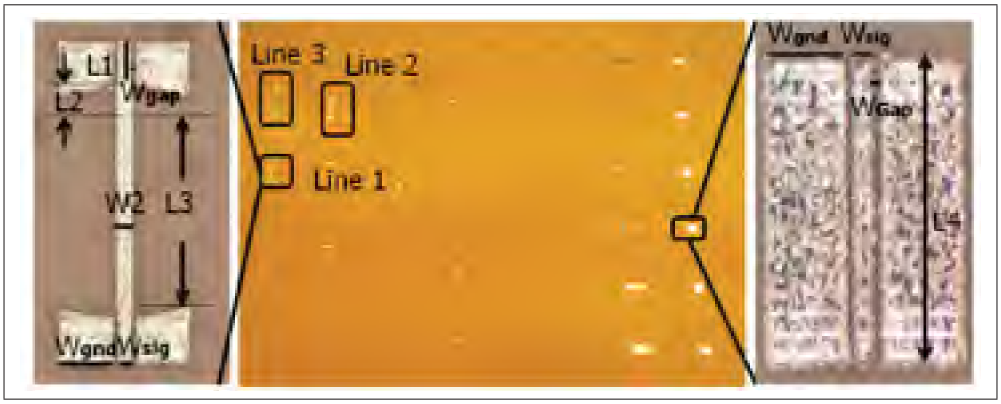

Figure 0.17 Aerosol Jet Printed CB-CPW-MS transmission line
Cai *et al.* (2014)

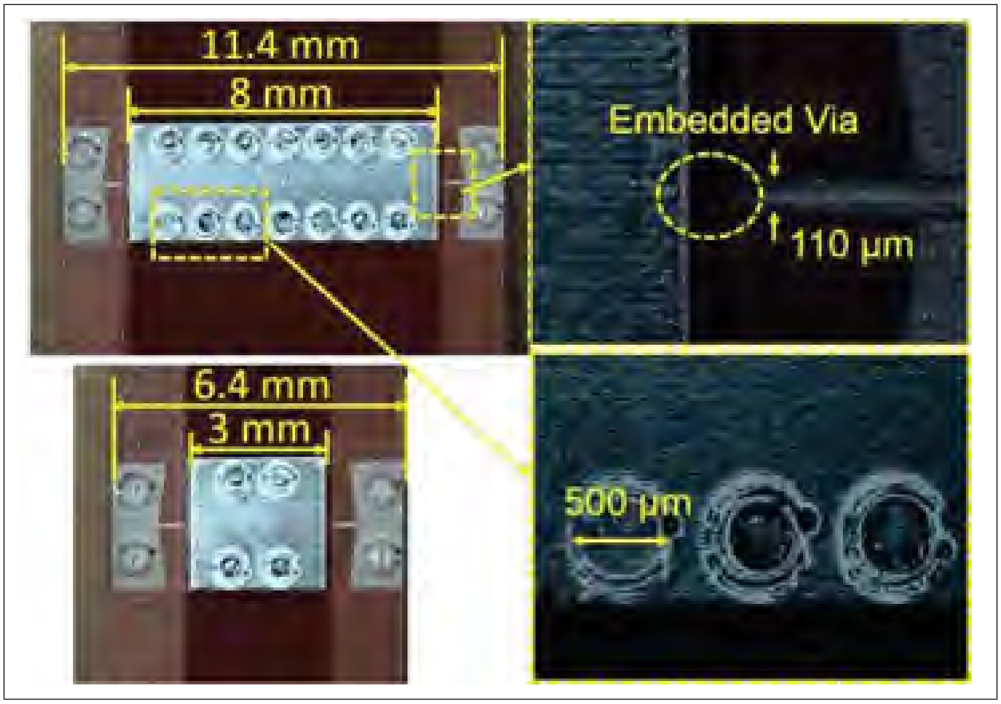

Figure 0.18 Multi-layer printed transmission line with transitions from CPW to stripline to microstrip
Cai *et al.* (2016)

Inkjet printed CPW with kapton as substrate material and silver as conductor were presented (Fig. 0.19). A loss of 0.3 dB/mm was demonstrated at 67 GHz after sintering at 300 °C. It was shown that the Radio Frequency (RF) performance of the transmission line was not significantly affected by bending, leading to possible applications in flexible microwave electronics.

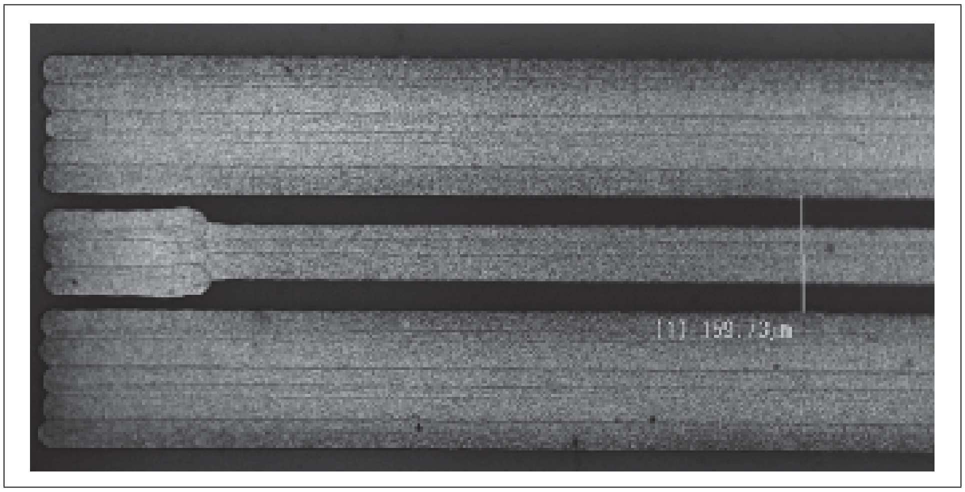

Figure 0.19 Inkjet printed CPW on kapton substrate
Belhaj *et al.* (2014)

Research Goal

Digital-write printing techniques embody the ideal of electronic manufacturing by printing: fast turnaround time, flexible designs, low cost and low wastage. Inkjet printing has been at the forefront of research into digital-write techniques, despite its constraints on ink formulation and sensitivity to nozzle clogging. In contrast, AJP has emerged as an alternative technique with tempting advantages, such as a wide range of possible ink viscosities, a high resilience to nozzle clogging, an inherent vector-like deposition pattern, and limited conformal 3D printing capability.

Since its inception, it has been postulated that AJP opens up exciting new printed devices due to its unique printing characteristics. Several interesting concepts have been demonstrated in literature, but it is clear that AJP needs a driving research effort in order to fulfill its promise. It is therefore the goal of this thesis to explore the potential of AJP, in particular in the field of photonics, chip packaging and microwave structures. Chapter 1 first discusses the characteristics and challenges of the AJP system, so that a better understanding of its potential and limitations can be reached.

Printed electronics has increasingly penetrated the photonics market, with devices such as solar cells, light emitting diodes and photodetectors being manufactured by printing techniques. The attractive properties of printed electronics in this case are large area manufacturing, flexible substrates and low cost production. Of special interest is the development of a low-temperature manufacturing process, such that large, inexpensive panels of thin, lightweight, recyclable and flexible substrates can be produced. Keeping device performance in mind, there has been substantial research effort into nanostructured materials for photonics, in particular utilizing zinc oxide for ultraviolet sensing. In this context, chapter 2 discusses in detail the work on a low-cost, zinc oxide photodetector, which benefits from the specific processing by AJP to maximize its surface area on the nano scale.

In conventional electronics, the fabricated semiconductor dies are assembled into packages in order to protect them and provide leads at a convenient size and pitch for PCB assembly. Wire bonding is the cost effective approach but suffers from limitations in bandwidth, while flipchip packaging requires expensive interposers and careful thermal coefficient matching. A low cost and high performance packaging technique is called for to enable applications in the microwave and mmWave frequency bands, while providing convenient plastic molded packaging. To this end, chapter 3 discusses the work on utilizing AJP to print transmission lines inside of a plastic molded package with the aim of providing a high-speed interface to the semiconductor die.

Of the various microwave structures, ring resonators have found myriad applications as sensing components. The size of the ring resonator is linked to the resonating frequency, with large rings being fabricated on printed circuit boards and interfaced to integrated circuits designed for sensing applications. Interesting applications are envisioned with smaller rings at corresponding microwave resonating frequencies, but the interface from the PCB implemented ring to the amplifier semiconductor die has proven challenging due to the high operating frequencies. In order to break this trade off, chapter 4 reports the work on a fully-printed microwave ring resonator, which can be directly integrated with a sensing integrated circuit.

CHAPTER 1

AEROSOL JET PRINTING

1.1 Background

Aerosol jet printing, developed by the Optomec Corporation, is also known as a Maskless Mesoscale Material Deposition (M^3D^{TM}) apparatus, and is a non-contact, CAD-driven direct write method capable of printing electronic materials on planar as well as non-planar surfaces. It can be used in an ambient or an inert environment for the deposition of micron sized features (Renn, 1998). This process aerosolizes the functional material and deposits it onto the substrate using aerodynamic focusing. The applications of the aerosol-jet process are not limited to the printing of electrical devices and circuits, but are also extended to the direct-writing of biological materials.

1.2 Operating Principle

Aerosolization of an ink can be accomplished in two different ways. A schematic of the AJP method illustrating its working principle in terms of the Pneumatic Atomizer (PA) and Ultrasonic Atomizer (UA) are shown in Fig 1.1. In the PA, a stream of inert gas, such as N_2 is blown over the ink surface. This generates a mist of material having droplets of different sizes. Droplets bigger then 5 μm drop back into the ink reservoir due to the force of gravity and are recycled. The finer droplets with dimension < 5 μm are propelled by the N_2 stream towards the deposition head. Before reaching the printing head, a device called virtual impactor removes the extra gas and increases the density of the aerosol stream to enhance the deposition. In the case of the UA, an ultrasonic transducer is used to generate the mist. Once the container is saturated with mist, an inert gas carries it directly to the deposition head without passing through the virtual impactor. At the deposition head, a second flow of N_2, called the sheath gas, surrounds and compresses the aerosol stream as it passes through the nozzle. This results in aerodynamic focusing of the stream, thereby reducing spray-over. The particle stream is then deposited onto the substrate, and is capable of forming fine features ($<10\ \mu$m). A mechanical shutter and a precision motion control system allow the printing of complex patterns on the substrate (Hedges & Marin, 2012).

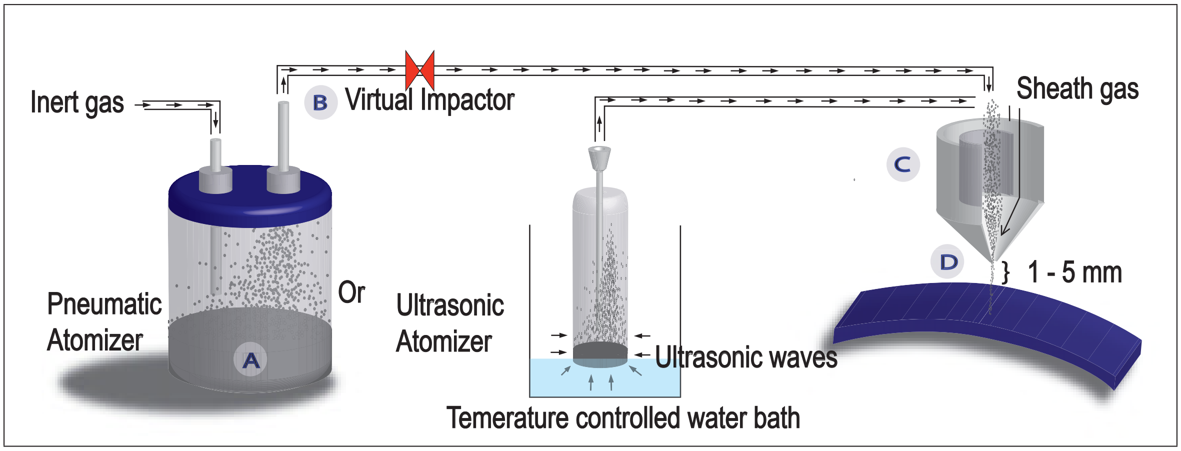

Figure 1.1 Schematic diagram illustrating Aerosol Jet Printing setup and operating mechanism

During the deposition process, there exists no contact between the material and the nozzle. This prevents material build up at the tip, which keeps this critical area of the printing system clean, permitting longer usage times and stable operation. Also, there exists a stand off gap of about 1-5 mm between the nozzle and the substrate. This helps in accomplishing conformal printing on 2D-3D structures. The small dimensions of the aerosol droplets are responsible for creating fine patterns, good edge definition, and a high control over the deposited thickness and profile.

Deposited materials then undergo post processing (drying, sintering or curing) in order to improve their properties, such as electrical conductivity, mechanical stability and adhesion. This could be done by either using a heated platform or via laser. Polymer materials such as epoxy and acrylic dielectric inks can be post processed using UV curing.

1.3 System Components

The main components of the Aerosol Jet Printer includes: atomizers, virtual impactor (VI), tube heater, deposition head, visual aid system (printing process camera, alignment camera), laser, platform and temperature control/stirring unit (Figure 1.2). The two different types of atomizers include: pneumatic atomizer (PA) and ultrasonic atomizer (UA). Both use a different mechanism of generating mist. Mist collection and transfer to the deposition head occurs in a similar way in both cases.

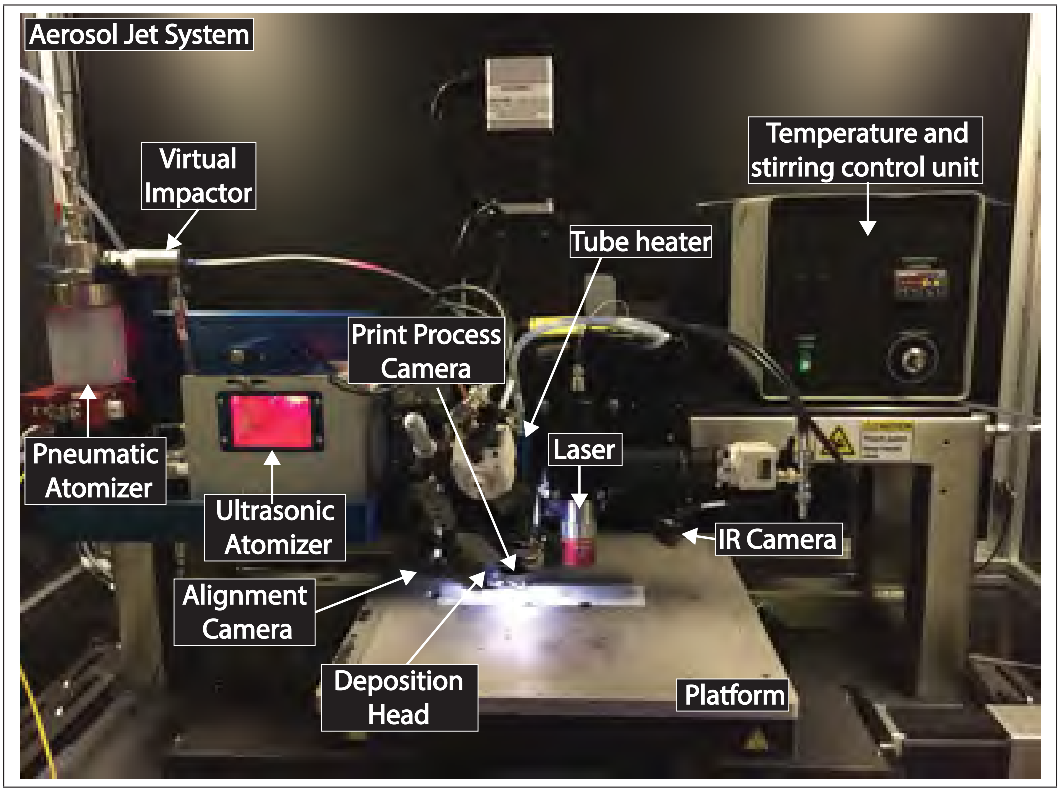

Figure 1.2 Aerosol jet system with annotated components

Atomizers

Ultrasonic atomizer: Ink formulations based on high vapor pressure and low weight % loadings having viscosity between 1-5 cP can be printed using the UA. In this case, the mist is generated by exposing the source material to an ultrasonic transducer. The high-frequency pressure waves generate fine droplets from the liquid ink. These droplets are then carried by an inert gas stream towards the printing head. The particle size in suspensions is limited to <50 nm for optimum printing.

Pneumatic atomizer: Thick functional inks and pastes based on solvents having low or medium vapor pressure ($<$ 1mmHg) or having high weight % loadings having viscosity up to 1000 cP are printed using the PA. A high-velocity gas stream is used to break the liquid into droplets. Larger droplets hit the reservoir wall and fall back while the smaller droplets ($< 5\mu$m) remain suspended in the mist. An inert carrier gas stream carries these droplets towards the deposition head. For particulate-suspension inks, the particle size used with PA must be less than 500 nm.

Virtual impactor The virtual impactor is a device present between the ink reservoir and the printing head. It extracts out excess carrier gas and concentrates the aerosol stream before it passes through the tube heater and reaches the deposition head.

Tube Heater The tube heater surrounds the carrier tube carrying the functional material, which is about to be printed. Prior to being deposited, the aerosol stream can be heated in order to remove the volatile solvents if required. It allows quick drying of material onto the substrate. It prevents ink overflow and also enables the printing of high aspect ratio structures.

Deposition Head Inside the deposition head, a second inert gas stream know as sheath gas is introduced. It surrounds the carrier gas the brings the functional material from the ink reservoir as it passes through the nozzle. The sheath gas has two key roles: (1) Aerodynamic focusing of the printing stream ; (2) Avoids nozzle clogging by preventing the contact of material with the sidewalls of the deposition head. Different sizes of nozzles can be used, such as, 100, 150, 250, 300 μm depending on the resolution required for the printed line width. For the same atomization gas flow rates, a smaller nozzle will print narrower but thicker traces, where as a broad nozzle will print wider but thinner traces.

Visual Aid System The AJ visual aid system comprises of three built-in cameras: (1) The alignment camera allows exact positioning of the substrate prior to printing. It is used to perform manual alignment of the toolpath to the exact co-ordinate on the substrate where the feature must be printed. Also, it is used for offset adjustment between successive printing runs. (2) A print-processing camera helps in the real-time monitoring of the process run. In case of any problem, the process could be immediately stopped, such as misalignment, toolpath malfunction, overflow or no output of material, etc. (3) Infrared camera for the alignment of laser with the printed feature which is to be sintered.

Laser The AJ system has a built-in 830 nm infrared multi-mode laser for in-situ post-processing of the printed materials. The laser spot has a diameter of 30 μm and an adjustable output power of 100-700 mW. The program file used by laser can easily be generated using the design file used to print the same feature. The process parameters, such as pitch, speed and power can also be easily controlled.

Design and Toolpath generation The toolpath for printing structures can be generated either by using AutoCAD software or by programming manually. A design file in Drawing Exchange Format (DXF) format created using software other than AutoCAD can also be used. First, a geometric shape is created as shown in Figure 1.3 (a). The shape can then be filled using different methods, such as serpentine or perimeter fill method. Almost all our designs have been created using a serpentine fill method at 0° angle without any outline. A sample of the serpentine fill method is shown in Figure 1.3 (b). The pattern is then converted to toolpath in PRG format to be input into the aerosol jet system to deposit materials. The completed design after printing is shown in Figure 1.3 (c).

1.4 Process Optimization

Aerosol Jet printing requires optimization of a number of process conditions in order to achieve the best results. The complete print process comprises of four main steps: (1) ink selection, (2) surface treatment, (3) process parameters optimization and (4) post-processing. The first step is to choose the right ink and substrate. For the selection of suitable solvents and co-solvents, it is important to consider a number of properties including polarity, vapor pressure, viscos-

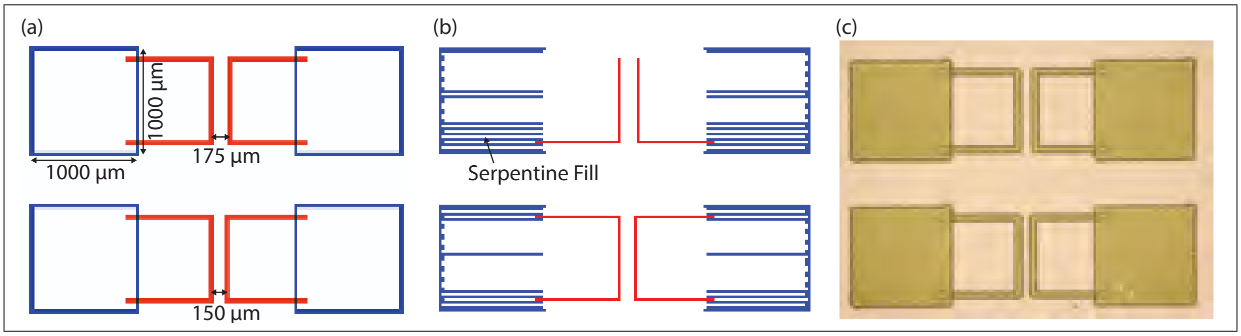

Figure 1.3 Steps in the toolpath generation: (a) input of geometric shapes ; (b) conversion to filled shapes ; (c) resulting printed structure

ity, surface-tension and boiling point. The second step is to prepare the substrate to achieve the best print quality by physical or chemical surface treatment methods (cleaning, corona or chemicals). The third step is a systematic investigation for optimum process parameters, such as temperature, flow rates, focusing ratio, speed and power. The last step is to optimize the post processing treatment (thermal, laser or UV) to obtain better properties, such as electrical conductivity, mechanical stability and adhesion.

1.4.1 Ink Considerations

An ink is a liquid or a semi-liquid collidal system which typically comprises of an active material, a vehicle, additives, and solvent. Inks can be broadly classified into two main categories: aqueous based inks (for example water) or solvent based inks (for example xylene, toulene, chlorobenzene). Not every ink is suitably printed on all substrates due to surface energy mismatch. In order to overcome this problem, either ink formulation or the substrate surface can be modified.

Viscosity

Viscosity simply refers to the resistance offered by an ink to flowing. An ink which is less viscous or "thin", flows freely, for example water and alcohol. On the other hand, a viscous or "thick" ink, such as honey or mercury, does not flow easily. The viscosity of an ink can change when subjected to shear, temperature, and more.

AJP is capable of printing materials (pure liquids, solutions, dispersions or suspensions), fluids, as well as pastes in a viscosity range of 1-1000 cP. Viscosity plays an important role in determining the atomization rate and controlling the thickness of printed films, and it dictates the printing quality. Viscous inks are capable of printing high aspect ratio structures in a single pass. They tend to resist overspray and form structures with better edge definition. On the other hand, if the ink is too thick, it might be difficult to atomize or spread onto the substrate.

The viscosity of an ink formulation can be adjusted by: (1) the choice of solvent and co-solvent system; (2) solid loading content, i.e., weight % content of solute added in solvent; and (3) dilution, i.e., addition of more primary solvent. This lowers the viscosity and solid loading. The use of viscosity modifiers (eg., long chain polymers) should be limited since they make atomization difficult. Since the viscosity of ink is strongly affected by the temperature, it is suggested to use the inks at constant temperature for reproducible results.

For example, the SU-8 2002 ink in chapter 3 and 4 was diluted to make it suitable for printing with the ultrasonic atomizer. The off-the-shelf ink has 29% solid loading with a 7.5 cP viscosity, which was diluted by half using cyclopentanone, resulting in 14.5% solid loading and a viscosity of 2.5 cP.

Vapor Pressure

The vapor pressure of an ink depends on the solvent used in the ink formulation. If a solvent has weak intermolecular forces, a small amount of heat energy will allow the molecules to escape. Thus, it will tend to have a faster evaporation rate, resulting in a lower boiling point.

A liquid having extremely high vapor pressure is termed as a volatile liquid. The inks based on volatile solvents dry out extremely fast and do not have enough time for surface tension to interact with the surface to form smooth films. In some cases, the solvent will evaporate even before passing through the printing head. This will result in a building up of material and clogging of printing components. Inks based on low vapor pressure solvents help to achieve a steady print rate over a long time scale. This also allows a high weight % solid loading with the PA, which is required to print high aspect ratio structures. But if the vapor pressure is too low, the atomization of ink becomes difficult.

For example, while using the UA, if the vapor pressure of the solvent is too low, such as ethylene glycol (mmHg=0.084), it is not possible to get aerosolisation at the maximum allowable power of the ultrasonic transducer. If the vapor pressure of the solvent is extremely high, such as acetone (mmHg=184.5), the printing run is extremely short, which results in non-uniform printing. Heating the ink can increase the vapor pressure. However, it is critical to maintain the temperature of inks constant during the entire printing process. This allows the vapor pressure to remain stable in order to achieve reliable printing over a period of time. The ink properties can also be modified by the addition of a co-solvent ($\sim$ 10 vol.%) to the primary solvent ($\sim$ 90 vol.%).

Particle size and encapsulant

In AJP, it is easier to achieve atomization of smaller particles and encapsulants. Smaller particles have a higher surface area to volume ratio, which is responsible for several advantages.

In the case of semiconductor inks, nano-particles are known to give higher performance for sensing applications due to enhanced surface area. In the case of conductor inks, nano-particles in comparison to nano-flakes fuse at a much lower temperature. Lower sintering temperatures allow the usage of low temperature substrates, such as paper and polyethylene terephthalate (PET). However, if the sintering temperature is not the limiting factor, nano-flake ink can give a lower resistivity due to reduced contact resistances.

Commonly, in an inorganic conductor ink, metallic nanoparticles are stabilized using organic encapsulants. During sintering, first the solvent is evaporated, followed by the disassociation of the encapsulant. Thereafter, the metal particles fuse together to form a metal thin film. The melting and merging of metal particles allow regaining the conductivity similar to bulk material. As such, the minimum sintering temperature is limited by the boiling point of the encapsulants (Molesa, 2006), and it is beneficial to select encapsulants with a lower boiling point.

In chapter 2, the ability of AJP to print large particles is utilized to print nano-crystals with a size between 100 nm and 1 μm. The resulting porous structures is key in achieving the high performance of the ultraviolet photodetector. AJP can also handle metal inks with large particle sizes. For all designs in chapter 2, 3 and 4, a Novacentrix HPS-030AE1 silver flake ink was used for the conductors, with a particle size distribution between 10 nm and 800 nm.

Surface Tension

The surface tension of a liquid affects its ability to wet a substrate. Adhesive forces help in the spreading of ink, whereas cohesive forces cause the ink to form a droplet and prevents the contact with the surface. Adding surfactants or a co-solvent can modify the surface tension of the ink. Surfactants that are routinely used in inkjet printing for suitable ink preparation are not guaranteed to be compatible with the ultrasonic atomizer of the aerosol jet printing system. As it uses a transducer to generate mists, the use of surfactants may result in the formation of froth, which leads to a degradation of the print quality. Therefore, whenever the ultrasonic atomizer is used for printing in chapter 2, 4 and 5, surfactants are avoided. However, in future the use of surfactants along with defoamers can be explored.

1.4.2 Surface Treatment

Surface treatment is important to improve the wetting characteristics of aerosol jetted droplets for the formation of continuous lines and thin films. It is crucial for spreading and adherence between the liquid and the substrate. Wettability directly depends on the surface energy of the substrate and the surface tension of the ink. The wetting ability of a surface can be measured by its contact angle. A lower contact angle ($< 90^\circ$) means that wetting of the surface is favorable. A large contact angle ($> 90^\circ$) indicates an unfavorable wetting ability of the surface.

A wide range of substrates are available, each having a different surface energy. When a low surface tension liquid, such as alcohol, is printed on a high surface energy substrate, such as metal or glass, it stretches out to achieve complete wetting. But when printed on a low energy surface, such as polymer or Polytetrafluoroethylene (PTFE), it results in partial wetting. Similarly, when a liquid having high surface tension, such as mercury, is printed on top of a high-energy substrate, it results in partial wetting. But when printed on low energy substrate, it may result in little to no wetting. This has been summzaried in Table 1.1. Complete wetting is useful to deposit thin films. On the other hand, partial wetting helps to deposit structures having high aspect ratios. In short, the higher the surface energy of the substrate in comparison to the surface tension of the ink, the smaller is the contact angle and the better is the wettability. In order to achieve a good interaction between a liquid and a substrate, the surface energy of the substrate should be about 2-10 mN/m more than the surface tension of the liquid (Tantec, 2019).

The low surface energy of a substrate can be inherent (PE, PP, PTFE, etc.) or due to the presence of surface contaminants. Surface contamination may result in poor wetting, poor adhesion and pinhole formation, which can lead to a degradation of device performance. In order to improve the wetting characteristics of a surface, several techniques are currently available, such as corona and plasma pre-treatment technologies. These methods enable uniform wetting by raising the surface energy of the substrate and thereby reducing the contact angle of the printed ink. Also, high energy plasma is used to remove low molecular weight contaminants from the substrate and to expose a clean surface for improved wettability and adhesion.

It is essential to start the printing process with clean substrates, so that the wetting is optimal. The substrates that were used for the photodetectors in chapter 2 were thoroughly cleaned with soap solution/acetone/isopropyl alcohol/deionized water before printing. In chapter 3 and 4, pre-fabricated PCBs with a high surface cleanliness were used. In this case, the high surface energy of the substrate copper surface, combined with the high surface tension of the SU-8 results in partial wetting, which aids in the formation of high aspect ratio structures.

This proved beneficial in constructing 30 μm and 75 μm thick dielectrics for 50 Ω matched transmission lines.

Surface Tension of Ink	Surface Energy of Substrate	Wettability
Low	High	Complete wetting
Low	Low	Partial Wetting
High	High	Partial Wetting
High	Low	Poor Wetting

Table 1.1 Wettability dependance on surface tension of ink and surface energy of substrate

1.4.3 Process Control

In AJ printing, the basic element of deposition is the line[1]. Control of the line parameters is crucial in accurately reproducing the CAD design. The printing in chapter 2, 3 and 4 was performed while applying the principles outlined in this subsection.

Line Width

AJP requires the adjustment of several parameters to ensure an optimal print quality and an optimized line width. For example, the geometry of a printed line is affected by various parameters such as: gas flow rates, nozzle diameter, stage speed and substrate temperature.

The primary gas flows that have a major influence on the line width include sheath gas, virtual impactor and atomizer gas flow, which were previously defined in section 1.2. For the PA, the carrier gas flow rate is equivalent to the difference between the atomizer and the virtual impactor gas flow rate. Whereas for the UA, due to the absence of a virtual impactor, the net carrier gas flow rate is the same as the atomizer gas flow rate. For a specific material at a given carrier gas flow rate (in sccm), the amount of material being propelled from the atomizer to the printing head remains fixed. As a result, a reduction in line width corresponds to an increase in line thickness and vice-versa. Depending on the application, narrow and thick lines for fine pitch, or thin and wide lines for filled shapes can be printed. The line width is

---

[1] In contrast to inkjet printing, where a point is the basic element

mainly determined by the ratio between sheath and carrier gas flow rate, which is defined as the focusing ratio (A. Mahajan & Francis, 2013):

$$\text{Focusing Ratio (FR)} = \frac{\text{sheath gas flow rate}}{\text{carrier gas flow rate}} \tag{1.1}$$

Figure 1.4 showcases the line width with a silver nano-particle ink, and with different nozzle sizes of 150 μm, 250 μm and 300 μm. As we can see in the figure, higher focusing ratios reduce the line width until a limit is reached. This is due to turbulence in the jet stream and the built-in pressure inside the nozzle head (A. Mahajan & Francis, 2013). We can further observe that a smaller diameter nozzle allows the printing of finer features at lower focusing ratios, which is useful for depositing high-resolution lines. A wider nozzle gives more control over the variation of the line width and is used for the printing of larger area thin films.

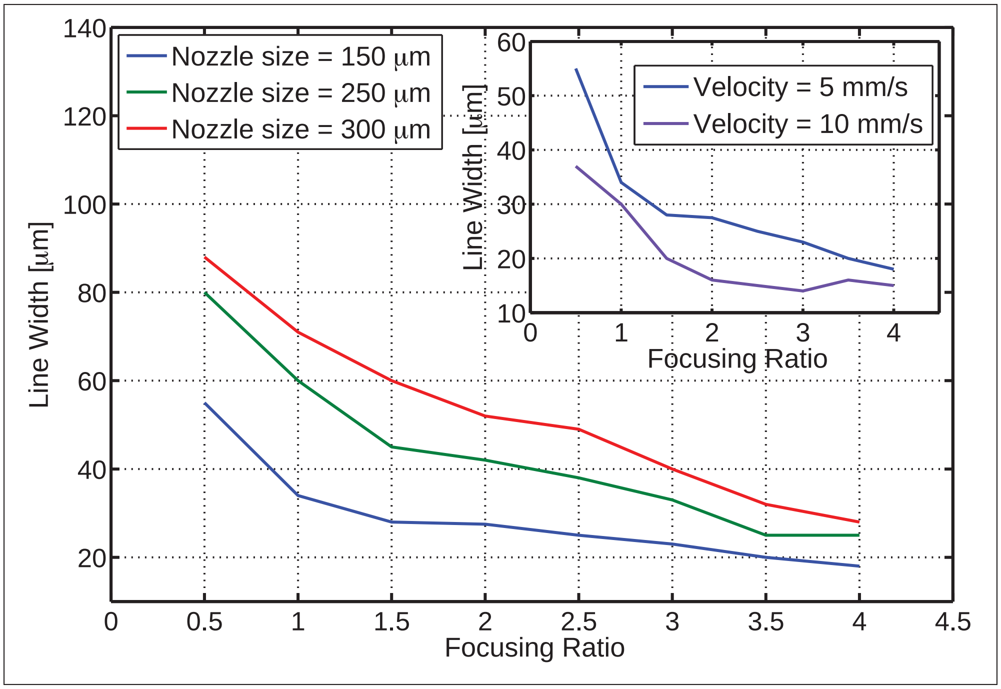

Figure 1.4 Effect on line width with increasing focusing ratio for different nozzle sizes (150μm, 250μm, 300μm), with a stage velocity of 5 mm/s. Inset: effect of stage velocity on line width with increasing focusing ratio

The inset of Fig. 1.4 depicts the achieved line width when the deposits are made at different stage speeds of 5 and 10 mm/s. Both the line width and line thickness decrease at higher velocity. This reduction in cross-sectional area corresponds to the decrease in amount of material being deposited per unit length. The stage speed thus gives additional control over the line geometry. It is however observed that the line becomes irregular and discontinuous at higher velocity, placing a limit on the stage speed.

Line Profile

Another feature critical to obtain smooth surface profile and high-quality uniform film is the cross-sectional profile of printed lines. When the ink is deposited on the substrate, the solvents evaporate and the functional material is left behind. This evaporation process can give rise to a "coffee ring" effect, with an uneven distribution of material along the line cross-section. This is caused by the outward flow of the material, since the evaporation rate is faster at the thin edges (Park *et al.*, 2006). Several approaches for reducing the coffee-ring effect in inkjet printing have been proposed. The first uses two solvents in the ink preparation such that the surface tension gradient offsets the material flow, which is known as the Marangoni effect (Park *et al.*, 2006). In the second approach the substrate temperature is modified such that the evaporation driven material flow is canceled by the geometric surface tension driven flow (Soltman & Subramanian, 2008).

In this work we utilized the second approach and studied the influence of the substrate temperature on the profile of the lines printed by AJP. Figure 1.5 shows the profile of lines deposited using a silver nanoparticle ink at various substrate temperatures ranging from 30 ^{o}C to 75 ^{o}C. It can clearly be observed in the figure that for lower temperature, the shape of the line is convex, while higher temperatures result in concave line profiles. For this specific ink, the optimum temperature of 45 ^{o}C yields a flat line profile.

As this effect depends on the ink properties, the optimization of these process parameters has to be carried out for each material that is used in device fabrication. Moreover, the ink formulation must be stable in order to reproduce printing results over multiple batches.

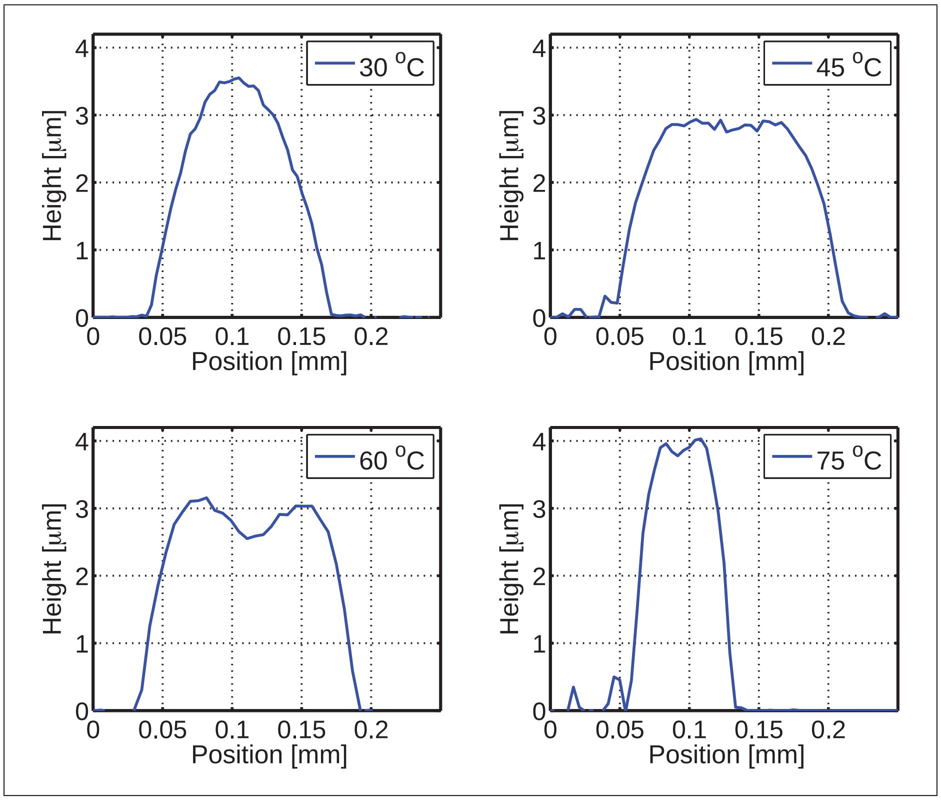

Figure 1.5 Cross-sectional profile of printed lines obtained from surface profilometry with increasing temperature at 30 °C, 45 °C, 60 °C and 75 °C

Line Thickness

In section 1.4.3, it was observed that the line width can be controlled by adjusting a number of parameters, such as the focusing ratio, changing the nozzle size or by adjusting the speed. But, the main challenge lies in controlling the line thickness precisely. In the AJP system, there is no in-situ real time thickness measurement setup. The only way to measure the thickness is to remove the sample from the printing platform and perform the ex-situ thickness measurement. The thickness of dielectric or metals can be critical for many applications, such as transmission lines, antennas and others.

Performing multiple printing passes can help to obtain high aspect ratio structures. Sometimes single layers may not be perfectly filled and might contain voids. Additional passes help to fill these voids. These thick films should be dried before being laser sintered. Otherwise, it may result in residual stress development which may cause the film to peel off (Goth *et al.*, 2011). The effect of multiple passes on the line thickness and line width is shown in Figure 1.6. In chapter 2, 3, and 4, the two materials mainly used to print conductive and dielectric structures are silver and epoxy SU-8 2002, respectively. In Figure 1.6, the left side presents the study of Ag metal ink whereas the right side shows the study of the SU-8 dielectric ink. In both cases, it is observed that the printing of multiple layers result in an increase of thickness without any increase of width. The right platform temperature helps the ink to dry out and prevents overflow of material to the sides.

1.4.4 Post-Process

Post-processing is usually carried out for the removal of extra solvent and densification of the deposited material. This is an important step to achieve maximum electrical conductivity (for metals) and improved adhesion. In conductive inks, the grain boundaries fuse together to form a denser layer, which results in a lower resistance. Increasing the annealing temperature or duration gives a better conductivity.

Thermal annealing and Laser Sintering

The aerosol jet system is equipped with a built-in hot plate (up to 120 °C) as well as an in-situ infrared laser (λ=832 nm). Both the methods are equally effective and have their own advantages. For Novacentrix HP0A1 silver ink, the conductivity obtained by thermal annealing on a hot plate at 250 °C for 1 hour is equivalent to that obtained by laser sintering at 100 mW. The conductivity (σ) in both cases is measured at $\sim 1.69 \cdot 10^7$ S/m (as compared to $6.30 \cdot 10^7$ S/m for bulk silver) by four-point probe measurement.

Using the laser, it is possible to selectively sinter high-resolution features without causing thermal damage to the nearby zone or to the substrate. The laser spot has a diameter of about 30 μm. This process is extremely fast and ideal for rapid prototyping of small designs or designs printed on low-temperature substrates. The limitation remains scaling up for industrial applications, in which case thermal annealing is still the most widely used method.

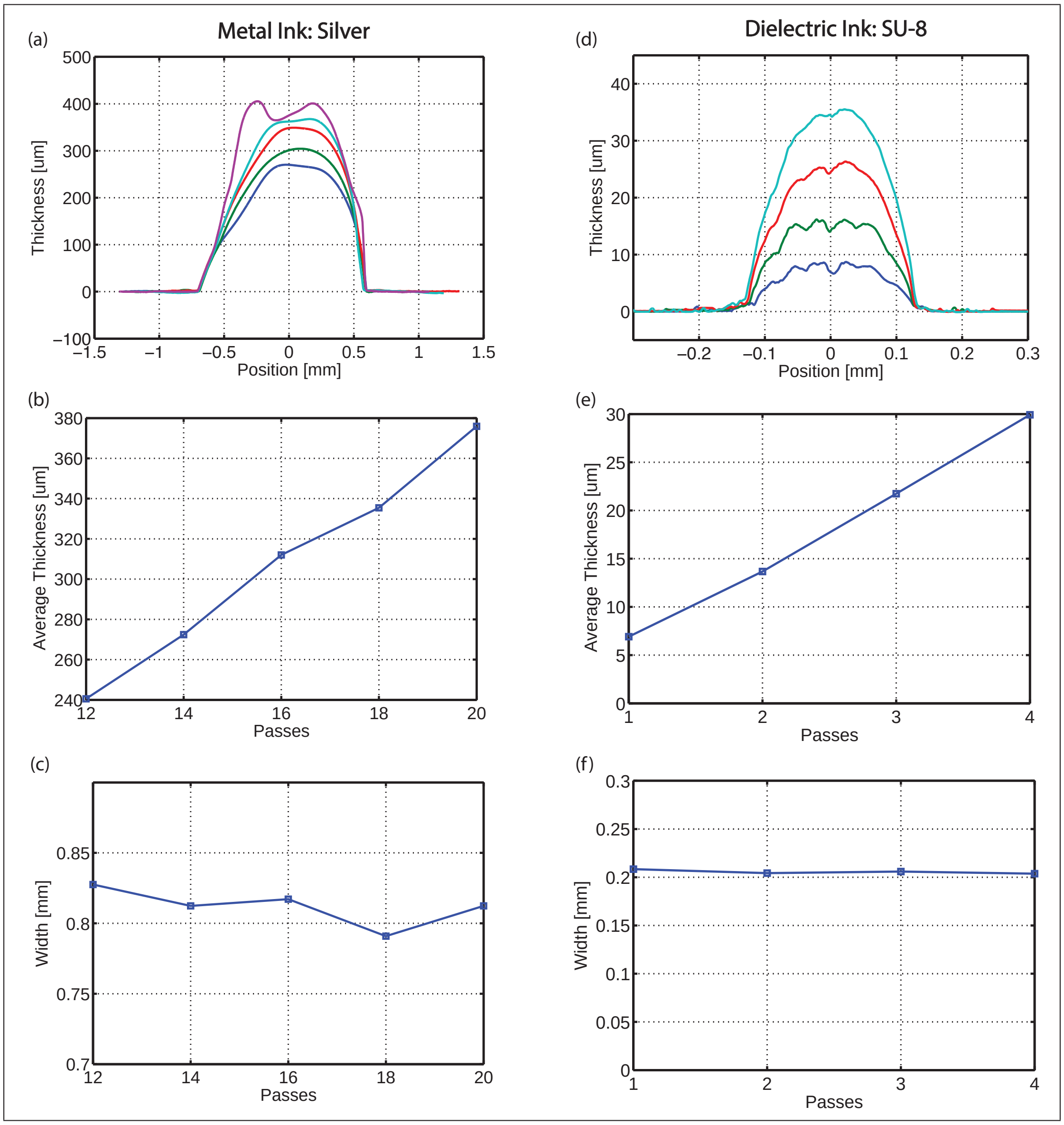

Figure 1.6 Effect of multi-pass on cross-sectional profile, line thickness and line width of printed metal (left side, a,b,c) and dielectric ink (right side, d,e,f)

In chapter 2, the silver pads and conductors are selectively laser sintered as to not damage the plastic substrate. This proved crucial in keeping the processing temperature below 150 °C, and keeping compatibility with flexible substrates.

UV exposure

For printing, organic dielectrics are preferred over inorganic dielectric inks due to their low-cost, easy processing and good printability. One of the main advantage of using epoxies is that the thermal annealing can be replaced by UV curing. This works on the principle of polymerization instead of evaporation. On exposure to the ultraviolet radiation, the polymer chains get cross-linked, thereby creating a rigid film. It is not only a faster process but also more compatible with low temperature substrates. As a result, printing can be carried out on more fragile substrates, including paper, PET, plastic and others.

The SU-8 transmission line dielectrics in chapter 3 and 4 are cured using UV. The cross-linked SU-8 polymer is mechanically stable and serves as a solid base for the silver signal conductor. Besides the demonstrated transmission lines and microwave resonators, filters and diplexers are also envisioned with this method.

1.5 Challenges

In the section, some of the commonly faced challenges related to the quality and reliability of the aerosol jet printing process are discussed. The printing quality directly depends on numerous factors, such as the substrate surface energy, interfacial interactions, ink properties (surface tension, viscosity, etc.), and the process conditions.

1.5.1 Surface Energy Mismatch

The effect of energy mismatch between the aerosol jet printed ink and the substrate is shown in Figure 1.7. The functional ink is SU8-2002 from Microchem printed on top of a glass substrate. As a result of surface energy mismatch, the dielectric printed on the substrate balls up, which results in discontinuous printing. To improve wettability, the glass substrate is pretreated by O_2 plasma. The high energy radicals break the molecular bonds on the surface. The free radicals in the presence of oxygen can react to form functional groups on the surface of the substrate. This increases the surface energy of glass substrate and improves the intermolecular interaction with the resin.

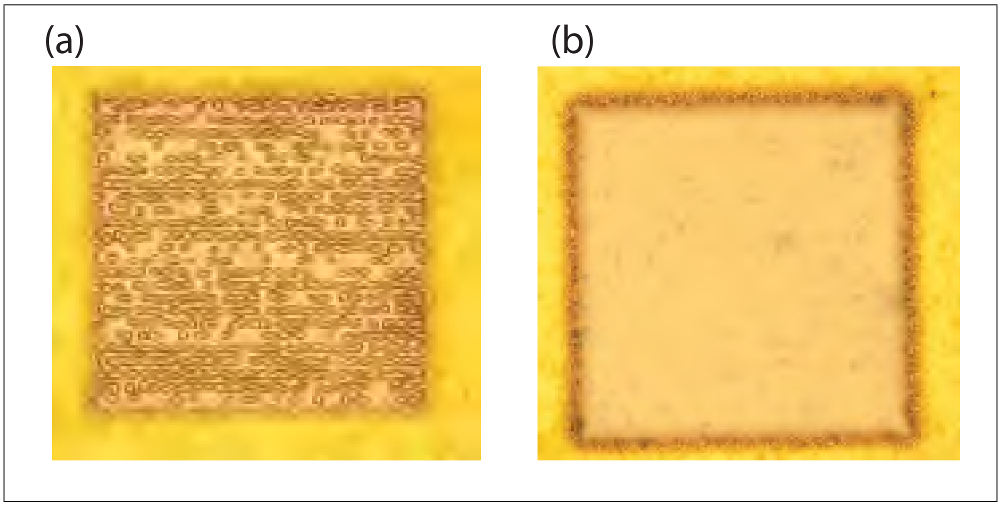

Figure 1.7 Surface preparation before the printing process: (a) Discontinous film due to poor wettability of resin on glass ; (b) Improved wettability after O_2 plasma treatment

1.5.2 Misalignment

Aerosol jet printing is capable of printing features with a resolution as small as 10 μm. While printing multi-layered structures, or on top of pre-patterned structures, alignment becomes critical for the fabrication of functional devices. Figure 1.8 shows the misalignment of the successive layers due to a slight shift of the substrate.

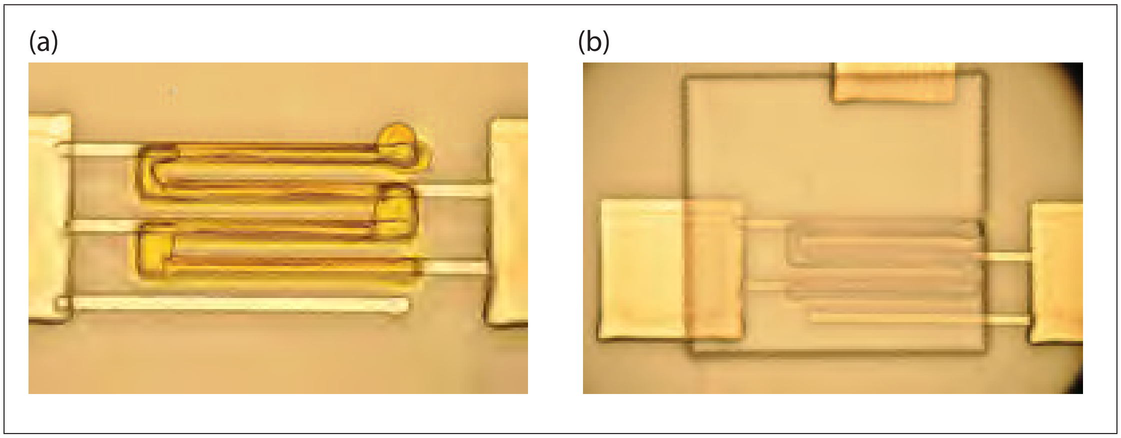

Figure 1.8 Misalignment caused by the shifting of the substrate

Even a slight misalignment due to the shift or rotation of the substrate can disrupt the complete process run. Some common causes of misalignment are a change in the substrate position when it is moved to another equipment for an intermediate step (thermal annealing, microscopy or profilometry), or a shift due to weak vacuum. Replacement of nozzles or ink during the printing process is another reason. Any of these aforementioned steps does not only disturb the alignment of the printing head with respect to the substrate but also changes the calibration of the printing head with respect to the laser and alignment camera. In order to resolve this problem: (1) Alignment markers should be used in all corners of the design to adjust the positional as well as rotational misalignment; (2) Followed by any change in printing setup, re-calibrate the printing head with respect to the camera as well as the laser.

Each of the designs in chapter 2, 3 and 4 included multiple 1 mm by 1 mm crosses as alignment marks to align multiple printing layers. With a single alignment mark, the translation of the substrate can be compensated for. In order to also cancel the rotation of the substrate, a minimum of two alignment marks are required, such that the rotation angle of the substrate can be measured. The best example of the importance of alignment is the printed MMIC transmission line in chapter 3, where the transmission line conductors has to precisely line up with the MMIC bondpads without creating shorts. This was achieved by using the center of several MMIC bondpads as alignment markers.

1.5.3 Overspray and Satellite Deposition

The resolution of aerosol jet printing is limited by the problem of overspray. It becomes critical at smaller pitch as it can result in short circuits. Few examples where the detrimental effect of overspray can be clearly observed are shown in Figure 1.9 (a) inductor, (b) capacitor and (c) silver interconnects printed from the bond pads (60 μm * 60 μm) to the package. In all these cases, the line width is critical and any overspray or overflow can result in a short.

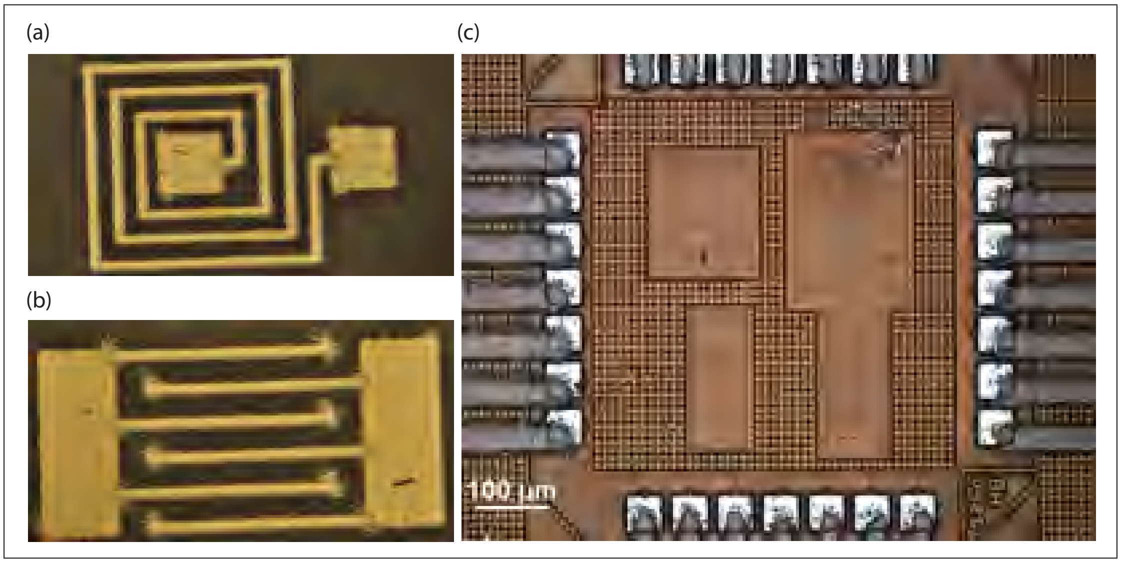

Figure 1.9 Overspray illustrated with the help of (a) Inductor, (b) Capacitor and (c) Interconnects

In Figure 1.9 (b, c), it can be noticed that the overspray is dominant at the end of the printed lines. This can be explained by the opening and closing of the shutter, which breaks the flow of the printing beam, thereby causing overspray.

In general, the reason behind overspray is not completely understood. From the experimental results, it is observed that the main factors that can help to reduce overspray are optimization of sheath gas flow, material flow and working distance. Firstly, the sheath gas used for focusing the printing stream must be optimized. At low pressure, it is unable to focus the carrier gas carrying functional material and at high pressure, it tends to become turbulent because of the pressure build up inside the nozzle. Secondly, a sufficient amount of material should be carried to the deposition head to form a good flow. A large amount of material leads to overflow, but when the material to be deposited is not enough, the sheath gas tends to scatter it. Lastly, we suggest to reduce the working distance between the printing head and the substrate, so that it is in the focal depth of the printing beam.

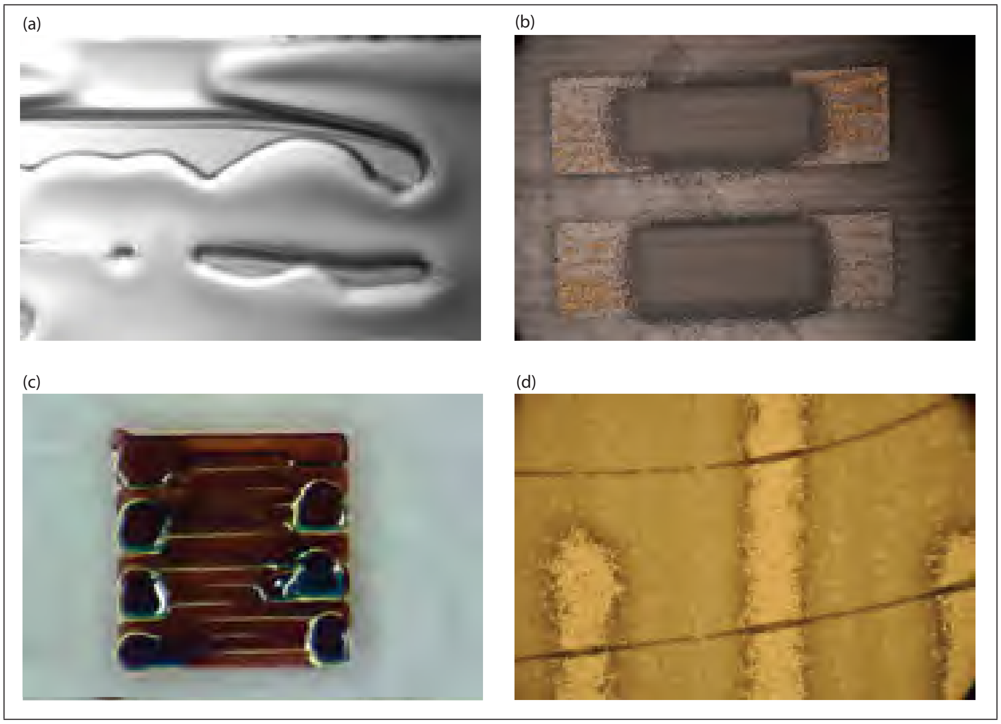

Figure 1.10 Other printing problems (a) Drying effect (b) Foaming due to surfactant (c) Acceration time (d) Cracking due to thermal co-efficient mismatch

1.5.4 Other Problems

Some other common problems faced during the printing process are shown in Figure 1.10. The rapid drying of the printed material results in drying effects as shown in Figure 1.10 (a). This is detrimental for film formation. It can be avoided by reducing the platform temperature in order to slow down the ink drying process. In section 1.4.1, we discussed the limitation of ultrasonic atomizer being unable to print ink formulations containing surfactants. In Figure 1.10 (b) the white layer shows the foam, which is printed by UA onto the substrate. Figure 1.10 (c) shows the overflow of the material at the edges. This happens because the printing head deposits more material towards the edges before the ink could dry. Adjusting the acceleration time can reduce this problem. In Figure 1.10 (d) silver is printed on top of a dielectric and is subsequently thermally annealed. As a result of thermal co-efficient mismatch, the dielectric has cracked.

1.6 Conclusion

In this chapter, we first introduced the operating principle of the aerosol jet deposition system. Next, we described the system components for a better understanding of the process and parameter control. Under the process optimization, the procedure was differentiated into 4 distinct steps: (1) ink selection, (2) surface treatment (3) process control and (4) post-processing. The first step explained the importance of the consideration of key parameters, such as viscosity, vapor pressure, surface tension, particle size and encapsulant. The second step briefly discussed the different ways in which surface energy match between the substrate and ink can be achieved. The third step gave the detailed explanation of how the line width, thickness and profile can be controlled. The final step mentioned the different ways in which the post-processing of printed film can be carried out, such as thermal, laser or UV exposure. In the last section of the chapter, we showed the different types of challenges commonly faced during the printing process and how these problems could be resolved. In the following three chapters, these results were used for the development of different promising applications.

PREFACE: CHAPTER 2

In the introduction, a background for printed photodetectors was given, including the operating mechanism, measurement characteristics and state-of-the art. In chapter 1, an overview of AJP as a printing technique was provided. In the next chapter, the application of AJP in the field of photodetectors is explored. In the last few decades, considerable effort has been made to fabricate morphologies having high surface area to volume ratio in order to achieve better performance metrics. The drawbacks of these fabrication techniques include either a high processing temperature, tedious fabrication techniques or precisely engineered nano materials. Notably, the device performance of printed photodetectors is not comparable to those which are fabricated using traditional techniques. In this work, fully printed UV photodetectors on flexible substrates, with complete processing carried out below $<150^{o}$C, are reported. Here, the choice of AJP in comparison to other direct printing technique is based on its ability (1) to print pre-synthesized large ZnO crystals ($\sim$ 1 μm) without clogging; (2) and to print a dispersion ink formulation. The two main advantages of depositing ZnO crystals instead of the precursor ink is a reduced post-annealing temperature, and obtaining high surface area-to-volume ratio at much lower cost. Due to the low cost of the ink formulation, with more research efforts these devices show a great promise with other high throughput roll-to-roll printing processes.

CHAPTER 2

FULLY AEROSOL JET PRINTED, HIGH-PERFORMANCE NANO-POROUS ZNO ULTRAVIOLET PHOTODETECTORS

Anubha Gupta[1], Shivaram Arunachalam[1], Sylvain G. Cloutier[1], Ricardo Izquierdo[1]

[1] Electrical Engineering Department, École de Technologie Supérieure,
1100 Notre-Dame Ouest, Montréal, Québec, Canada H3C 1K3

Article published in ACS Photonics in September 2018.

2.1 Abstract

We report fully aerosol-jet printed ultraviolet photodetectors based on zinc oxide nano-crystal networks having a porous morphology. The developed photodetectors exhibit selective optical photo response in the ultraviolet spectrum at wavelengths ranging from 250 nm upto 400 nm. These devices show a high ON/OFF ratio of $\sim 10^6$ and short response times. The characteristic time constants for the rise and fall edges were measured to be $\sim$0.4 s and $\sim$1.3 s, respectively. In this work, we propose a direct approach for aerosol printing pre-synthesized nanocrystals to overcome the limitations of high post-annealing temperatures and tedious fabrication methods to obtain high aspect ratio nanostructures. The high performance characteristics of these devices are attributed to Schottky barrier modification under the influence of oxygen, which is enhanced by the porosity of the semiconductor material. The random orientation of the crystals aids the formation of air traps in the network, thereby enhancing the surface area-to-volume ratio. Most importantly, the complete processing of these devices is performed below 150 ^{o}C, which makes this technology compatible with the processing on a wide range of mechanically flexible, recyclable or inexpensive substrates such as paper and plastics.

2.2 Introduction

Printed electronics is a fast developing field, promising low-cost fabrication on large area substrates, with applications in photonics, RFID tags, digital logic, sensors, etc. In particular, due to the low temperature processing, electronics can be printed on unconventional substrates such as conformal plastics and flexible PET. Printed UV photodetectors are of significant interest for missile detection, chemical and biological threat interception, environmental pollution monitoring, optical communications and others (Monroy *et al.*, 2001; Varenne *et al.*, 2008; Cheng *et al.*, 2004). ZnO (among other metal oxides such as, Ga_2O_3, SnO_2, In_2O_3, ZnGeO and $InGe_2O_7$) shows great potential as a UV photodetector (Basak *et al.*, 2003) due to its direct-wide band gap of 3.37 eV at room temperature and a corresponding band absorbance of 250-400 nm (Ozgur *et al.*, 2005).

Several morphologies of ZnO nano-materials have been proposed to achieve enhanced photosensitivity due to their large surface area-to-volume ratio (Zhou *et al.*, 2009; Cheng *et al.*, 2011), since the background oxygen concentration has a prominent effect on the behavior of ZnO semiconductors (Kind *et al.*, 2002). In particular, ZnO nanoparticle detectors were shown to have reduced dark currents as well as increased responsivity.(Jin *et al.*, 2008) Single nanowire detectors have been reported to have similar properties (Kind *et al.*, 2002; Cheng *et al.*, 2011; Liu *et al.*, 2014; Law & Thong, 2006; Hullavarad *et al.*, 2009), and the photocurrent can be scaled up by increasing the number of nanowires (Bai *et al.*, 2011). Alternative structures such as microtubes (Cheng *et al.*, 2008), nanorods (Hassan *et al.*, 2013), nanospheres (Hullavarad *et al.*, 2007) and tetrapods (Mishra *et al.*, 2015) have also been proposed. However, these structures either require high processing temperatures (Chen *et al.*, 2009), tedious fabrication techniques such as electro spinning (Liu *et al.*, 2014), vapor deposition techniques which require vacuum processing (Kind *et al.*, 2002) or precise control of the synthesis and morphology of the nano-materials (Wang, 2004; Lupan *et al.*, 2008), which impede their use in scaled-up fabrication.

On the other hand, efforts have been made in solution processing for the fabrication of thin film ZnO photodetectors (Li *et al.*, 2014; Jin *et al.*, 2008; Panigrahi & Basak, 2012; Konstantatos & Sargent, 2010). However, processing techniques like screen printing, spin coating and dip coating waste a large fraction of the material inks, leading to higher costs in the fabrication process. The use of digital-write additive techniques, such as inkjet printing can significantly reduce material waste by 94-97% (Haverinen *et al.*, 2010) . However, the narrow allowable viscosity range of the inks in ink-jet processing limits the amount of usable materials. Moreover, the risk of nozzle clogging reduces process throughput. Recently, direct-writing techniques have attracted interest for the fabrication of ZnO thin films, although a processing temperature of 200^oC-400^oC is still required to anneal the precursor ink(Winarski *et al.*, 2018).

In this work, we demonstrate a first fully-printed, low temperature processed nano-porous ZnO photodetector on rigid as well as flexible substrates. The entire device is fabricated using Aerosol Jet Printing (AJP), a digital-write fabrication method capable of printing inks with a wide viscosity difference ranging from 1-1000 cP and with improved resilience to nozzle clogging. Recently, printing of ZnO precursor ink formulations have been explored with AJP(Winarski *et al.*, 2018; Hong *et al.*, 2013). However, it has not been so far employed to print directly from a pre-synthesized nano-crystal ink. In this study, the aerosol jet technique is used to deposit the ZnO nano-crystals from a dispersion ink. As the solvent evaporates, a well-connected porous film is formed having high surface roughness. As a result of this porous morphology, the devices exhibit a high surface-to-volume ratio, and show high ON/OFF ratio and fast speed, comparable in performance to previously published nanostructured ZnO photodetectors (Jin *et al.*, 2008; Liu *et al.*, 2014; Bai *et al.*, 2011). Another important aspect of this work is that the complete fabrication process is carried out below 150^oC, making it compatible for processing on large area flexible substrates.

Experimental Section

2.3 Aerosol Setup and Synthesis Procedure

Figure 2.1 (a) describes the aerosol jet printing process for the fabrication of ZnO photodetectors. In this process, a stream of inert gas is blown at high pressure over the surface of the functional ink to be printed. This generates a mist of the material which, after compression by a virtual impactor, is directed towards the deposition head. At the printing head, a second flow of inert gas called sheath gas surrounds the aerosol gas stream and guides it to the substrate, as

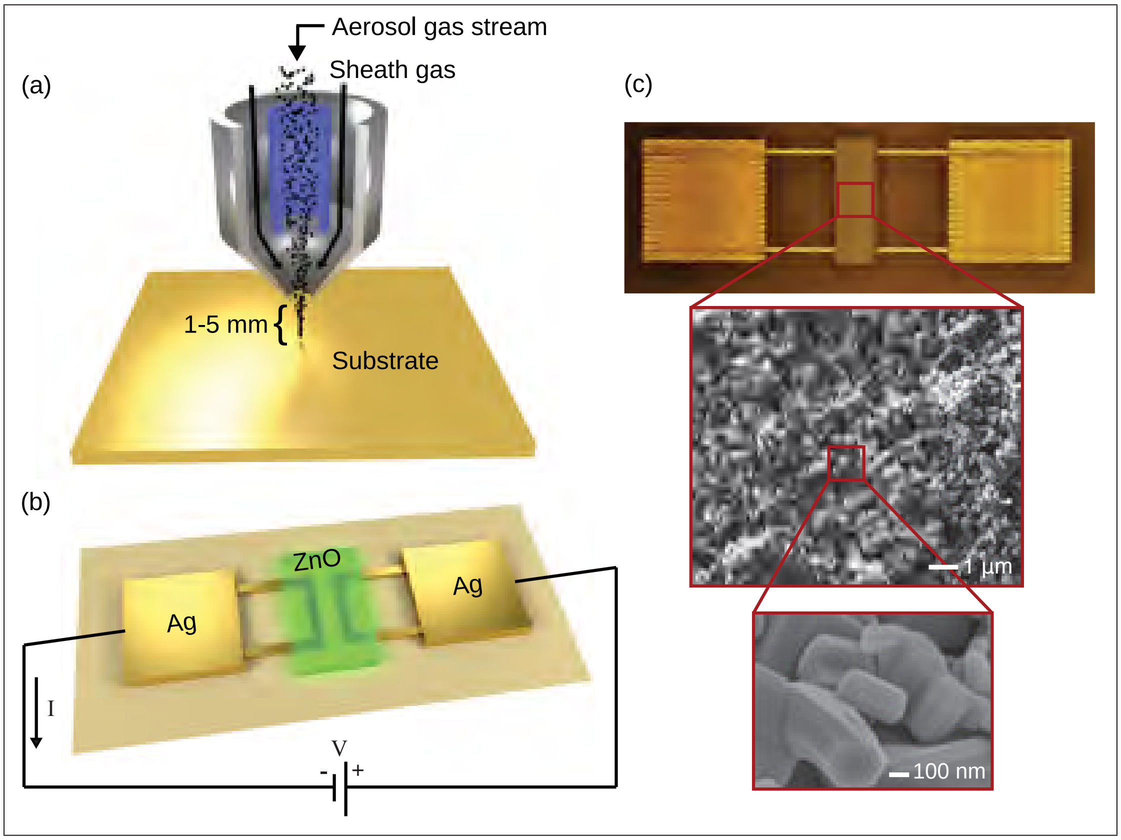

Figure 2.1 (a) Schematic illustration of aerosol jet deposition head demonstrating the aerodynamic focusing of aerosol gas stream using sheath gas; (b) Schematic diagram depicting the device architecture of the printed photodetector on PET substrate; (c) Microscope image of the device and SEM images of the ZnO films

shown in Figure 2.1 (a). This helps focusing the printing stream, thereby reducing sprayover. It also prevents the material to come in contact with the nozzle to avoid clogging. The temperature of the substrate and the feed tube to the printing head can be controlled to improve ink drying. Printed structures can be thermally-annealed or laser-sintered.

Figure 2.1 (b) shows the schematic device structure for the printed ZnO photodetectors. A pair of 1 mm^2Ag contact pads was printed to facilitate electrical probing of the device. Ag electrodes with 30 μm width and a gap of 80 μm were printed from the contact pads. A ZnO porous film was then deposited atop of the metallic contacts to form a metal-semiconductor-metal (MSM) photodetector with Ag-ZnO and ZnO-Ag interfaces.

Materials and Device Fabrication. All layers of the device were printed using a commercially available Aerosol jet printing system (AJ300 from Optomec, Inc.) under ambient environment on glass substrate or PET substrates. Prior to the device fabrication, the glass substrates were cleaned with soap solution/acetone/isopropyl alcohol/deionized water for 10 min each followed by drying with nitrogen gas. The printing of both the metal and semiconductor material was carried out using pneumatic atomizer.

The Ag metal electrodes are first printed on the cleaned substrates using commercial water-based ink HPS-030AE1 with 55-60 wt% loading from Novacentrix without further modification, while the substrate is maintained at 45 ^oC to facilitate drying. The printing profiles of this Ag ink at various substrate temperatures have been previously reported (Gupta *et al.*, 2016). The aerosol mist is then generated by fixing the virtual impactor/carrier gas flow rate 610 sccm/650 sccm. The sheath gas at a flow rate of 40 sccm is used to focus the aerosol stream. The electrodes are finally laser sintered at a power output of 100 mW with a spot size of 30 μm using built-in infrared multi-mode laser. The conductivity of Ag was measured at 10^6 S.m^{-1} using four-point probe measurement.

For printing the ZnO, the substrate temperature is elevated to 60 ^oC. The ZnO ink is prepared by mixing ZnO nanopowder (Anachemia Chemicals Inc, $>$ 99%) in distilled water (0.6 M). The gas flow rates, sheath gas/virtual impactor/carrier gas are set to 100 sccm/800 sccm/850 sccm, respectively. The tube temperature is maintained at 80 ^oC to reduce the water content of material being printed and the printing stage speed is maintained at 2 mm.s^{-1}. Both the ink formulations are stirred continuously during the printing process run. The printing is followed by annealing at 150 ^oC on a heating plate for 30 min to remove the residual solvent in controlled environment (nitrogen). The thickness of the metal electrodes and the ZnO layer are measured at 1.85 μm and 2.9 μm respectively using a Dektak XT B516 profilometer.

2.4 Material Characterization

An optical image of the fabricated device is shown in Figure 2.1 (c). The figure inset shows the scanning electron microscopy (SEM) images of the ZnO film, showing a well-connected polycrystalline porous film morphology. The magnified image shows the hexagonal symmetry of the ZnO nano-crystals with large surface-to-volume ratio. The nano-crystals were observed to have a size spreading from 100 nm up to 1 μm, in contrast with colloidal quantum dot based films having much smaller nanoparticle sizes. This alternative approach leads to a significant reduction in the cost of the nano-particle ink. For instance, a commercial ZnO nanoparticle ink with particle size spreading in the range of 7-17 nm, from Sigma Aldrich, is 20000 times more expensive than the cost of this ink.

Figure 2.2 (a) shows the X-ray diffraction pattern for the ZnO film printed on glass substrate as measured using Bruker's D8 Advance diffractometer. The pattern distinctly depicts the characteristic (hkl) peaks at 2θ angles 31.78, 34.43 and 36.27, corresponding to the lattice planes (100), (002) and (101) matching ZnO's hexagonal wurtzite structure. The high intensity of these peaks affirms the crystallinity of the material and the random orientation of the crystals as also observed from the SEM micrograph in Figure 2.1 (c).

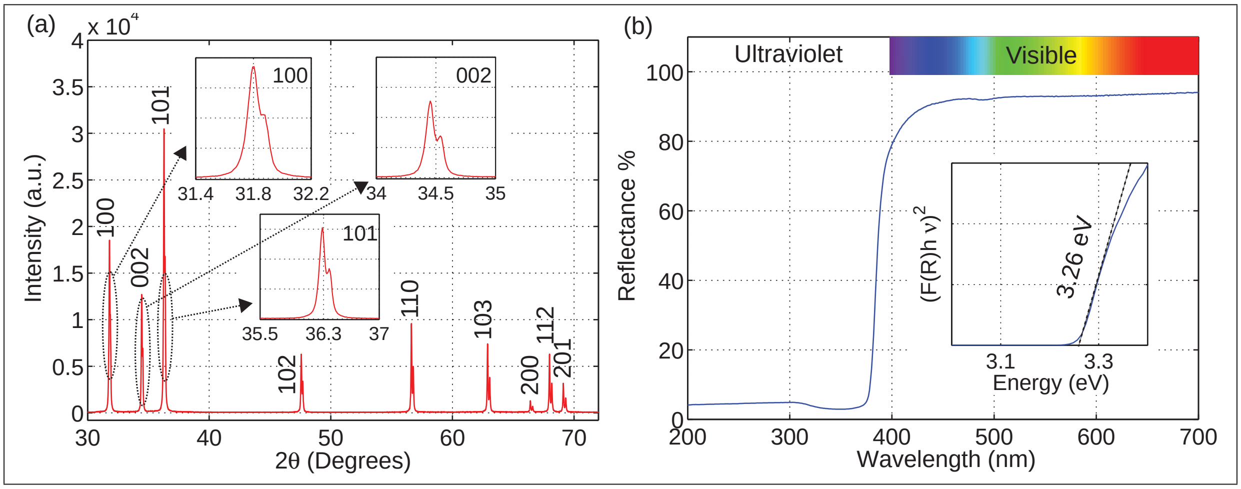

Figure 2.2 Characterization of ZnO film with (a) X-ray diffraction pattern; (b) Diffused reflectance spectra, inset indicates the Tauc's plot

The optical absorption of the ZnO film was studied using diffused reflectance spectroscopy (DRS), obtained by a double-beam spectrometer (Lambda 750) on a solid sample as shown in figure 2.2 (b). The ZnO nano-crystal film shows 85 % reflectance in the visible spectrum, compared to approximately 5 % in the UV region. The material shows low absorbance for photons with wavelength above 400 nm making it insensitive to visible wavelengths. The inset of figure 2.2, represents the Tauc's plot. From this plot, the optical band gap of the semiconductor is calculated at 3.26 eV by the extrapolation of the tangent. This energy corresponds to a wavelength of 380 nm in accordance with the literature (Ozgur *et al.*, 2005).

2.5 Optoelectronic Characterization

The optoelectronic characterization of the devices was performed using a Lake Shore probe station (Figure 2.3 (a)) in ambient environment and in vacuum. The electrical parameters of these devices were measured using an Agilent B1517A source meter. Current-voltage (IV) curves, shown in Figure 2.3 (b) on a logarithmic scale, are obtained by sweeping the bias voltage from -20 V to +20 V. The sweep was performed in the dark and during illumination under a 40 μW/cm^2 UV lamp with a dominant wavelength at 252 nm. The ratio between light and dark current, defined as the ON/OFF ratio, is approximately $\sim 10^6$. The photodetector is therefore sensitive enough to detect weak UV light intensities.

The illumination is modulated using a shutter assembly controlled by a frequency generator from Stanford Research. Figure 2.3 (c) shows the time photoresponse of the device on a linear scale when illuminated at 40 μW/cm^2 with a light source modulated at 0.05 Hz. In order to perform a detailed observation of the response speed, the pulse duration was increased and the photocurrent response was plotted on a log-linear scale in Figure 2.3(d). The plot on Figure 2.3(d) clearly shows that a steady state dark current on the order of a few pA is achieved within a short time after the illumination.

To further analyze the dynamic behavior of those devices, we perform a curve fitting on the rising and the falling edges of the time photoresponse curve. In Figure 2.3 (d), we can observe

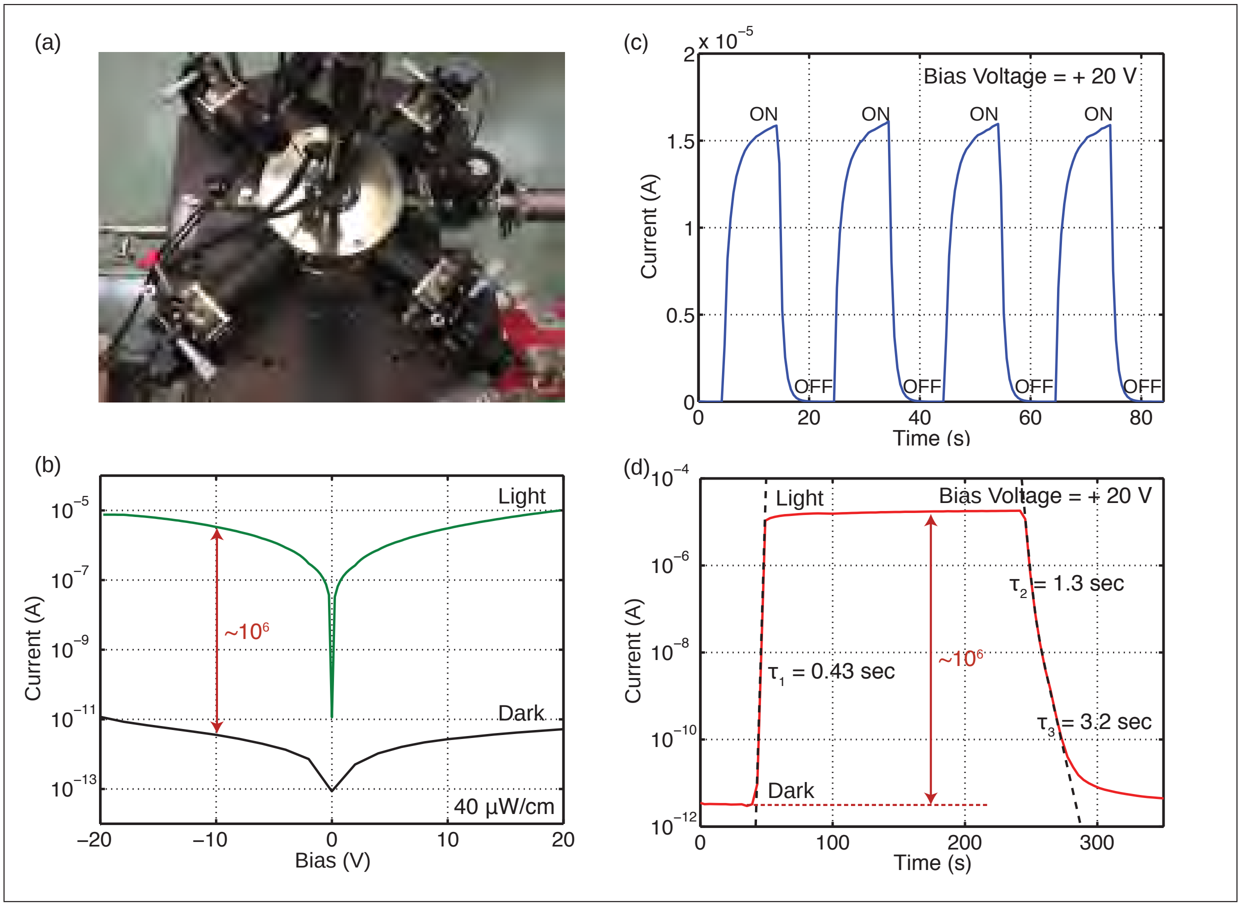

Figure 2.3 (a) Lake Shore probe station used for opto-electronic characterization ; (b) IV curves under 252 nm wavelength light illumination (40 μW/cm^2) and dark condition; Time-dependent photo current with 20V bias and 40 μW/cm^2 UV excitation (switched by a mechanical shutter) in (c) linear and (d) logarithmic scale. The rising and falling edge are fitted with a single order and double order exponential respectively

on the rising edge that, as the illumination is turned on, the photo current increases six orders of magnitude in 10 s. This behavior can be accurately fitted with a single order exponential growth, characterized by a time constant of 0.43 s. On the falling edge, when the illumination is turned off, the photocurrent first decreases by three orders of magnitude in 15 s. This first decay is followed by a second decay of three orders of magnitude which occurs this time on a 40 s period. In order to properly fit this behavior, a second order exponential fit is necessary, with a first time constant of 1.3 s and a second slower time constant of 3.2 s. This is an indication that there are two separate physical mechanisms controlling the photo decay of this device, which merits further investigation.

Figure 2.4 plots the dependence of the photocurrent on the illumination intensity in (a) ambient and (b) vacuum environment. The light intensity was measured by a standard silicon photodiode(S1226-18BQ) bought from Hamamatsu Corp. In air, the current changes by four orders of magnitude as the light intensity is increased from $2 \cdot 10^{-4}$ mW/cm^2 to $4 \cdot 10^{-3}$ mW/cm^2. The photocurrent increases with irradiance following a power law corresponding to $I_{ph} \propto P^{3.5}$, while in vacuum the response is linear with a power law fit of $I_{ph} \propto P^{1.09}$. In photoresistors and photodiodes, the photocurrent is expected to increase linearly with the number of incoming photons. Therefore, an additional mechanism is required to explain the superlinear response.

2.6 Oxygen Adsorption Mechanism

The difference in characteristics of the device between operation in air and vacuum can be attributed to oxygen adsorption mechanism on the surface of the ZnO crystals. As illustrated in the energy level diagram of the MSM photodiode structure under UV illumination shown in Figure 2.4 (c), Schottky barriers are formed on the Ag-ZnO interfaces due to difference in work functions. Absorbed photons generate excitons which are split into holes and electrons by the built-in electric field. The Schottky barriers significantly increase the speed of the device, because of the built-in electric field at the junctions (Brillson & Lu, 2011; Li *et al.*, 2014; Jiang *et al.*, 2008; Jin *et al.*, 2008) . If the barrier has a fixed height, the photocurrent scales linearly with the amount of absorbed photons.

Figure 2.4(d) explains how the Schottky barrier could be modified by oxygen adsorption. In the dark, oxygen molecules are adsorbed on the surface of the nanoparticles by capturing electrons from the n-type ZnO:

$$\mathrm{O_2(g) + e^- \rightarrow O_2^-(ad)} \tag{2.1}$$

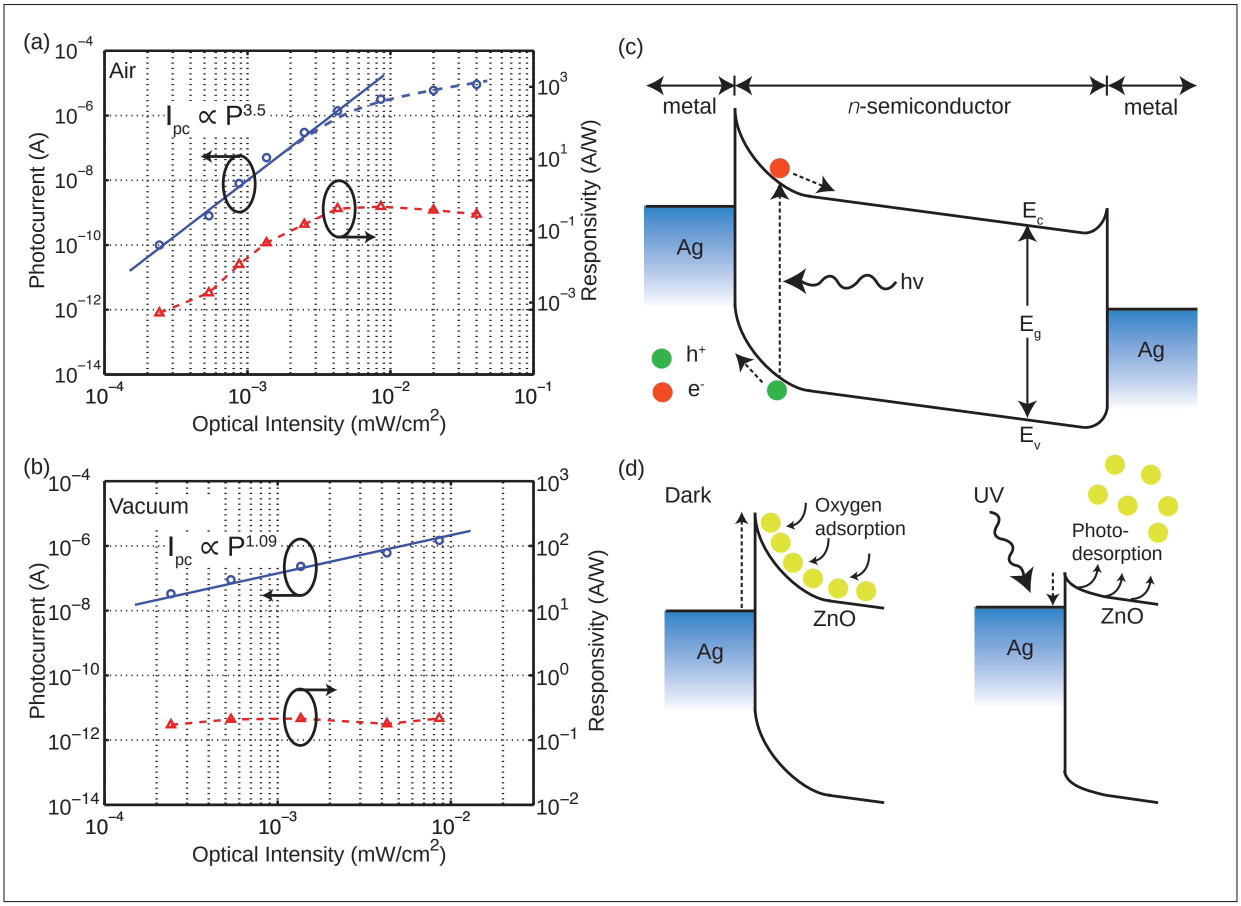

Figure 2.4 Photo current versus light intensity at 20V bias for (a) ambient air and (b) vacuum condition. A power law fit is made for both conditions. Also plotted are the responsivities, showing light sensitivity as a function of light intensity; Device energy band diagram of (c) MSM photodiode under UV illumination with external bias applied (d) barrier modification due to the adsorption and photo-desorption of oxygen under UV illumination

The oxygen adsorption increases the Schottky barrier at the Ag-ZnO interface, thereby reducing the dark current. Upon illumination, the absorbed UV photons generate excitons and the photo-generated holes release the adsorbed oxygen by the following reaction:

$$h^+ + O_2^-(ad) \rightarrow O_2(g) \tag{2.2}$$

The oxygen desorption will lead to the decrease of the Schottky barrier and results in a larger flow of charge carriers by diffusion through the junction. The current due to the illumination therefore increases in a super-linear fashion (Jin *et al.*, 2008). This modification of the Schottky barrier therefore results in a large ratio between dark and illuminated current upon adsorption of oxygen. Moreover, from this relationship,between Schottky barrier height and the amount of adsorbed oxygen, we expect that a larger contact area of the ZnO active material with air will result in a larger ON/OFF ratio.

An important metric of a photodetector is the responsivity R, which is defined as the ratio of photocurrent I_{ph} to the optical power P_{opt}:

$$R = \frac{I_{ph}}{P_{opt}} \tag{2.3}$$

The optical power P_{opt} is obtained by multiplying the optical intensity of the light source by the 80-by-1000 μm active area of the device. The responsivity as a function of the illumination power density, when a 20V bias is applied, is plotted on the right axis of Figure 2.4 (a) and (b). As we can see on the figure, in the air, the responsivity increases with optical power due to the superlinear rise in photocurrent. We can attribute this behavior to the Schottky barrier modulation mechanism described above, which controls the injection of charge carriers into the ZnO film. In contrast, the device shows constant responsivity in vacuum, which is consistent with a transport-limited photocurrent in photoconductor.

2.7 Film Porosity

In order to quantify the influence on the performance of the photodetector of an enhanced surface-area-to-volume-ratio, a reference device, with similar dimensions and a non-porous film morphology, was fabricated. For the printing of this film, a water-based precursor ink synthesized from $Zn(NO_3)_2.6H_2O$ (0.15 M) was used, followed by the post-annealing at 350^oC. The precursor ink was prepared in accordance with the recipe reported by K. Hong et al (Hong *et al.*, 2013). The surface topography of the printed film was studied by AFM as shown in Figure 2.5 (a). The 3-dimensional AFM topography image (10 μm x 10 μm) exhibits a smooth and continuous surface. The root-mean-square (RMS) surface roughness was measured to be 18.40 nm.

The measured current of the devices with porous and non-porous ZnO film , when switching the illumination On and OFF, are shown in Figure 2.5 (b). It is clear that the non-porous film exhibits an ON/OFF current ratio that is three orders of magnitude lower than for the porous film. This confirms that the operating mechanism of the photodetector is dominated by surface effects and that a large surface-to-volume ratio is beneficial to get a high ON/OFF ratio.

2.8 Flexible Substrates

As the entire fabrication process of the ZnO photodetectors is performed below 150 ^{o}C, it is compatible with temperature sensitive plastic substrates. This enables applications in large area and flexible electronics. To demonstrate this, identical photodetectors were fabricated on a PET substrate, as shown in Figure 2.5 (c). The measured IV curves for the devices in the dark and under illumination are displayed in Figure 2.5 (d). These devices deposited on a PET substrate show a high ON/OFF ratio $\sim 10^6$, akin to devices produced on a glass substrate.

Paper	ON/OFF Ratio	Incident Power	Rise Time	Fall Time	Processing Temp.	Morphology	Method
		[μW/cm^2]	[s]	[s]	[^{o}C]		
This work	$\sim 10^6$	40	0.43	1.3 / 3.2	150	Nano-porous	Printed
(Cheng *et al.*, 2011)	$4 \cdot 10^5$	7600	N/A	0.05	N/A	Nano-wire	Thermal evaporation
(Jin *et al.*, 2008)	$\sim 10^6$	830	<0.1	1.31	250	Colloidal nanoparticle	Solution
(Liu *et al.*, 2014)	$\sim 10^5$	100	0.56	0.32	420	Nano-wire	Electro spinning
(Bai *et al.*, 2011)	$8 \cdot 10^4$	4500	N/A	14	N/A	Nano-wire	CVD
(Cheng *et al.*, 2008)	$\sim 10^5$	21700	2.9	100	1300	Micro-tube	Microwave heating
(Hassan *et al.*, 2013)	$6 \cdot 10^2$	1500	4.8	7.3	900	Nano-rods/tetrapods	Thermal evaporation
(Hullavarad *et al.*, 2007)	$\sim 10^2$	N/A	3.9	1.7	900	Nano-wire/micro-sphere	Direct Vapor Phase
(Mishra *et al.*, 2015)	$5 \cdot 10^2$	N/A	0.04	0.05/1.2	1100	Tetrapod	Flame transport synthesis
(Chen *et al.*, 2009)	$\sim 10^2$	N/A	N/A	N/A	650	Thin film	Sol-gel
(Li *et al.*, 2014)	$\sim 10^3$	1500	N/A	> 2.9	150	Crystal film	Solution
(Panigrahi & Basak, 2012)	$\sim 10^3$	N/A	<0.3	<0.3	500	Nano-rod	Solution
(Winarski *et al.*, 2018)	$\sim 10^5$	24000	N/A	N/A	400	Thin film	Printed
(Jiang *et al.*, 2008)	$\sim 10^3$	N/A	20n	250n	400	Thin film	Sputtering

Table 2.1 Performance comparison of published ZnO UV photodetectors

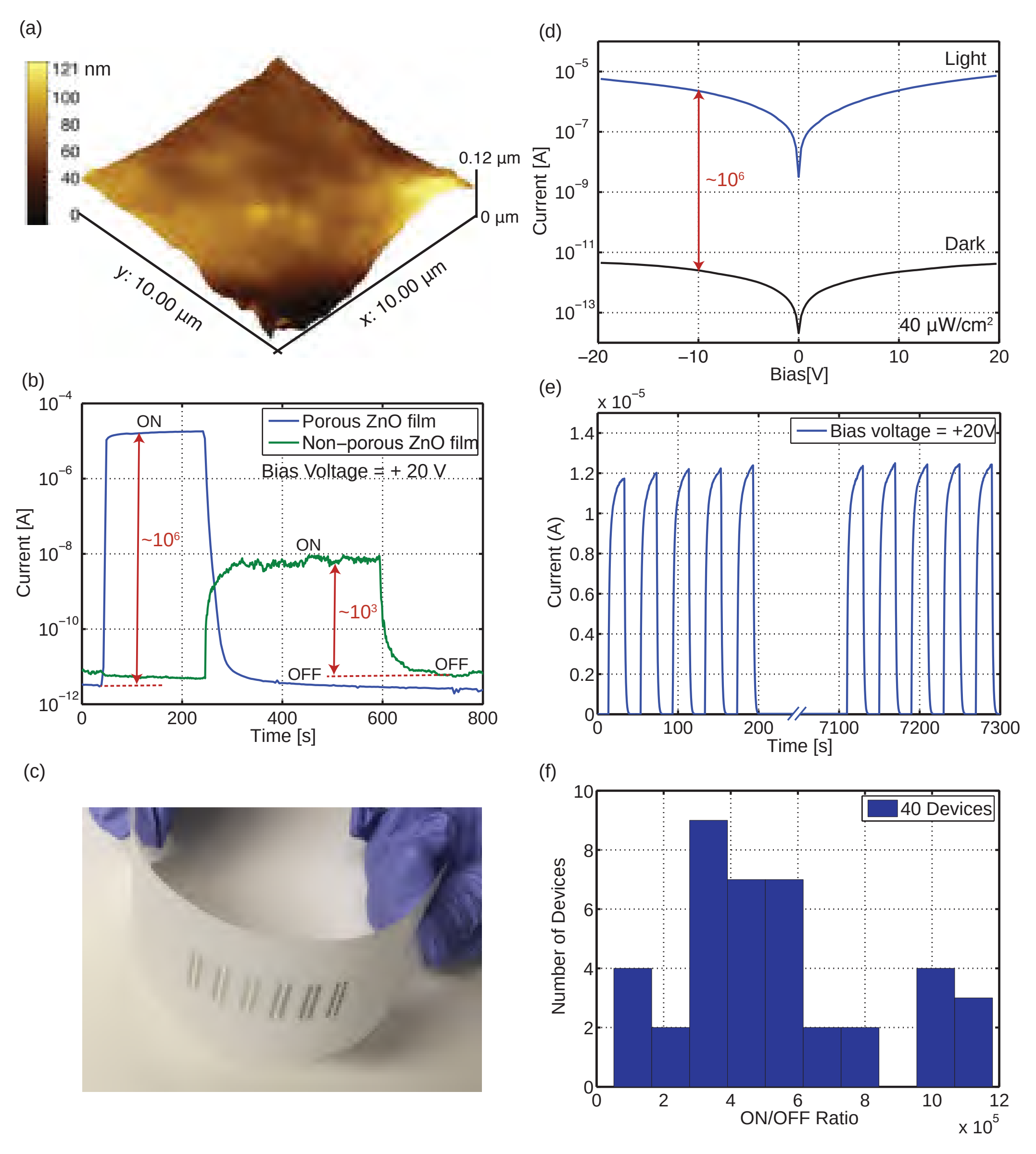

Figure 2.5 (a) AFM image of non-porous ZnO film, detailing a smooth, crystalline surface; (b) Comparison of time-dependent photocurrent in photodetector with porous and non-porous ZnO film under switching 252 nm wavelength light source; (c) Optical image of fully aerosol-jet printed array of ZnO photodiodes on a mechanically flexible PET substrate, with $< 150^{o}$C processing; (d) IV curve demonstrating same order of ON/OFF ratio for a device printed on flexible substrate as on rigid substrate; (e) Repeatability of time-dependent photo current tested for over 2 hours duration with 20V bias and 40 μW/cm^2 UV excitation (switched by a mechanical shutter) on PET substrate, plotted in linear scale; (f) Histogram of ON/OFF ratio measured for 40 devices on PET substrate as shown in Figure 2.5(c)

Next, the stability and the reproducibility of these devices are examined. The stability is tested by illuminating the sample with a UV light source, modulated at 0.025 Hz for ∼2 hours. As shown in Figure 2.5 (e), the photocurrent of the detector remains unchanged over two hours and no degradation in the device performance is observed. These measurements verify that the printed photodetectors exhibit good stability over time. Figure 2.5 (f) shows the histogram of the statistical variation in ON/OFF ratio for 40 devices. All devices have an ON/OFF ratio ranging from 10^5 to 10^6. It shows that this process is suitable to give reproducible results over multiple devices.

Performance Comparison Finally, we summarize the state-of-the-art in the field of ZnO ultraviolet photodetectors with their performance metrics and fabrication methods in Table 2.1. From the table, it can be observed that this work reports the highest ON/OFF ratio while using the lowest incident optical power. The processing temperature is among the lowest reported, which enables the use of temperature sensitive substrates, thus making it ideal for large-area electronics.

Conclusion. In summary, we used aerosol jetting for the fabrication of a fully-printed ZnO UV-photodetector on glass and flexible PET substrates. The device architecture consists of a nano-porous ZnO film with high surface-to-volume ratio, contacted with Ag electrodes. Well-controlled experiments show a linear increase in photoresponse current with illumination under vacuum and a superlinear increase in air. To explain this phenomenon, we proposed a Schottky barrier-modification mechanism upon adsorption and desorption of oxygen, and verified the hypothesis with experimental results in both vacuum and air. The performance was comparable to state-of-the-art nano-structured ZnO photodetectors with low dark current, high ON/OFF ratios and fast response time. These AJ-printed thin film devices offer significant advantages over other fabrication methods: (a) Increased film porosity enhances the surface-area-to-volume-ratio while not requiring precise control over the morphology and size of ZnO nanocrystals, thereby significantly reducing the manufacturing cost. (b) The printing approach makes the fabrication process easily scalable to large area substrates. (c) As these devices are fully printed with low-temperature processing ($< 150^o$C), flexible and plastic substrates can be used that enable novel applications.

2.9 Acknowledgement

The authors would like to thank NanoQAM, NSERC, the Canada Research Chair program, ReSMiQ and CMC microsystems for financial support. We would like to thank Prof. Mohamed Siaj and Dr. Michiel Soer for valuable discussions and technical assistance. The authors would also like to thank Gwenael Chamoulaud for his assistance with the AFM.

Discussion

In this chapter, the large ON/OFF ratio of the ultraviolet photodetector was attributed to the modification of the Schottky barrier at the Zno-Ag interface. It was assumed that the ZnO film can be treated as a crystalline continuous medium, which can be represented as a simple semiconductor material in the band diagram of the device. In practice the film is composed of nano crystals which are sintered together at a comparatively low temperature. The question therefore arises if there are additional barriers between the ZnO nano crystals which are also modified by oxygen adsorption, thereby providing an alternative mechanism to the Schottky barrier.

To gain insight into the primary injection limitation, the photodetector was fabricated with aluminum electrodes. Aluminum has a work function that is close to the electron affinity of ZnO, and as a result an Ohmic contact is formed at the electrodes. The measured ON/OFF ratio of the aluminum electrode device was measured to be in the order of 10^3, in contrast to an ON/OFF ratio of 10^6 for the silver electrode device. Furthermore, the ON/OFF ratio of the non-porous film device is similar to the aluminum electrode device. We can therefore conclude that the Schottky barrier at the ZnO-Ag interface is responsible for the improved ON/OFF ratio, and that any barriers at the ZnO nano crystal boundaries are not likely to be a primary influence.

PREFACE: CHAPTER 3

In the previous chapter, the application of AJP for the printing of a nano-porous photodetector was demonstrated, taking advantage of AJP's ability to print large sized particles and dispersion inks. Another advantage of the AJP system is its wide viscosity range, which can be used in the printing of high weight % loading inks. As a result, thick dielectrics as well as high aspect ratio conductors can be created. These properties are utilized in the next chapter to print a low loss microwave transmission line for semiconductor packaging applications. Either flip chip or wirebonding is used in industry to package semiconductor dies. Wirebonding is very cost efficient, but introduces wire inductance which limits wideband microwave and millimeter wave applications. In contrast, flip chip packaging has much lower parasitic inductances but requires a costly fine pitch interposer. In this work a packaging technique with in-package AJP printed transmission lines is proposed. The application of this technique is in providing high-bandwidth connections in low-cost plastic packages for high-frequency microwave and millimeter wave applications. Because AJP has an aerosol beam that is focused over several millimeters and because it can print a thick dielectric, the transmission line can bridge the height difference between a package lead and the bondpad of a silicon die.

CHAPTER 3

AEROSOL-JET PRINTED TRANSMISSION LINES FOR MICROWAVE PACKAGING APPLICATIONS

Anubha Gupta[1], Michiel C.M. Soer[1], Mohammad Taherzadeh-Sani[1], Sylvain G. Cloutier[1], Ricardo Izquierdo[1]

[1] Electrical Engineering Department, École de Technologie Supérieure,
1100 Notre-Dame Ouest, Montréal, Québec, Canada H3C 1K3

Article submitted for review to IEEE Transactions on Components, Packaging and Manufacturing Technology in February 2019.

3.1 Abstract

This paper presents a low loss microstrip line, entirely fabricated using aerosol-jet printing (AJP) technology directly to a MMIC chip to achieve high-speed on-chip connectivity. AJP is a direct write fabrication method capable of printing materials with viscosity ranging from 1-1000 cP, with a printing resolution and alignment precision of 10 μm and 2 μm respectively. The length of the printed transmission line is 2 mm and the S-parameters are measured from 500 MHz to 18 GHz. In this paper, the microstrip line is first printed on PCB and the fabrication process is optimized to reach a transmission loss of 0.3 dB/mm at 18 GHz. Subsequently, the microstrip line is printed atop an MMIC architecture to achieve a transmission loss under 0.9 dB/mm at 18 GHz. These results clearly show the potential of using direct printing of microstrip lines as an alternative to conventional wire bonding for wide-bandwidth MMIC electronics packaging applications.

3.2 Introduction

Recent progress in monolithic microwave integrated circuit (MMICs)(McQuiddy *et al.*, 1984; Midford *et al.*, 1995; Hauhe & Wooldridge, 1997) will lead to more affordable high-frequency solutions for the Internet of Things (IoT) and wearable electronics using cell phones, ASICs and memory devices with high communication rates. The packaging of microwave chips is mostly done using either flip-chip or wire bonding(Palesko & Vardaman, 2010). In spite of their widespread use, the two techniques face the same time fabrication challenges as well as performance limitations.

The main challenges of the flip-chip approach include the PCB-induced transmission line resolution and tolerance limits and the lack of a well-characterized, microwave frequencies capable material, with a thermal coefficient that matches with the PCB (Zwick *et al.*, 2006). Moreover, fabrication of specific pitch interposers requires high-resolution photo-lithography with high-precision machining and alignment techniques which makes the prototyping process quite expensive(Parker, 2002; Schepps & Rosen, 2002; Kitazawa *et al.*, 2000; Jain, 2000; Oppermann, 1998).

In contrast, the wire bonding of dice suffers from impedance mismatches at high frequencies for wide-bandwidth applications(Bessemoulin *et al.*, 2004; Kim *et al.*, 2000), due to the inductance of the bondwire (1 nH mm^{-1}). Designers endeavor to shorten the RF wire-bonds in order to minimize the total inductance, but this also limits the length of supply and control connections. Thus, chip-on-board (COB) shortens the RF connection to the PCB and improves the high frequency performance as compared to wire bonding in Quad Flat No-lead (QFN) packages by reducing the bondwire inductance (Liu *et al.*, 2009).

In the meantime, printed electronics is a rapidly emerging field, enabling cheap prototyping with fast turnaround. Direct-writing additive techniques, such as ink-jet and aerosol-jet printing offer cost-effective fabrication on large area substrates by significantly reducing the material waste compared to more traditional processing methods such as spin-coating and photo-lithography(Haverinen *et al.*, 2010). During the last decade, ink-jet printing technology has found diverse applications in the field of microelectronics in the fabrication of components such as resistors, capacitors, inductors, thin-film transistors and antennas(Jung *et al.*, 2013; Kang *et al.*, 2012; Tseng & Subramanian, 2009; Rida *et al.*, 2009; Chung *et al.*, 2015). Compared to ink-jet printing, aerosol-jet printing (AJP) has much higher printing resolution ($\sim$10

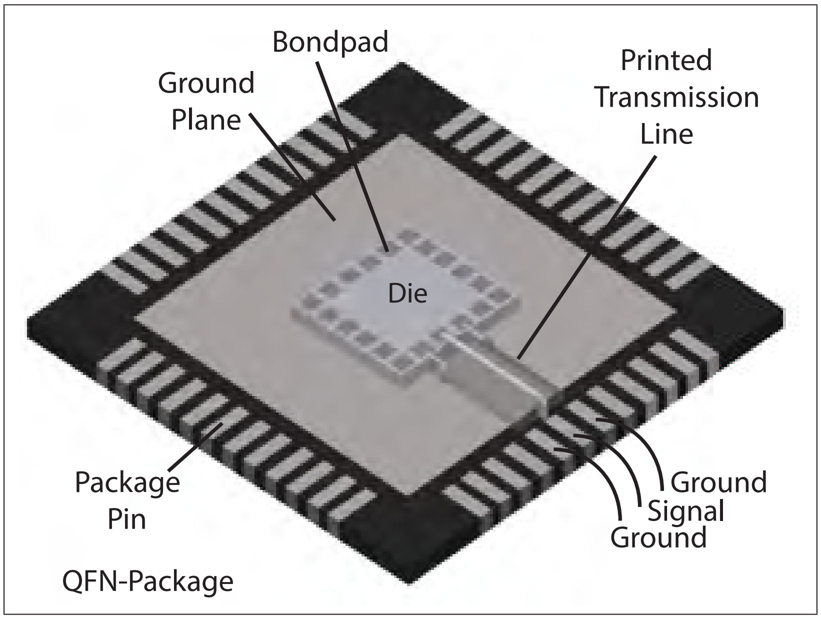

Figure 3.1 Concept drawing of a printed transmission line in a QFN package as a replacement to wire-bonding for high frequency applications. The QFN thermal pad acts as the ground plane, while the MSTL connects the Silicon MMIC to the QFN package pins

μm) and alignment precision ($< 2\ \mu$m). AJP operates on the principle of generating an aerosol mist of the material to be deposited, which is carried to the deposition nozzle by using an inert gas flow. It is capable of printing a wider range of materials, with viscosity ranging between 1-1000 cP and a significantly-higher resilience to clogging. As a result, a large variety of metallic, semiconductor and dielectric inks can be processed using a single technique.

Ink-jet and aerosol-jet printing have been used to print transmission lines (Azucena *et al.*, 2008; Liang *et al.*, 2015; Cai *et al.*, 2014, 2016). Azucena *et al.* first reported an ink-jet printed co-planar waveguide transmission line on glass substrate(Azucena *et al.*, 2008). More recently, Liang *et al.* fabricated a 3D-printed microstrip line having a vertical transition using combination of ultrasonic wire embedding and fused deposition modeling techniques(Liang *et al.*, 2015). Cai *et al.* reported an aerosol-jet printed transmission line for mmWave multichip modules with embedded transmission lines and interconnects(Cai *et al.*, 2014, 2016).

In this paper, we propose a technique to connect MMICs in plastic packages using high-performance aerosol-jet printed microstrip lines. The concept is shown in Fig. 3.1, where a die is placed inside a QFN package and a microstrip line (MSL) is used to connect the package pins to the die. The thermal pad of the package acts as a ground plane for the transmission line, while the dielectric layer and signal line are printed by AJP. Thanks to the significantly improved impedance matching at high frequencies, this approach allows the use of wideband microwave signals in packaged MMICs without the bandwidth limitations of wire-bonding or the costs associated with flip-chip or COBs.

To this end, section II discusses the design of the transmission line. Section III addresses the fabrication of transmission lines on ground planes with AJP and the utilization of this technique to connect to a printed transmission line to an MMIC. In section IV the measurements are discussed, and in Section V the conclusions are presented.

3.3 Design

Traditionally, for the fabrication of transmission line on PCB, the non-conductive substrate acts as a dielectric while the top conductive layer is etched to form the microwave structures. Instead, we propose the direct-writing method to selectively deposit the dielectric, which enables applications in die-packaging.

The MSL architecture comprises of a metal signal line printed on top of a dielectric, whereas the substrate acts as the ground plane. The optimum line parameters to print a MSL with a 50 Ω characteristic impedance can be calculated using following equations for $W/H \geq 1$ (Pozar, 2004):

$$\varepsilon_{eff} = \frac{\varepsilon_r + 1}{2} + \frac{\varepsilon_r - 1}{2\sqrt{1 + 12\frac{H}{W}}} \tag{3.1}$$

$$Z_0 = \frac{120\pi}{\sqrt{\varepsilon_{eff}}\left[\frac{W}{H} + 1.393 + \frac{2}{3}ln\left(\frac{W}{H} + 1.444\right)\right]} \tag{3.2}$$

where W is the effective width of the conductive signal line and H is the effective height of the dielectric. The relative permittivity ε_r is ratio as compared to the permittivity of vacuum.

In contrast, ε_{eff} is the effective dielectric constant calculated from (3.1). $Z_0 = 50\ \Omega$ is the characteristic impedance of the test system.

Parameter	Symbol	Value
Frequency Range	f	1-18 GHz
Microstrip line length	L	2 mm
Characteristic impedance	Z_0	50 Ω
Effective dielectric height	H	30 μm
Dielectric width	D	1.0 mm
Dielectric Constant	ε_r	3.2
Dielectric loss	tan δ	0.035
Metal Conductivity	σ	$1.7 \cdot 10^7\ S \cdot \text{m}^{-1}$
Effective metal width	W	70 μm
Effective metal thickness	t	2 μm

Table 3.1 Dimension summary used for HFSS simulation of the microstrip line

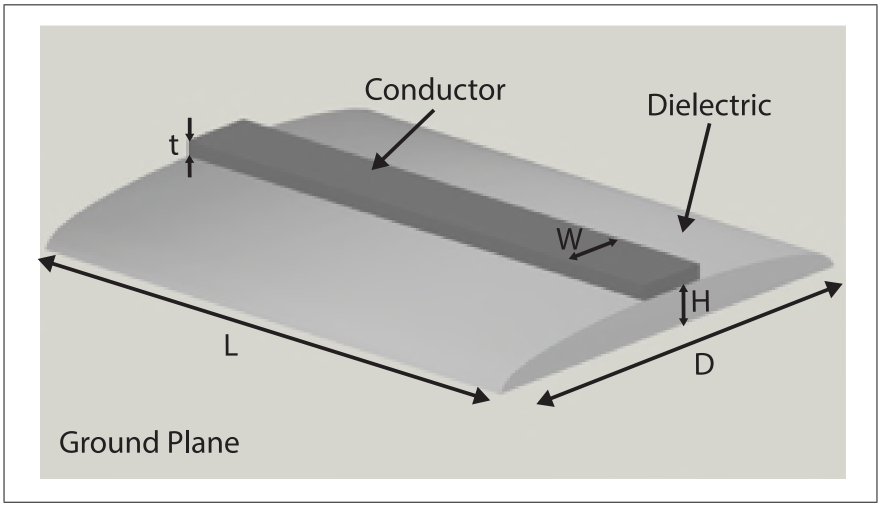

Figure 3.2 Design used for HFSS simulation of the microstrip transmission line with curved dielectric topology

We propose to use SU-8 photoresist as a dielectric because of its good printability and excellent mechanical stability after crosslinking. Its dielectric constant is reported to be 3.2 (Ghalichechian & Sertel, 2015). As a conductor we choose a silver nano-flake ink with excellent conductivity and printability.

Due to the surface tension of the dielectric ink, it forms a convex structure. Therefore, prior to the fabrication, simulations were performed using ANSYS High Frequency Structure Simulator (HFSS) in order to compare the the performance of a curved and flat dielectric topology. The parameters used for HFSS simulations are shown in Table 3.1 and the simulation model is shown in Fig. 3.2. The total length of the transmission line was set at 2 mm, which is conceptually sufficient to connect the die bondpads to the package pins of the QFN package. The curvature of the dielectric was matched to the typical wetting of SU-8 on a copper substrate.

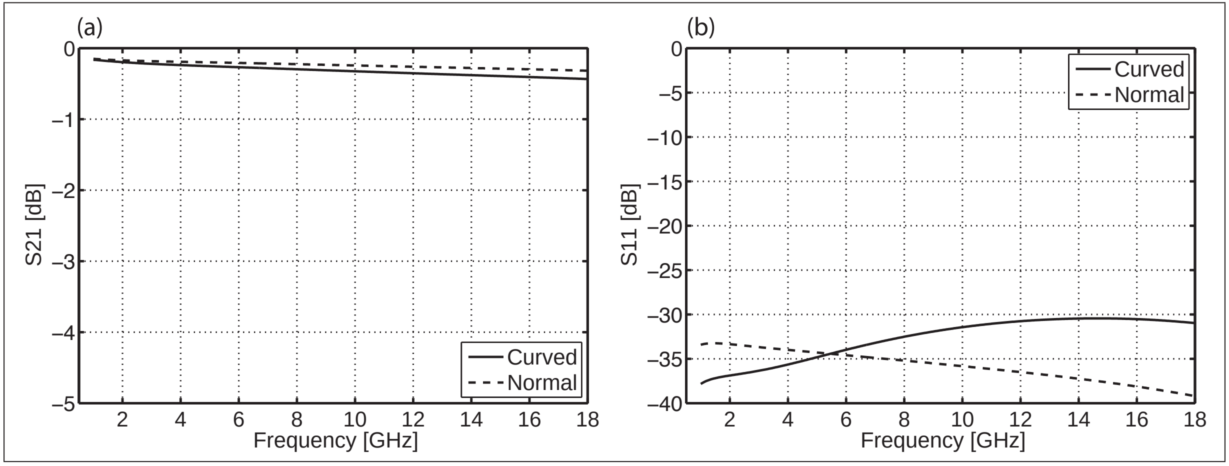

Figure 3.3 HFSS simulation of S_{21} and S_{11} for microstrip transmission line with curved and flat topology

The simulation results in Fig. 3.3 reveal that the transmission line loss and impedance match are very similar between the curved and flat dielectric.

We can therefore conclude that the classical transmission line equations are valid for use in the proposed curved dielectric.

3.4 Fabrication

3.4.1 Method and Materials

The complete fabrication is carried out under ambient environment using an aerosol-jet printing system (AJ300 from Optomec, Inc.). During the aerosol-jet printing process, a functional material solution is atomized into a mist and carried by gas stream to the substrate. A schematic representation of the printing head is shown in Fig. 3.4. The carrier gas, a stream of inert nitrogen gas, guides the dense aerosol of functional material droplets to the printing head. A virtual impactor strips away excess gas while increasing the density of the stream. At the deposition head, another flow of inert nitrogen gas, known as sheath gas, surrounds the material and focuses the printing jet stream. This sheath gas reduces the spray-over and helps prevent the clogging of nozzles, which poses a critical problem in ink-jet printing.

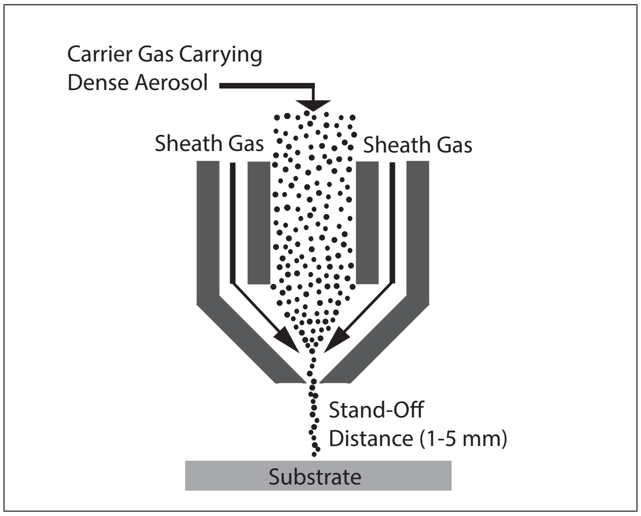

Figure 3.4 Schematic of the cross-sectional view of the aerosol-jet printing head

The atomization of material can be performed with either the ultrasonic (UA) or the pneumatic (PA) atomizer, depending on the solution properties. The UA uses an ultrasonic transducer to atomize the liquid, whereas the PA uses a high-velocity gas stream to generate the mist. The atomization process can be performed for a wide variety of materials having viscosities ranging between 1 to 1000 cP such as solutions, dispersions, suspensions and pastes containing metallic, insulating, conducting, polymer and biological materials. It can print materials with a resolution of 10 μm with an alignment precision of $\pm 2\mu$m. The width of the printed line is a primary concern in the fabrication of transmission lines. In aerosol-jet printing, it depends on ink properties, gas air flows and stage speed. It has been previously reported that the width is correlated to the focusing ratio, which is defined as(A. Mahajan & Francis, 2013):

$$\text{Focusing ratio} = \frac{\text{Sheath gas flow rate}}{\text{Carrier gas flow rate}} \tag{3.3}$$

The printing of dielectric material and conductive metal ink was carried out using ultrasonic atomizer and pneumatic atomizer, respectively. SU-8 2002, an epoxy-based UV-crosslinkable polymer, bought from Microchem Corporation was used as dielectric ink after 50% dilution with cyclopentanone. The printing was carried out by using the sheath/carrier gas flow rates of 40/20 sccm, while the substrate was maintained at 60 °C. The dielectric was thermally annealed at 150 °C for 5 min to remove excess solvent and was then cured under UV lamp for 2 min. The polymer cross-linking time may vary depending upon the dielectric thickness and UV-lamp intensity.

The signal line of the microstrip was printed using commercially available water-based silver metal ink HPS-030AE1 with 55-60% loading bought from Novacentrix without any further modification. The substrate was maintained at 60 °C to facilitate drying. The printing was carried out by fixing the sheath/virtual impactor/carrier gas flows to 50/1300/1350 sccm, thereby keeping the focusing ratio at 1. In both cases of printing materials, the stage speed was fixed at 2 mm/s. To improve the printed line resistivity, laser sintering was performed using a built-in 832 nm IR laser at a power output of 100 mW with a spot size of 30 μm. The thickness and the width of the Ag line is measured using a Dektak XT B516 profilometer. The conductivity σ of Ag was measured to be $1.7 \cdot 10^7$ S/m by four-point probe measurement using Agilent B1517A source meter and calculated as:

$$\sigma = \frac{1}{\rho} = \frac{L}{R \cdot t \cdot W} \tag{3.4}$$

where σ is the conductivity, ρ is the resistivity, R is the measured resistance, L is the length, t is the thickness and W is the width of the silver structures.

3.4.2 Printed Microstrip Line

A microstrip tline (MSL) is fabricated on a copper ground plane. At first, five layers of the SU-8 dielectric ink were printed atop the ground plane. The effective dielectric thickness was measured at 30 μm. For this dielectric height, the width of the signal line was calculated to be 70 μm for a 50 Ω characteristic impedance. Secondly, a single printing pass of silver ink is used to produce the signal line trace atop the dielectric layer. The printing parameters were adjusted to result in a 70 μm line. The optical image of the printed MSL is as show in Fig. 3.5(a).

3.4.3 MMIC Integration with Printed Transmission Line

With this newly-developed MSL printing capability, we explored its use to interface a MMIC by using an integrated transmission line. The design and measurement of this MMIC are further outlined in Appendix 3.6. To connect this MMIC chip, we can now print a 2 mm-long MSL that connects to one port of the on-die transmission line, while probing on the second port of the die. This allows us to verify the connectivity and bandwidth of the printed transmission line connection. Depending on the application, longer transmission lines can be printed without any process limitation. Here, it is envisioned to apply this technique for the packaging of silicon dice inside of standard packages.

Figure 3.5(b) shows the MMIC with the printed transmission line connection. The cross-section of the transition from the transmission line to the MMIC die is illustrated in Fig. 3.6. Typical back-ground dice have a height of 200 μm, but as our fabricated die lacks back-grinding and was 520 μm-thick, a 300 μm deep hole is carved by laser in the FR4 substrate using a ProtoMat S63 (from LPKF Laser Electronics AG) to simulate a 200 μm high die. To facilitate the transition in height between the printed transmission line and the MMIC die, SU-8 is aerosol-jet printed in the trench between the MMIC die and the PCB ground plane.

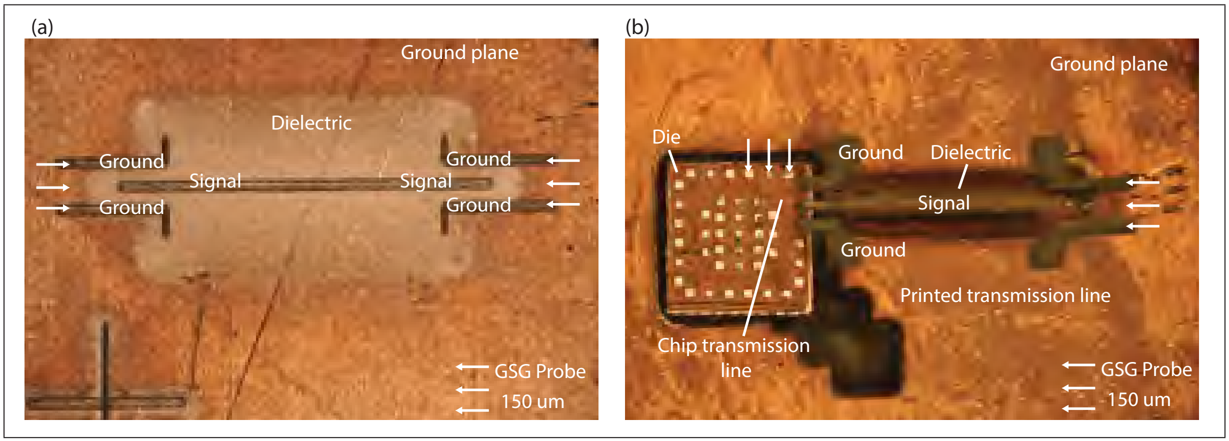

Figure 3.5 (a) Microscopic image of printed transmission line prototype on PCB showing ground plane (GND) and transmission line (TL); (b) Microscopic image of chip and printed transmission line on PCB

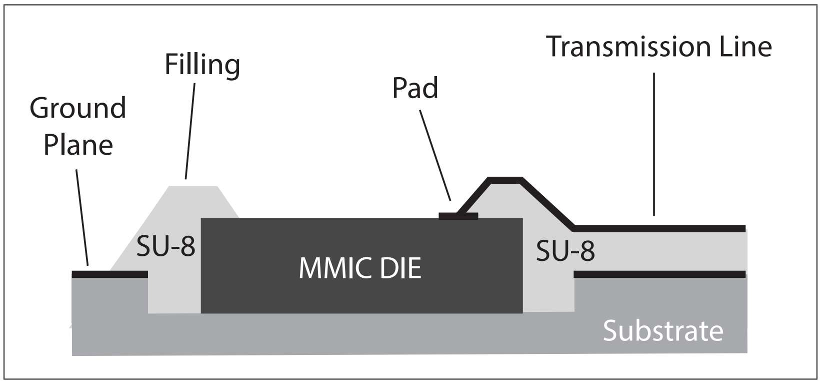

Figure 3.6 Cross-section of the transition from printed transmission line to MMIC die

For the transmission line dielectric, ten layers of the SU-8 ink were printed atop the ground plane. The effective dielectric thickness was measured at 75 μm. For this dielectric height, the effective width of signal line was calculated to be 176 μm for a 50 Ω characteristic impedance. Secondly, a single printing pass of silver ink is used to produce the signal line trace atop the dielectric layer. In order to achieve the exact signal line width, a rectangle with 175 μm width is printed using a 15 μm wide metallic trace at a pitch of 10 μm. Note that the ground pads of the on-chip transmission line must be connected to the ground plane by the shortest possible route to reduce the resistance in the ground return line. The fine 15 μm resolution of the AJP system enables connecting to bondpads with very fine pitch, even though in this work we demonstrate connectivity to bondpads with a 150 μm pitch for probing purposes.

3.5 Measurements

An N5225A PNA network analyzer from Agilent technologies (10 MHz-50 GHz) is used to perform the *S*-parameter measurements. The 150 μm pitch, I40A GSG high frequency probes are used to perform measurements using SMA cables (measures up to 18 GHz). The measured frequency range was set from 500 MHz to 18 GHz. The SOLT calibration is carried out using the Picoprobe CS-5 calibration substrate.

The *S*-parameter measurements for the printed transmission line in Fig. 3.5(a) are shown in Fig. 3.7(a)-(b). Figure 3.7(a) shows a transmission loss of 0.8 dB at 500 MHz and 0.6 dB at 18 GHz. We attribute the increased loss below 2 GHz to capacitive coupling of the probe tips to the transmission line, which is due to the height differences of the signal and ground conductors. The design of the transmission line was altered for the MMIC integration setup to ensure better probe connectivity. Figure 3.7(b) shows that the measured S_{11} parameter decreases from -20 dB at 500 MHz to around -40 dB at 18 GHz. This suggests that the printed MSL has a good impedance match with the 50 Ω circuit impedance with a low loss over a large operation bandwidth.

For the second setup in Fig. 3.5(b), the integrated on-chip transmission line was de-embedded from the characterization to yield the *S*-parameters of the isolated printed transmission line and wire-bonds (further details are included in Appendix). The measured *S*-parameters of the printed MSL are shown in Fig. 3.7(c)-(d). S_{21} measurements in Fig. 3.7(c) show a transmission loss increasing from 0.7 dB at 500 MHz to 1.8 dB at 18 GHz for the printed transmission line.

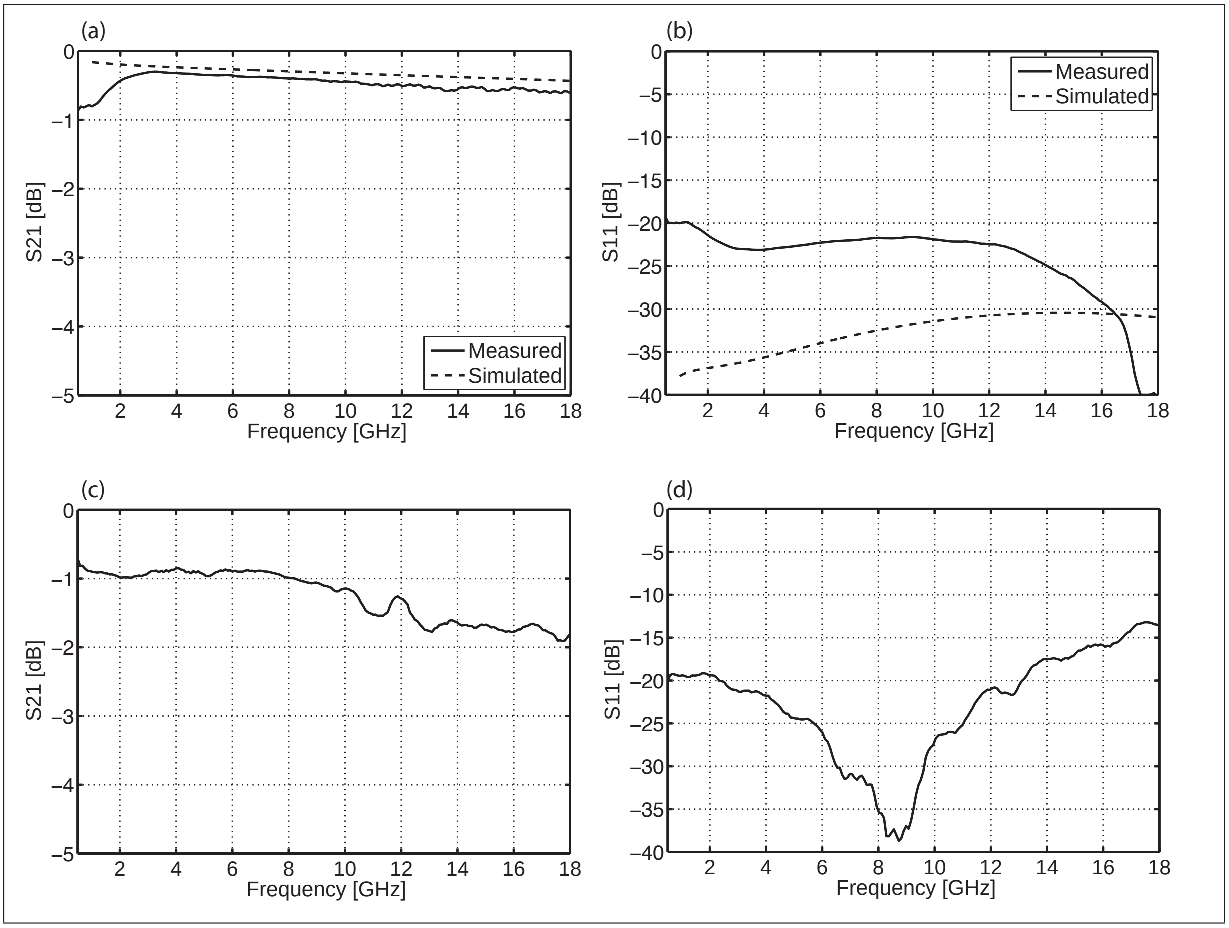

Figure 3.7 (a) Simulated and measured (a) S_{21} and (b) S_{11} parameter of 2 mm long printed transmission line prototype on PCB; Measured (c) S_{21} and (d) S_{11} parameter for chip connected by printed transmission line

In Fig. 3.7(d), the S_{11} parameter for the printed MSL shows a good impedance match with the 50 Ω line of the MMIC chip, with -20.1 dB at 500 MHz and -13.6 dB at 18 GHz.

From these measurements we can conclude that the printed transmission line has low loss and good impedance matching over a wide bandwidth up to 18 GHz. Therefore, the proposed technique enables the packaging of high performance microwave MMICs into plastic packages using low-cost printing techniques. It is expected that further optimization of this technique can enable applications in even higher frequency bands above 18 GHz, where bondwire inductance becomes an even larger problem.

Paper	Topology	Conductor	Dielectric	Max Frequency [GHz]	Loss @ Max Freq. [dB/mm]	Includes TL-to-die transition
This Work	Microstrip	Ag	SU-8 (printed)	18	0.90 0.30	Yes No
(Azucena *et al.*, 2008)	CPW	Ag	Glass	20	0.26	No
(Cai *et al.*, 2014)	CPW	Ag	LCP substrate	170	0.51	No
(Cai *et al.*, 2016)	Stripline	Ag	Polyimide (printed)	40	0.53	No

Table 3.2 Comparison of published printed transmission lines

Table 3.2 compares this work with published printed transmission lines. The loss of the transmission lines is normalized to their length and compared at the maximum measured frequency. The measured 0.6 dB of insertion loss for the 2 mm long stand alone transmission line at 18 GHz results in a loss of 0.3 dB/mm, while the 1.8 dB loss for the transmission line connected to the MMIC results in 0.9 dB/mm at 18 GHz. When compared to coplanar waveguides (CPW) with printed conductors on existing substrates (Azucena *et al.*, 2008; Cai *et al.*, 2014) and a stripline with printed conductor and dielectric (Cai *et al.*, 2016), our stand-alone microstrip line achieves a comparable loss of 0.3 dB/mm. For the first time, we are able to report the loss of a printed transmission line to a MMIC die. The TL-to-chip transition introduces extra losses, which results in the reported 0.9 dB/mm loss. We expect that further optimizations can bring the loss of the TL-to-die closer to the loss of the isolated transmission line.

3.6 Conclusion

We demonstrate the use of aerosol-jet printing, in order to fabricate a fully-printed transmission line for chip-on-board applications. We also demonstrate its potential as an alternative to conventional wire-bonding, particularly for high-performance MMICs applications. SU-8 was proposed as a printed dielectric, due to its good printability and mechanical properties, while the conductor was printed from a nano-flake silver ink. First, the microstrip line prototype was optimized to achieve a 50 Ω characteristic impedance and printed on a PCB. The transmission loss of this printed transmission line is 0.3 dB/mm at 18 GHz with good impedance matching. Then, the transition of the printed transmission line to a MMIC chip was demonstrated. The loss measurement including the TL-to-die transition at 18 GHz shows 0.9 dB/mm, with the S_{11}

measurement at 18 GHz of -13.6 dB. As such, we believe this additive printing approach to on-chip interconnections has the potential to transform MMICs packaging for high-speed RF applications.

Acknowledgements

The authors would like to thank NanoQAM, NSERC, ReSMiQ and CMC Microsystems for financial support. SGC is also thankful to the Canada Research Chairs program for its support. The authors thank Mr. Normand Gravel for his continuous assistance with equipment support and Dr. Mohammad Rahmani for his support and fruitful advice throughout the project.

Demonstration MMIC Die

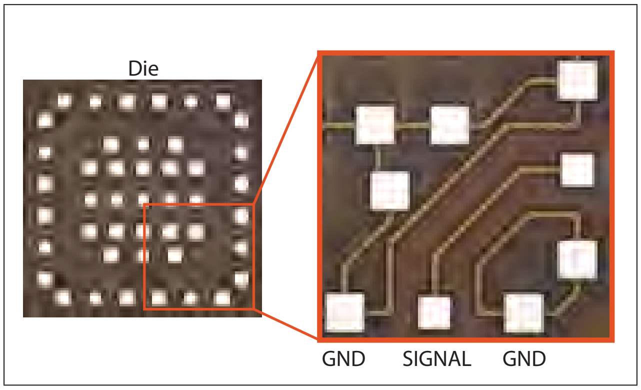

Figure 3.8 Microscopic image of chip (left) and magnified view of integrated on-chip transmission line (right)

This appendix outlines the design and measurement of a MMIC with integrated transmission line, as a demonstration MMIC for printed transmission line connections.

The MMIC is designed and fabricated in an AMS 0.35 μm CMOS process. Figure 3.8 shows the optical image of the overall chip (measuring 1150 μm by 1150 μm), while the inset shows a magnified view of one of the built-in on-chip transmission lines. This transmission line connects a probe-compatible G-S-G pads on the lower chip edge to G-S-G pads on the right chip edge over a distance of 400 μm.

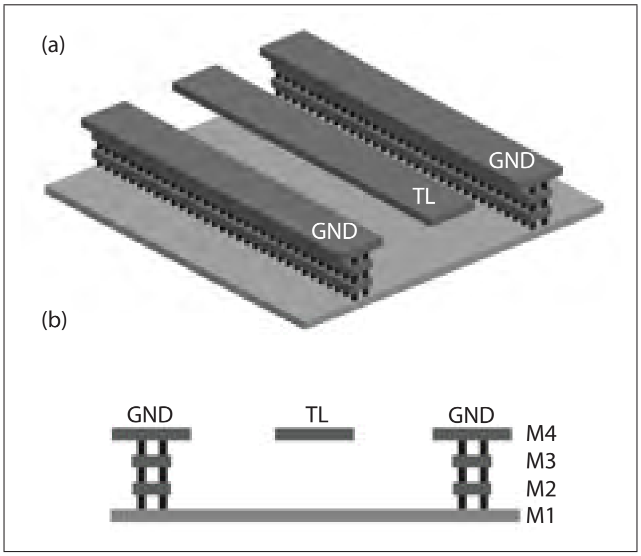

Figure 3.9 (a) Transmission line on CMOS die showing ground plane (GND) and transmission line (TL). (b) Cross-sectional view

A cross-section of the integrated transmission line is shown in Fig. 3.9. The microstrip ground plane is in metal-1, while the signal line is in metal-4 with a width of 10 μm. The dielectric distance between metal-1 and metal-4 is 4.3 μm, leading to a simulated characteristic impedance of 50 Ω.

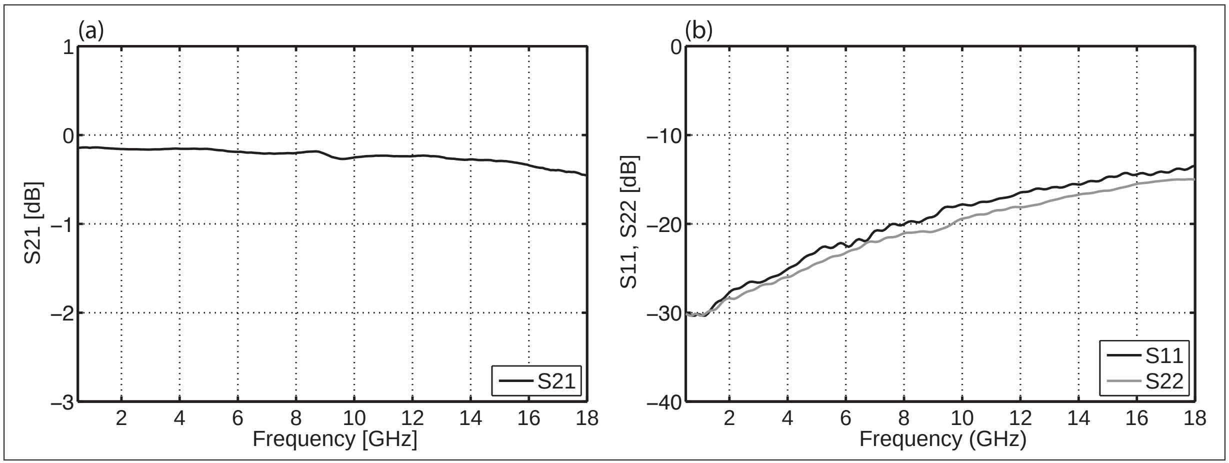

Figure 3.10 (a) Measured S21 for on-chip transmission line. (b) Measured S11 and S22 for on-chip transmission line.

The on-chip transmission line was characterized with a vector network analyzer from 1 to 18 GHz. Figure 3.10 (a) shows the transmission loss for on-chip microstrip line to be less than 0.5 dB over the frequency range. Figure 3.10 (b) shows the measured S_{11} and S_{22} for on-chip microstrip line to be below -13 dB over the frequency range, indicating that good matching to 50 Ω is achieved.

In the measurements of a printed transmission line connected to the MMIC, the loss of the on-chip transmission line was subtracted from the measurements results to yield the loss of the de-embedded printed transmission line.

Comparison with Wirebonded Die

This appendix demonstrates a comparison between the MMIC with printed transmission line and wirebonding. The MMIC was wirebonded in a plastic QFN package with 1.0 mil gold wires. The length of both the printed transmission line and the wire-bonding are identical at 2 mm.

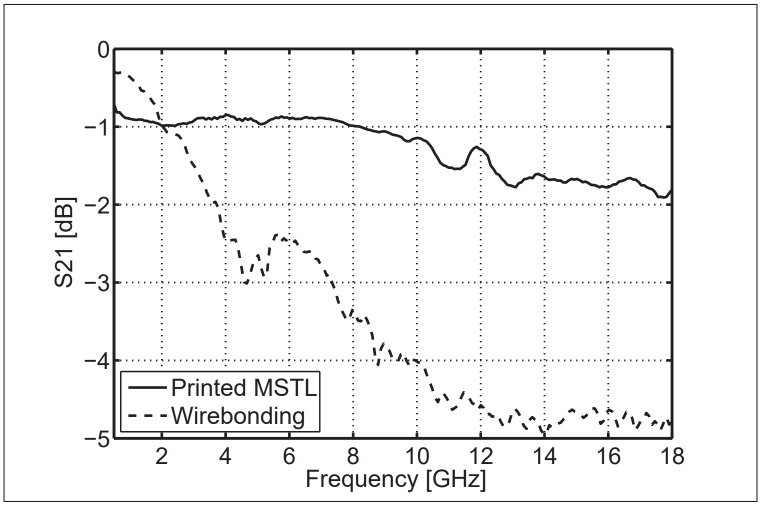

Figure 3.11 Measured S_{21} parameter for printed transmission line and measured S_{21} parameter for wire-bonding

The measured S-parameters of both the printed MSTL and the wire-bonded connections are compared in Figure 3.11 and Figure 3.12. S_{21} measurements in Figure 3.11 show a transmission loss increasing from 0.7 dB at 500 MHz to 1.8 dB at 18 GHz for the printed transmission line, compared to a transmission loss increasing from 0.3 dB to over 4.8 dB for the wire-bonded connection at the same frequencies. In Figure 3.12, the S_{11} parameter for the printed MSTL clearly shows much better impedance matching with the 50 Ω line of the MMIC chip, with -20.1 dB at 500 MHz and -13.6 dB at 18 GHz compared to -18.61 dB at 500 MHz and -4.7 dB at 18 GHz for the wire-bonded connection.

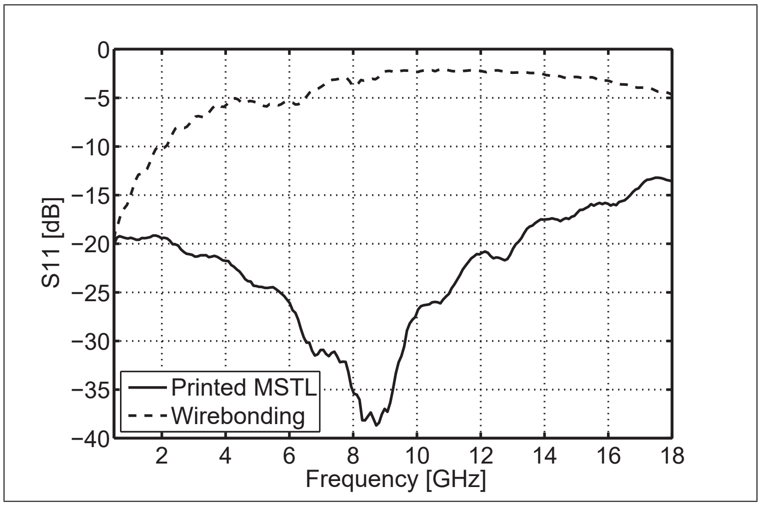

Figure 3.12 Measured S_{11} parameter for printed transmission line and measured S_{11} parameter for wire-bonding

From these measurements we can conclude that the printed transmission line has much lower losses and much better impedance matching over a wide bandwidth, especially for high-frequency operation. This can be largely explained by the impedance mismatch suffered by the wire bonded sample due to the bond-wire's inductance. Therefore, the proposed technique enables the packaging of high performance microwave MMICs into plastic packages using low-cost printing techniques.

PREFACE: CHAPTER 4

In the previous chapter, a fully printed transmission line for high frequency packaging applications was presented. The next chapter continues on this line of research by extending the transmission line into a microwave ring resonator. Microwave ring resonators are versatile structures that find applications in sensors, filters and diplexers. These rings have been predominately fabricated on high quality Printed Circuit Boards (PCB), which result in a large size footprint and low resonant frequency. Their integration with integrated circuits can be difficult due to the transition from transmission line to semiconductor package. In this work, it is proposed to print the ring resonator inside of the semiconductor package together with the semiconductor die. This leads to high resonant frequencies, direct integration with integrated circuits and a very small footprint. As a digital-write printing technique, AJP is ideally suited to selectively deposit the dielectric where it is needed. AJP's high weight % loading inks allow the deposition of a thick conductor on top of the dielectric in a single pass without overflow. Firstly, this is crucial in obtaining a low conductor resistance and therefore high Quality factor (Q). Secondly, this allows accurate control of the coupling gap spacing that is required for optimal ring coupling. It is foreseen that more microwave structures can be printed with AJP, especially at higher millimeter wave frequencies.

CHAPTER 4

AEROSOL JET PRINTED, MICROWAVE MICROSTRIP RING RESONATORS FOR SENSING APPLICATIONS

Anubha Gupta[1], Mohammad H. Rahmani[1], Michiel C.M. Soer[1], Sylvain G. Cloutier[1],
Ricardo Izquierdo[1]

[1] Electrical Engineering Department, École de Technologie Supérieure,
1100 Notre-Dame Ouest, Montréal, Québec, Canada H3C 1K3

Article submitted for review to IEEE Transactions on Components, Packaging and Manufacturing Technology in May 2019.

4.1 Abstract

This paper presents the design, simulation and fabrication of fully printed microstrip transmission line and microwave ring resonators using aerosol-jet printing for system-in-package applications. The printed transmission lines are 8 mm long and their S-parameters are measured over a wide bandwidth ranging from 1 GHz to 26 GHz. Their insertion loss ranges between 0.02 dB/mm at 1 GHz and 0.56 dB/mm at 26 GHz. Ring resonators were designed and printed to operate at center frequencies of 15.5 GHz, 17.5 GHz, 19.5 GHz and 21.5 GHz by tuning the size of the ring. Variability studies are carried out to evaluate the ability of the printing process to fabricate reproducible devices. The coupling gap is optimized in order to minimize the insertion loss in the ring resonators. The simulations are consistent with the experimental results. The ability to print both conductors as well as dielectrics for the fabrication of microwave resonators demonstrate the potential for in-package integration of RF resonators for low-cost sensor applications.

4.2 Introduction

Microwave ring resonators are versatile components that have found applications in diverse fields, such as moisture, gas and biological sensing (Velez *et al.*, 2017; Herrojo *et al.*, 2017;

Bahar *et al.*, 2017a; Samant *et al.*, 2015; Kim *et al.*, 2014; Torun *et al.*, 2014; Sharafadinzadeh *et al.*, 2017; Jing *et al.*, 2017; Babarinde *et al.*, 2018; Xu *et al.*, 2018; Mahdi *et al.*, 2016; Bahar *et al.*, 2017b; Zarifi *et al.*, 2018; Zarifi & Daneshmand, 2015). Torun *et al.* fabricated a split ring resonator (SRR) for biomolecular sensing at frequency 2.12 GHz (Torun *et al.*, 2014). Kim *et al.* demonstrated a double-SRR for gas sensing applications at 13 GHz (Kim *et al.*, 2014). Sharafadinzadeh *et al.* showed an application of microwave SRR in glucose sensing at 1.863 GHz (Sharafadinzadeh *et al.*, 2017). Bahar *et al.* used microfluidic planar resonators to detect the permittivity of liquids at 2.35 GHz for pharmaceutical and biomedical applications (Bahar *et al.*, 2017a). These sensing applications rely on measuring the shift in resonance frequency of the resonator. Another field of application for ring resonators is in microwave filters and diplexers (Shaman *et al.*, 2014; Matsuo *et al.*, 2001; Luo & Zhu, 2009; Ma *et al.*, 2007). A 14.5 GHz and 28.2 GHz diplexer was reported for next generation 5G wireless networks (Shaman *et al.*, 2014). Matsuo *et al.* demonstrated a 1.9 GHz dual-mode ring resonator for bandpass applications (Matsuo *et al.*, 2001). A dual-band ring resonator filter was proposed for the 2.4 and 5.8 GHz band in wireless applications (Luo & Zhu, 2009). In filter applications, the ring resonator architecture is optimized for minimal insertion loss and maximum out-of-band rejection.

In general, these ring resonators have been fabricated on high-frequency Printed Circuit Boards (PCB) with tightly controlled dielectric and conduction properties. This reduces the conduction and dielectric losses, but results in a large PCB footprint, which makes it difficult to integrate with Monolithic Microwave Integrated Circuits (MMICs). Efforts have been made to print the conducting elements of microwave structures using additive technologies, which promises low-cost manufacturing, rapid turnover time and large-area fabrication. Direct-writing additive technologies, such as inkjet printing and aerosol jet printing are most promising, due to their ability to print a wide varieties of materials, while allowing rapid prototyping and reduced material waste. These technologies have been used in a wide range of RF and microwave applications, including transmission lines (Azucena *et al.*, 2008; Liang *et al.*, 2015; Cai *et al.*, 2014, 2016), antennas (Cook *et al.*, 2013; Mariotti *et al.*, 2015; Rida *et al.*, 2010; Marroncelli *et al.*, 2011; Siden *et al.*, 2007) and filters (Olukoya & Budimir, 2016; Sette *et al.*, 2013; Ahmad *et al.*, 2015). Inkjet printing has been most commonly used for the fabrication of printed microwave filters. Olukoya *et al.* reported an inkjet printed microstrip bandstop filter at 2.4 GHz (Olukoya & Budimir, 2016). Ahmad *et al.* reported a bandpass coplanar waveguide filter designed at 5.8 GHz (Ahmad *et al.*, 2015). Sette *et al.* reported a filter at 17 GHz fabricated using inkjet printing (Sette *et al.*, 2013). Since the printed microwave conductor structures are deposited on top of existing substrates, they still suffer from the same size and integration drawbacks as traditional PCBs.

In this work, we propose the concept of a fully-printed microwave resonator co-integrated with a MMIC inside a standard package. The concept is shown in Fig. 4.1. The thermal pad of the package serves as the ground plane of the resonator, while the dielectric as well as the top conductor are additively-printed into the package. The advantages of this concept include a small physical footprint, due to a high resonant center frequency, and low interface losses to the MMIC.

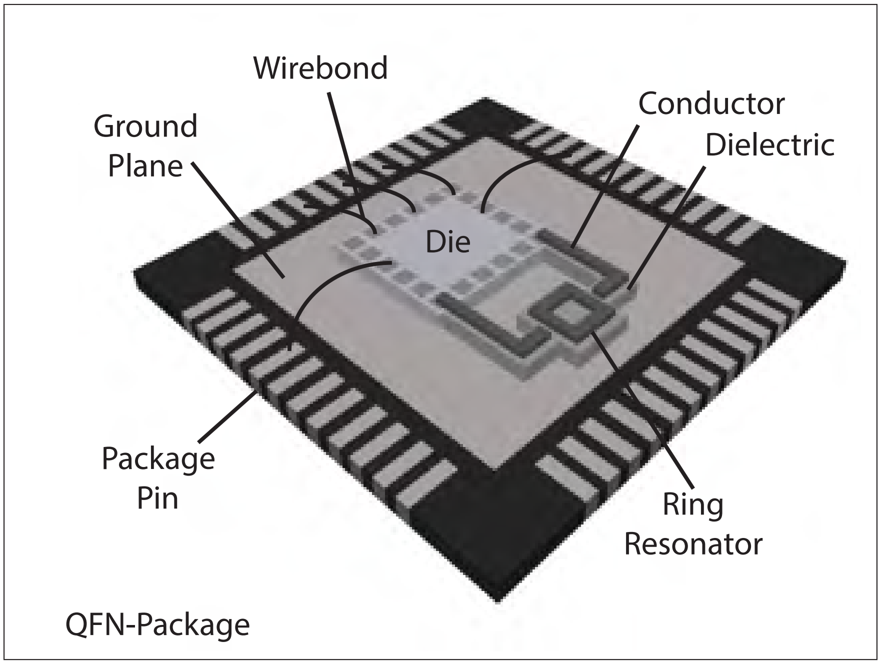

Figure 4.1 Concept drawing of in-package ring resonator with fully printed dielectric and conductor for sensing applications

The rest of the paper is organized as follows. Section 4.3 provides the details about the materials that are used for the fabrication of these high-frequency resonators. Section 4.4 describes the equations used to design and model these structures using High Frequency Structure Simulator (HFSS) simulation software. Section 4.5 outlines the details about the fabrication procedure for these devices by aerosol jet printing technique. Finally, section 4.6 presents the measurement results and the main conclusions are highlighted in section 4.7.

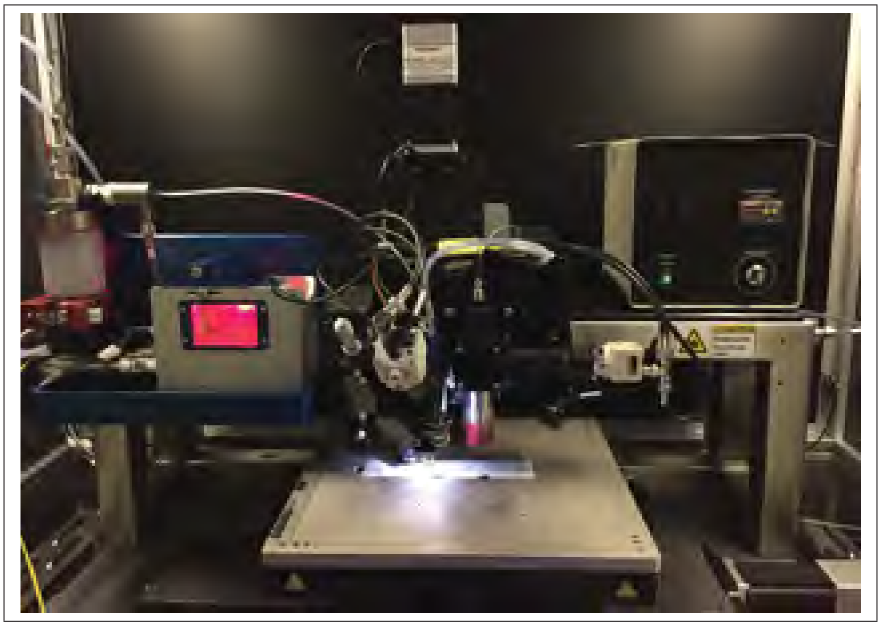

Figure 4.2 Aerosol jet printing system, with pneumatic and ultrasonic atomizer

4.3 Aerosol Jet Printing of Dielectric and Metallic inks

Aerosol jet printing is capable of depositing a wide range of functional materials, including metals, dielectrics and semiconductors, from solutions with viscosities ranging from 1 to 1000 cP. In comparison to inkjet printing, aerosol jet is capable of processing ink formulations with much higher weight % loadings, and can thus achieve thicker films in a single pass. This can contribute to a lower resistance for printed conducting traces. Furthermore, the system's built-in infrared laser enables sintering of deposited materials without damaging its surroundings. The dielectric ink is printed using an ultrasonic atomizer and metal ink is printed using a pneumatic atomizer. The details of the aerosol-jet operation mechanism are found in our previous work (Gupta *et al.*, 2016).

An epoxy based dielectric ink, cross-linkable by ultraviolet exposure (SU8-2002 bought from Microchem Corporation) is printed as an insulating layer between the ground and signal line. Before printing, the epoxy is diluted by 50% using cyclopentanone. The viscosity of the ink formulation is measured to be 2.5 cP. The printing is carried out on top of a PCB, while maintaining the substrate temperature at 60°C. The dielectric film is then post-annealed at 150°C for 5 min to remove extra solvent. It is then UV-cured for an additional 5 min to allow cross-linking of the polymer.

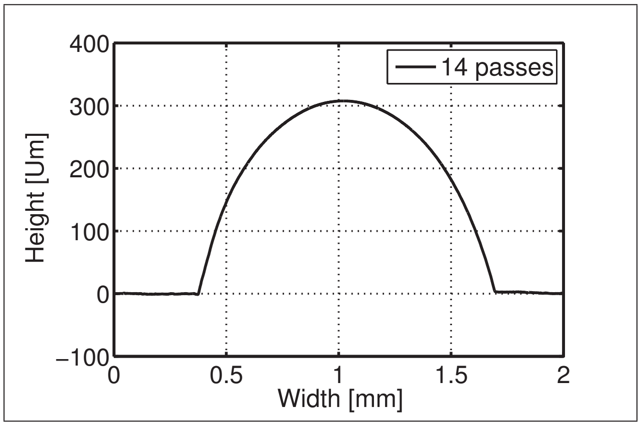

Figure 4.3 Thickness profilometer scan of printed dielectric SU8 film after curing

The profilometer scan of the dielectric film, as measured with a Dektak XT B516 profilometer, is shown in Fig 4.3. A 300 μm-thick convex structure is obtained by successively printing 14 passes of SU-8 in a single session. The curvature of the dielectric film is due the surface tension of the liquid. The film has an effective thickness of 250 μm over the total width of 1.3 mm. The relative permittivity, ε_r of the hardened SU-8 is 3.2 at 1 GHz and the dielectric loss, tan δ, is 0.035 (Ghannam *et al.*, 2009). The cured dielectric film is mechanically stable and remains unaffected by the subsequent printing of silver ink on top of it.

A commercial water-based silver nano-flake ink, HPS-030AE1 with 55 weight % loading from Novacentrix is used without further modification. These Ag lines are printed on a glass substrate while its temperature is maintained at 60°C, to prevent the ink from overflowing. After being printed, these structures are laser sintered at a power output of 100 mW with a spot size of 30 μm. The conductivity σ of Ag was measured by a four-point probe measurement using an Agilent B1517A source meter and calculated using equation 4.1.

$$\sigma = \frac{1}{\rho} = \frac{L}{R.t.w} \tag{4.1}$$

where ρ is the resistivity, R is the measured resistance, L is the length, t is the thickness and w is the width of the silver line.

The measured thickness for an increasing number of passes and their measured conductivity is shown in Table 4.1. The measured conductivity of the printed silver ($1.69 \cdot 10^7$ S/m) is 27% of the published conductivity of bulk silver ($6.30 \cdot 10^7$ S/m).

Number of passes	**Thickness (μm)**	**Conductivity (S/m)**
1	5	$1.69\dot{1}0^7$
2	12	$1.69{\cdot}10^7$
3	20	$1.78{\cdot}10^7$
4	25	$1.78{\cdot}10^7$

Table 4.1 Conductivity of Silver calculated for multiple printing passes

4.4 Resonator Design and Simulation

A microwave ring resonator is basically a transmission line looped on itself (Fig. 4.4). Constructive interference occurs when an integral multiple of the microwave wavelength fits into the circumference of the ring.

The basic building block of the ring is formed by microstrip (MS) transmission lines, which comprises of a signal conductor separated from the ground plane by a dielectric. These transmission lines are designed with a characteristic impedance Z_0 of 50 Ω, to ensure that energy can be efficiently coupled into the ring. The impedance of the line can be calculated from the line parameters with the following equations (Pozar, 2004):

$$\varepsilon_{eff} = \frac{\varepsilon_r + 1}{2} + \frac{\varepsilon_r - 1}{2\sqrt{1 + 12\frac{H}{w}}} \tag{4.2}$$

$$Z_0 = \frac{120\pi}{\sqrt{\varepsilon_{eff}}\left[\frac{w}{H} + 1.393 + \frac{2}{3}ln\left(\frac{w}{H} + 1.444\right)\right]} \tag{4.3}$$

where, ε_r is the dielectric constant, H is effective height of the dielectric and w is the effective width of the metal signal line. ε_{eff} is the effective dielectric constant calculated from equation 4.2. For the printed dielectric thickness of 250 μm, the width of the signal line is calculated to be 600 μm in order to achieve a 50 Ω characteristic impedance.

According to the simple model, the circumference of the ring resonator is designed to fit integral multiples of the guided wavelength. For a specific center-frequency, the guided wavelength λ_g is calculated as:

$$\lambda_g = \frac{c}{f \cdot \sqrt{\varepsilon_r}} \tag{4.4}$$

$$2L_R + 2W_R = n\lambda_g \qquad \text{for n = 1,2,3...} \tag{4.5}$$

where c represents the speed of light, ε_r is the dielectric constant and f is the frequency corresponding to the guided wavelength (Chang & Hsieh, 2004). L_R and W_R are the length and width of the ring resonator, and n is the mode number. For example, at a center-frequency of 15.5 GHz, the corresponding guided wavelength is calculated to be 10.82 mm. Energy is coupled capacitively into the ring from the feedlines through the coupling gaps. The spacing of the coupling gaps presents a trade-off between Q factor and insertion loss.

Parameter	**Symbol**	**Value**
Effective ring length	L_R	5800 μm
Effective ring width	W_R	2750 μm
Effective metal width	w	600 μm
Effective metal thickness	t	5 μm
Metal Conductivity	σ	$1.7 \cdot 10^7$ S/m
Effective dielectric height	H	250 μm
Dielectric Constant	ε_r	3.2
Dielectric loss	tan δ	0.035
Coupling gap	G	100 μm
Resonant frequency	f_r	15.5 GHz
Characteristic impedance	Z_0	50 Ω

Table 4.2 Summary of dimensions used for HFSS simulation of microwave ring resonator with center-frequency at 15.5 GHz

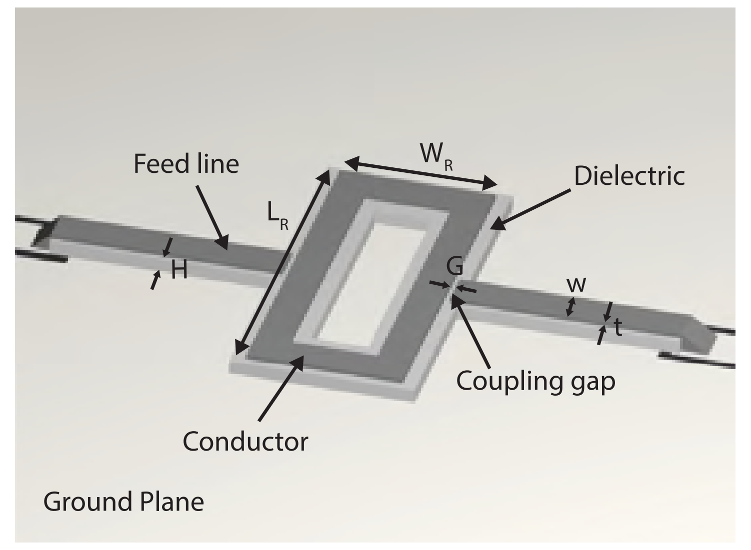

Figure 4.4 Design used for HFSS simulation of microwave ring resonator with center-frequency at 15.5 GHz

Simulations are performed using ANSYS HFSS and the design of the ring resonator is modified based on these results. For the printed silver layer, the metal conductivity is taken to be $1.7 \cdot 10^7$ S/m, as measured previously. A ring resonator having a center frequency of 15.5 GHz is designed with the parameters summarized in Table 4.2. Note that the HFSS simulated parameters are different from the parameters calculated using the simple model.

4.5 Fabrication

The fully additive fabrication process was carried out with an aerosol jet printing system (AJ-300), from Optomec. The layers are printed on RT/duroid 5880, high frequency laminates from Rogers Corporation with an 18 μm-thick copper top-layer. The copper layer forms the ground plane for the microwave devices.

The first step is to print the dielectric in order to isolate the ground plane from the signal line. It is printed using a 300 μm deposition nozzle at a speed of 5 mm/s. The ultrasonication can heat up the ink formulation, raising the vapor pressure and thus affecting the printing process. To prevent this, the water bath is controlled at 25 °C. The 1 ml of dielectric ink is atomized at a power of 50 W. Once the material mists and the container is saturated, an inert carrier gas (N_2) is used to carry the functional material from the atomizer to the printing head, and the carrier gas flow rate is set at 30 sccm. The sheath gas which helps in focusing of the printing jet stream by surrounding the carrier gas is set at 60 sccm. The dielectric layer is printed using lines having a width of 150 μm are printed at a pitch of 100 μm. The surface tension of the SU-8 creates a smooth topology. After printing, the substrate is dried at 150 °C for 5 min, followed by UV curing for 5 min.

Next, the silver ink is printed on top of the cured dielectric using a 150 μm deposition nozzle at a speed of 3 mm/s. The tube temperature maintained at 42 °C. This promotes faster drying and prevents the ink from overflowing. The carrier and virtual impactor gas flow rates are set at 1150 and 1100 sccm, respectively. The virtual impactor removes the extra solvent and increases the density of the deposited material. The sheath gas flow rate is set at 50 sccm. The 600 μm wide signal line is deposited by printing lines having a width of 15 μm at a pitch of 10 μm. The conductor is then laser sintered at a power of 100 mW.

A microscope image of the fabricated ring resonator is shown in Fig. 4.5. The coupling gaps are well defined and conform to the CAD design. Figure 4.6 shows microscope images of ring resonators fabricated with different resonant frequencies and coupling gaps.

Figure 4.5 Microscope image of an AJ-printed ring resonator

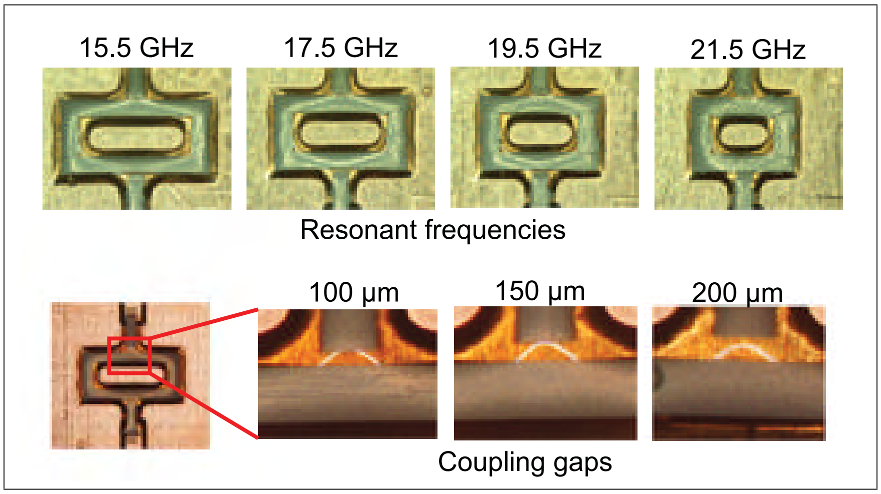

Figure 4.6 Microscope images of fabricated resonator rings with different resonant frequencies and coupling gaps.

4.6 Measurements

The measurements are carried out using a N5247A PNA-X Vector Network Analyzer (VNA) from Agilent technologies. The VNA is connected using 2.4 mm high frequency connecting cables characterized to measure up to 40 GHz. The SubMiniature version A (SMA) connectors support a maximum frequency up to 26.5 GHz. The setup was calibrated by the standard Short

Open Load Through (SOLT) calibration method. The S-parameters measured for the printed transmission line and microwave ring resonators are presented in this section.

Fig. 4.8 (a) shows the S_{21} parameter measured for a 8 mm long printed microstrip transmission line, characterized from 1 to 26 GHz. The insertion loss ranges from 0.02 dB/mm at 1 GHz up to 0.56 dB/mm at 26 GHz.

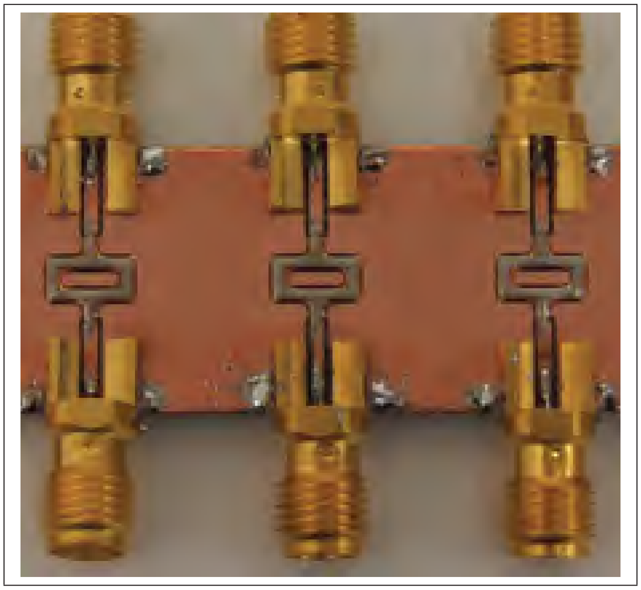

Figure 4.7 Setup for measuring the ring resonators, including SMA connectors which are soldered onto the substrate for S-parameter measurements

The coupling gap influences the performance of the ring. When the gap is large (loose coupling), it may give a higher Quality (Q) factor, but also a larger insertion loss. If the gap is reduced (tight coupling), the insertion loss is lowered, but the Q factor degrades and may cause resonant-peak shift due to capacitive loading. As such, achieving the optimal coupling gap is crucial to trade-off between high Q factor values and low insertion losses.

Resonators with 200 μm, 150 μm and 100 μm coupling gaps were fabricated. The measured transmission characteristics for these microwave ring resonators are shown in Fig. 4.8 (b). The 200 μm coupling gap results in much higher insertion losses compared to 150 μm or 100 μm gaps. In the transition from 150 μm to 100 μm coupling gaps, the S_{21} measurements show that its influence on insertion loss is much reduced. This suggests that the ring is approaching optimal coupling. Thus, all further devices are fabricated having the optimal coupling gap of 100 μm.

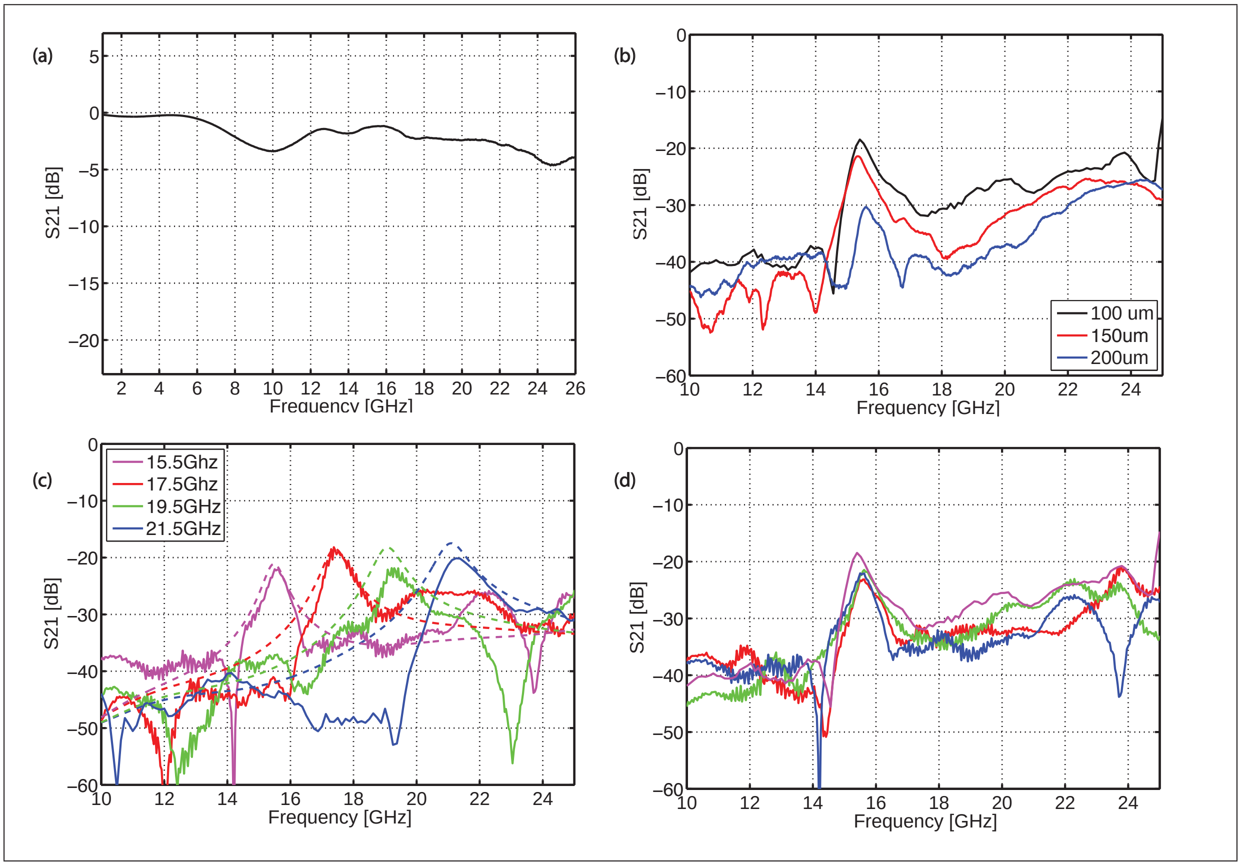

Figure 4.8 (a) Measured S_{21} parameter for aerosol jet printed microstrip transmission line with length of 8 mm. (b) S_{21} measurements showing influence of coupling gap variation for ring resonators having center-frequency at 15.5 GHz. (c) HFSS simulations and S_{21} measurements for ring resonators designed to have center-frequency at 15.5, 17,5, 19.5 and 20.5 GHz. (d) Variation study showing S_{21} parameters for four ring resonators designed to have center-frequency at 15.5 GHz showing reproducibility of printing process.

Next, resonators with center-frequency at 15.5, 17.5, 19.5 and 21.5 GHz were fabricated. The simulated and measured transmission characteristics for these microwave ring resonators are shown in Fig. 4.8 (c). The dotted line represents the simulated results whereas the solid line represents the measured results. Overall, S-parameters measurements of these printed structures show good agreement with the simulated transmission response. The Q factors for the resonators with center-frequencies at 15.5, 17.5, 19.5 and 21.5 GHz are 27, 28, 26 and 20, respectively. For resonators with center-frequency at 17.5 and 21.5 GHz, measured results show higher insertion losses as compared to the simulated results. This can be attributed to increased dielectric loss at higher frequencies.

In order to ascertain the reliability of the printing process and reproducibility of ring resonator performances, a variation study is carried out. Four identical devices with a 15.5 GHz center-frequency and 100 μm coupling gap were fabricated. Figure 4.8 (d) shows the S-parameters characteristics for these devices. All the devices show an insertion loss below 20 dB and consistency in terms of center-frequency and Q factor. The Q factor for all four resonators is measured to be between 25 to 30.

Parameter	**Value**
Fabrication method	Aerosol jet printing
Line conductor	Ag 5 μm thick
Dielectric	SU-8 250 μm thick
Ground plane	Cu 18 μm thick
Resonator frequency	15.5 to 21.5 GHz
Insertion loss	-18 to -23 dB
Quality factor	20 to 28

Table 4.3 Summary of fabricated ring resonators

This study demonstrates that the aerosol jet printing technique can yield microwave resonators for system-in-package applications. These fully additive ring resonators avoid the cost of micro-machining, photo lithography and vacuum processing. These are low-cost devices, completely processed at temperatures < 150 °C. In our future work, these resonators will be integrated with an MMIC inside a package.

4.7 Conclusion

To summarize, a microstrip transmission line and microwave ring resonators have been fabricated by aerosol jet printing technology on high-frequency compatible PCB. These microwave structures are characterized from 1 to 26 GHz. The 8 mm long transmission line shows a minimum insertion loss of 0.02 dB/mm at 1 GHz and a maximum insertion loss of 0.56 dB/mm at 26 GHz. The ring resonator was designed and modeled using the ANSYS HFSS simulator prior to fabrication. The influence of the coupling gap on the insertion loss in the ring resonator was demonstrated and an optimal coupling gap was determined from measurements. Ring resonators centered at 15.5, 17.5, 19.5 and 21.5 GHz were fabricated, with a coupling gap of 100 μm. The simulated and experimental results show good agreement in terms of insertion loss, center-frequency and Q factor. All the printed ring resonators demonstrate insertion loss below 20 dB. A variability study shows the reliability of the printing process to produce reproducible devices. This work demonstrates the potential of low-cost aerosol jet technologies for microwave ring resonators. Future work aims at in-package integration of fully printed microwave ring resonator with a MMIC. This would enable sensing applications at much smaller form factor and significant reduction of cost.

4.8 Acknowledgment

The authors would like to thank NanoQAM, NSERC, LACIME and ReSMiQ for financial support. SGC is also thankful to the Canada Research Chair Program for its support. The authors thank Mr. Normand Gravel for his continuous lab assistance.

CHAPTER 5

CONCLUSIONS

5.1 Summary

In the introduction, an overview of printed electronics and their benefits in comparison to conventional electronics were given. The capabilities of different printing technologies were highlighted, along with the intrinsic differences between them. Furthermore, the background of printed devices in the field of photodetectors, packaging, microwave transmission lines and resonators has been sketched. The operating principle, performance metrics and state-of-the-art have been discussed for each application. In conclusion, the research goal outlines the need and motivation for each project.

In Chapter 1, the background and the operating principle of aerosol jet printing were summarized. The basic system components were introduced, followed by the design and toolpath generation process. Next, a framework for process optimization was presented which explained the detailed process of ink selection, surface treatment, process control and post-processing. Within this framework, the important parameters for ink formulation were discussed. These included viscosity, vapor pressure, surface tension, particle size and encapsulant. Next, the effect of the substrate's surface energy on the wetting characteristics of an ink was reported. Surface treatment methods can reduce the energy mismatch and improve the interfacial interaction between the substrate and the ink. These methods included surface cleaning, plasma treatment and chemical modification of the substrate. It was furthermore demonstrated that the printing geometry can be controlled by adjusting the gas flows, platform temperature, stage speed and nozzle size. The effect of the substrate temperature on the line profile was shown. Lastly, in process control, the importance of post-processing along with most commonly used methods was mentioned. These methods included thermal annealing, laser sintering and UV-exposure. In the end, the major challenges faced during the printing process were presented.

In Chapter 2, a fully printed process for the fabrication of zinc oxide photodetectors for ultraviolet sensing below 150 °C was presented. An approach to obtain porosity in a printed film was demonstrated in order to increase the surface-area-to-volume-ratio for better performance. The device performance was then carefully mapped by performing well-controlled measurements in both air as well as under vacuum. The photoresponse showed a linear increase under vacuum and a superlinear increase in air. In order to explain this phenomenon, an operating mechanism based on Schottkey barrier modification upon adsorption and desorption of oxygen was proposed. Furthermore, this hypothesis was established by the measurements carried out in an air and vacuum environment. These ZnO photodetectors were shown to have a low dark current, high ON/OFF ratios, and fast response times. In conclusion, this work resolved the problems of high temperature processing, vacuum processing and lack of large-area scalability for commercialization and compatibility with flexible-substrates, while exhibiting state-of-the-art photo response.

In Chapter 3, a fully additive packaging technique for chip-on-board applications was introduced. The concept of using printed transmission lines to connect the die to the packaging pins inside a QFN package was proposed. The fabricated microstrip transmission lines were completely printed, both dielectric as well as conductor using aerosol-jet printing. The transmission lines were optimized to have a 50 Ω characteristic impedance and a transmission loss of 0.3 dB/mm at 18 GHz. For the first time, the transmission line to die transition was demonstrated. The transmission loss including the die transition was measured to be 0.9 dB/mm at 18 GHz. In conclusion, this approach would enable applications in higher frequency bands using larger signal bandwidths without resorting to expensive packaging techniques.

In Chapter 4, the concept of system integration of a MMIC with a directly deposited ring resonator inside a package was proposed. An approach to fabricate a fully printed ring resonator at microwave center-frequency was given. The use of microwave frequencies enabled the smaller form factor, which facilitates the in-package integration. All the microwave structures have been characterized up to 26 GHz. The effect of the change in the coupling gap on insertion loss was analyzed. The modulation of center frequency was demonstrated at 15.5, 17.5, 19.5

and 21.5 GHz by controlling the ring size. The ANSYS HFSS simulations are consistent with the measured results in terms of insertion loss, center-frequency and Q factor. Finally, the reliability of the printing process to achieve reproducible devices was verified. In conclusion, this work showed the potential of using printing technologies for high-frequency microwave applications.

5.2 Original Contributions

- Effect of gas flows, stage speed, nozzle size and platform temperature on the AJ printed line profile. **Chapter 1**, Gupta *et al.* (2016)
- An approach to obtain nano-porosity in an AJP printed semiconductor film, which results in high performance metrics by enhancing surface area-to volume-ratio. **Chapter 2**, Gupta *et al.* (2018)
- A below 150 °C fabrication method for printing photodetectors on temperature sensitive flexible substrates, while retaining high ON/OFF ratios comparable to the state-of-the-art. **Chapter 2**, Gupta *et al.* (2018)
- A fully additive technique for fabricating microstrip transmission lines with AJP, utilizing printed SU-8 as dielectric and printed silver as conductor. **Chapter 3 and 4**.
- Realization of the transition from MMIC pad to printed transmission line, characterized up to a frequency of 18 GHz. **Chapter 3**, Gupta *et al.* (2019b)
- Realization of fully printed microwave ring resonators for integration in a MMIC package, operating with center frequencies up to 21.5 GHz. **Chapter 4**, Gupta *et al.* (2019a)

5.3 Discussion

In this thesis, we covered a wide array of subjects, from photodetectors to microwave structures, with the main focus on fabricating electronic components having good performance metrics at low cost, using a direct printing technique. In industrial manufacturing, a low cost is achieved with fully roll-to-roll high speed printing processes, such as flexo, offset or gravure. These processes are less suitable for the rapid prototyping of electronic devices, as their setup cost is high and the minimum batch size is large. In contrast, direct deposition is known to be less expensive as it significantly reduces the total processing cost, by cutting down on material wastage and the fabrication of masks or photopolymer plates. This significantly reduces the prototyping and development cost of electronic devices. In the past decade, the aerosol jet printing system was introduced as a new direct deposition system, promising a wider viscosity range, larger particle size, a finer resolution and a relaxation of nozzle clogging in comparison to inkjet printing. In this work, the challenge was met by exploiting the strengths of the AJP system and then finding suitable applications for the progression of the current state-of-the-art. AJP's application in the diverse fields of optics, packaging and microwave structures demonstrated its multi-faceted potential.

ZnO is a well-know wide band gap semiconductor which is used for a wide range of applications, such as solar cells, photodetectors and transistors. Digital-write techniques such as inkjet are limited to the printing of particle sizes up to 50 nm. Although ZnO nanocrystals are commercially available, their high cost hinders the efforts of developing a low-cost printing process. As an alternative, digital-write techniques have been used to deposit ink formulations based on Zn precursors, which were then converted to ZnO by annealing the substrates at a minimum temperature of 300 °C, which limits the use of temperature sensitive substrates. The ability of AJP to deposit large crystals (upto 1 μm) without clogging not only reduces the cost of ink formulations, but also results in a lower annealing temperature. At annealing temperatures below 150 °C, low-temperature flexible substrates become compatible with the printing process. In addition, the porous semiconductor film has several advantages for sensor applications due to its enhanced surface area-to-volume-ratio. However, such a film is of less interest for transistor applications, as the large number of grain boundaries between the nanocrystals results in insufficient mobility.

Another strength of AJP lies in its ability to print ink formulations having a wide range of viscosity (1-1000 cP) at a high resolution ($\pm$ 10 μm) and with an accurate alignment ($\pm$ 2 μm). These characteristics of AJP are ideal for the printing of transmission lines for in-package high speed connections, as shown in Chapter 3. For the packaging of an MMIC inside a QFN package, low-loss transmission lines need to be printed from the die bondpads to the QFN pins. The transitions across large height differences in such an application are overcome by printing high aspect ratio structures in a single pass utilizing high weight % loading ink formulations. Since the dimensions of the die bondpads are small (60 μm by 60 μm in this work), a fine resolution and high placement accuracy are crucial in preventing short circuits. Moreover, AJP's ability to print dielectric thicknesses in the range of tens-to-hundreds of μm allowed the transmission line to be designed with the correct characteristic impedance for optimal matching.

In extension to Chapter 3, the ability of the AJP system to print fine features and high aspect ratio structures is further used in chapter 4. The ability to print gaps as small as 50 μm and dielectrics as thick as 300 μm makes it possible to construct microwave ring resonators. As a digital-write technique with the capability to overcome height differences, AJP can integrate the resonator together with a MMIC inside a QFN package. Achieving a high Q-factor of the ring requires a low resistive loss in the conductor, which is facilitated by AJP's ability to print a thick conductor in a single pass without overflow or misalignment. At the same time, the coupling gap in the resonator can be tightly controlled, which is essential in realizing optimal coupling.

Despite all the advantages AJP has to offer, it is important to consider the limitations of the system. Since it is a digital-write technique, the throughput of AJP is much lower as compared to roll-to-roll techniques like flexo and offset printing. In general, precise thickness control in AJP is extremely hard to achieve, as many factors influence the flow of mass onto the substrate. Careful monitoring and control of the process parameters is essential in obtaining reproducible results. If very thick films are needed without the need for a high resolution, then screen and offset printing can provide better alternatives. Even though AJP offers high resolution printing, there can be factors that limit the achievable stable line width and separation. Overspray can lead to shorts between low-pitch lines, and must be carefully controlled by the process parameters and by lowering the working distance. In the formulation of inks for the AJP ultrasonic atomizer, we observed that the inclusion of surfactants can lead to foaming in the deposition. The use of de-foamers might alleviate this problem, but requires further investigation.

5.4 Future Work

In chapter 2, we reported a method to print a ZnO thin film with porous morphology for sensing ultraviolet radiation. The increase in surface area per unit volume increases the active area for absorption, thereby significantly improving photosensitivity. In future work, this fabrication method can also be applied to other inorganic semiconductor materials. Enhancing the surface area-to-volume ratio will improve the photo response. Furthermore, in solar cell applications, these semiconductor materials can be functionalized with dyes or quantum dots in order to widen the spectral response. The porous structure will help with dye adsorption and provide more surface area for functionalization.

In chapter 3, we characterized the materials at microwave frequencies (up to 18 GHz) and presented a working prototype of fully printed microstrip transmission lines. We demonstrated transmission line-to-die transition on a printed circuit board. Next, it is envisioned to package the MMIC inside a QFN package, while providing all the interconnections with fully printed transmission lines. The design parameters could be further improved to reduce the losses. It is also envisioned that these transmission lines can be used to make interconnections between the different components on a die or on a PCB.

In chapter 4, the characterization of conductive and dielectric materials was extended up to 26 GHz. Fully printed microwave ring resonators were presented. We demonstrated the modulation of center-frequency by controlling the ring size. As the next step, the design can be further improved in order to achieve higher Q-factor. These microwave ring resonators can be integrated with amplifier dies for sensing applications. This can be done by directly printing these structures inside a package connected to an amplifier with a MMIC in a positive feedback loop. The on-chip amplifier will increase the Q-factor of these devices. Furthermore, it would also be interesting to characterize these materials at higher frequency.

Of additional interest is the increasing awareness and concern for environmental protection in the field of green electronics. Traditional methods not only use hazardous chemicals but also consume more energy resources and create a lot of electronic waste, which ends up in the landfills. Therefore, researchers are looking for more eco-friendly technology to reduce the consumption of silicon electronics. Printed electronics provide one such alternative, at least for low-end applications. In the future, a lot of efforts must be invested to develop high performance ink formulations which are also environmentally sustainable. Using inks which are environment friendly and substrates that can be recycled are a great service to our society for the next generations to come.

LIST OF PUBLICATIONS

Journal Publications

1. **Gupta, A. A.**, Soer, M. C. M., Taherzadeh-Sani, M., Cloutier, S. G. and Izquierdo, R. (2019b). *Aerosol-Jet Printed Transmission Lines for Microwave Packaging Applications*. Submitted to IEEE Transactions on Components, Packaging and Manufacturing Technology.
2. **Gupta, A. A.**, Rahmani, M. H., Soer, M. C. M., Taherzadeh-Sani, M., Cloutier, S. G. and Izquierdo, R. (2019a). *Aerosol Jet Printed, Microwave Microstrip Ring Resonators for Sensing Applications*. Submitted to IEEE Transactions on Components, Packaging and Manufacturing Technology.
3. **Gupta, A. A.**, Arunachalam, S., Cloutier, S. G. and Izquierdo, R. (2018). *Fully Aerosol-Jet Printed, High-Performance Nanoporous ZnO Ultraviolet Photodetectors*. ACS Photonics, 5(10), 3923-3929. doi: 10.1021/acsphotonics.8b00829.
4. Arunachalam, S., **Gupta, A. A.**, Izquierdo, R. and Nabki, F. (2018). *Suspended Carbon Nanotubes for Humidity Sensing*. Sensors, 18(5), 1655. https://doi.org/10.3390/s18051655

Conference Publications

1. **Gupta, A. A.**, Arunachalam, S., Cloutier, S. G. and Izquierdo, R. (2018), *Fully Printed, ZnO Photodetectors for Ultraviolet Sensing*, 20th Photonics North Conference.
2. **Gupta, A. A.**, Bolduc, A., Cloutier, S. G. and Izquierdo, R. (2016, May). *Aerosol Jet Printing for printed electronics rapid prototyping*. 2016 IEEE International Symposium on Circuits and Systems (ISCAS), pp. 866-869. doi: 10.1109/ISCAS.2016.7527378.
3. **Gupta, A. A.**, Cloutier, S. G. and Izquierdo, R. (2015), *Aerosol Jet Printing: Enabling the Next Wave in Printing Electronics*, Canadian Printable Electronics Symposium 2015.

BIBLIOGRAPHY

A. Mahajan, C. d. F. & Francis, L. F. (2013). Optimization of Aerosol Jet Printing for High-Resolution, High-Aspect Ratio Silver Lines. *ACS Applied Materials and Interfaces*.

Abdelghani, A., Bahoumina, P., Hallil, H., Bila, S., Baillargeat, D., Frigue, K., Delhote, N., Lachaud, J. L., Coquet, P., Ravichandran, A., Pichonat, E., Paragua, C., Happy, H., Rebiare, D. & Dejous, C. (2017, June). Capacitive microwave resonator printed on a paper substrate for CNT based gas sensor. *2017 IEEE MTT-S International Microwave Symposium (IMS)*, pp. 513-516. doi: 10.1109/MWSYM.2017.8058611.

Aga, R., Lombardi, J., Bartsch, C. & Heckman, E. (2014). Performance of a Printed Photodetector on a Paper Substrate. *IEEE Photonics Technology Letters*.

Ahmad, W., Budimir, D., Maric, A. & Ivanisevic, N. (2015, July). Inkjet printed bandpass filters and filtennas using silver nanoparticle ink on flexible substrate. *2015 IEEE International Symposium on Antennas and Propagation USNC/URSI National Radio Science Meeting*, pp. 145-146. doi: 10.1109/APS.2015.7304458.

Andersson, P., Forchheimer, R., Tehrani, P. & Berggren, M. (2007). Printable All-Organic Electrochromic Active-Matrix Displays. *Wiley Advanced Functional Materials*.

Antognazza, M. R., Scherf, U., Monti, P. & Lanzani, G. (2007). Organic-based tristimuli colorimeter . *Applied Physics Letters*.

Antognazza, M. R., Musitelli, D., Perissinotto, S. & Lanzani, G. (2010). Spectrally selected photodiodes for colorimetric application . *Elsevier Organic Electronics*.

Arias, A. C., MacKenzie, J. D., McCulloch, I., Rivnay, J. & Salleo, A. (2010). Materials and Applications for Large Area Electronics: Solution-Based Approaches. *Chem. Rev.*

Armin, A., van Vuuren, R. D. J., Kopidakis, N., Burn, P. L. & Meredith, P. (2015). Narrowband light detection via internal quantum efficiency manipulation of organic photodiodes. *Nature Communications*.

Azucena, O., Kubby, J., Scarbrough, D. & Goldsmith, C. (2008, June). Inkjet printing of passive microwave circuitry. *2008 IEEE MTT-S International Microwave Symposium Digest*, pp. 1075-1078. doi: 10.1109/MWSYM.2008.4633242.

Azzellino, G., Grimoldi, A., Binda, M., Caironi, M., Natali, D. & Sampietro, M. (2013). Fully Inkjet-Printed Organic Photodetectors with High Quantum Yield. *Wiley Advanced Materials*.

Babarinde, O. J., Petrocchi, A., Volskiy, V., Ocket, I. & Schreurs, D. (2018, March). Development of a planar microwave resonator based wetness sensor. *2018 11th German Microwave Conference (GeMiC)*, pp. 199-202. doi: 10.23919/GEMIC.2018.8335064.

Bahar, A. A. M., Zakaria, Z., Rashid, S. R. A., Isa, A. A. M., Alahnomi, R. A. & Dasril, Y. (2017a, March). Microfluidic planar resonator sensor with highly precise measurement for microwave applications. *2017 11th European Conference on Antennas and Propagation (EUCAP)*, pp. 1843-1846. doi: 10.23919/EuCAP.2017.7928521.

Bahar, A. A. M., Zakaria, Z., Rashid, S. R. A., Isa, A. A. M. & Alahnomi, R. A. (2017b). High-Efficiency Microwave Planar Resonator Sensor Based on Bridge Split Ring Topology. *IEEE Microwave and Wireless Components Letters*, 27(6), 545-547. doi: 10.1109/LMWC.2017.2701338.

Bai, S., Wu, W., Qin, Y., Cui, N., Bayerl, D. J. & Wang, X. (2011). High-Performance Integrated ZnO Nanowire UV Sensors on Rigid and Flexible Substrates. *Advanced Functional Materials*, 21(23), 4464–4469. doi: 10.1002/adfm.201101319.

Basak, D., Amin, G., Mallik, B., Paul, G. & Sen, S. (2003). Photoconductive {UV} detectors on solgel-synthesized ZnO films. *Journal of Crystal Growth*, 256, 73 - 77. doi: http://dx.doi.org/10.1016/S0022-0248(03)01304-6.

Beag, K., Binda., M., Natali, D., Caironi, M. & Noh, Y. (2013). Organic Light Detectors: Photodiodes and Phototransistors. *Wiley Advanced Materials*.

Belhaj, M. M., Wei, W., Pallecchi, E., Mismer, C., Roch-jeune, I. & Happy, H. (2014, Oct). Inkjet printed flexible transmission lines for high frequency applications up to 67 GHz. *2014 44th European Microwave Conference*, pp. 1528-1531. doi: 10.1109/EuMC.2014.6986740.

Bernacka-Wojcik, I., Senadeera, R., Wojcik, P., Silva, L., Doria, G., Baptista, P., Anguas, H., Fortunato, E. & Martins, R. (2009). Inkjet printed and "doctor-blade" TiO2 pphotodetectors for DNA biosensors. *Elsevier Biosensors and Bioelectronics*.

Bessemoulin, A., Parisot, M. & Camiade, M. (2004, June). 1-Watt Ku-band power amplifier MMICs using low-cost quad-flat plastic package. *2004 IEEE MTT-S International Microwave Symposium Digest (IEEE Cat. No.04CH37535)*, 2, 473-476 Vol.2. doi: 10.1109/MWSYM.2004.1336015.

Boberl, M., Kovalenko, M., Gamerith, S., List, E. & Heiss, W. (2007). Inkjet-Printed Nanocrystal Photodetectors Operating up to 3 μm Wavelengths. *Wiley Advanced Materials*.

Bohling, D. (2011). Surface and Substrate Preparation. *AJ International Users Group Presentations*.

Braga, D., Erickson, N. C., Renn, M. J., Holmes, R. J. & Frisbie, C. D. (2012). High-Transconductance Organic Thin-Film Electrochemical Transistors for Driving Low-Voltage Red-Green-Blue Active Matrix Organic Light-Emitting Devices. *Wiley Advanced Functional Materials*.

Brillson, L. J. & Lu, Y. (2011). ZnO Schottky barriers and Ohmic contacts. *Journal of Applied Physics*, 109(12). doi: http://dx.doi.org/10.1063/1.3581173.

Brivio, M., Verboom, W. & Reinhoudt, D. N. (2005). Miniaturized continuous flow reaction vessels: influence on chemical reactions. *RSC Lab on a Chip*.

Cai, F., h. Chang, Y., Wang, K., Khan, W. T., Pavlidis, S. & Papapolymerou, J. (2014, June). High resolution aerosol jet printing of D- band printed transmission lines on flexible LCP substrate. *2014 IEEE MTT-S International Microwave Symposium (IMS2014)*, pp. 1-3. doi: 10.1109/MWSYM.2014.6848597.

Cai, F., Chang, Y. H., Wang, K., Zhang, C., Wang, B. & Papapolymerou, J. (2016). Low-Loss 3-D Multilayer Transmission Lines and Interconnects Fabricated by Additive Manufacturing Technologies. *IEEE Transactions on Microwave Theory and Techniques*, 64(10), 3208-3216. doi: 10.1109/TMTT.2016.2601907.

Chang, K. & Hsieh, L.-H. (2004). *Microwave Ring Circuits and Related Structures*. John Wiley and Sons, Inc.

Chason, M., Brazis, P., Zhang, J., Kalyanasundaram, K. & Gamota, D. (2005). Printed Organic Semiconducting Devices. *Proceeedings of the IEEE*.

Chen, K., Hung, F., Chang, S. & Young, S. (2009). Optoelectronic characteristics of {UV} photodetector based on ZnO nanowire thin films. *Journal of Alloys and Compounds*, 479, 674 - 677. doi: http://dx.doi.org/10.1016/j.jallcom.2009.01.026.

Chen, Miaoxiang. (2005). Printed Electrochemical Devices Using Conducting Polymers as Active Materials on Flexible Substrates. *Proceedings of the IEEE*.

Cheng, G., Wu, X., Liu, B., Li, B., Zhang, X. & Du, Z. (2011). ZnO nanowire Schottky barrier ultraviolet photodetector with high sensitivity and fast recovery speed. *Applied Physics Letters*, 99(20). doi: http://dx.doi.org/10.1063/1.3660580.

Cheng, J., Zhang, Y. & Guo, R. (2008). ZnO microtube ultraviolet detectors. *Journal of Crystal Growth*, 310(1), 57 - 61. doi: http://dx.doi.org/10.1016/j.jcrysgro.2007.08.034.

Cheng, X., Zhao, H., Huo, L., Gao, S. & Zhao, J. (2004). ZnO nanoparticulate thin film: preparation, characterization and gas-sensing property. *Sensors and Actuators B: Chemical*, 102(2), 248 - 252. doi: http://dx.doi.org/10.1016/j.snb.2004.04.080.

Cho, J. H., Lee, J., Xia, Y., Kim, B., He, Y., Renn, M. J., Lodge, T. P. & Frisbie, C. D. (2008). Printable ion-gel gate dielectrics for low-voltage polymer thin-film transistors on plastic. *Nature Materials*.

Chung, S., Ul Karim, M. A., Kwon, H.-J. & Subramanian, V. (2015). High-Performance Inkjet-Printed Four-Terminal Microelectromechanical Relays and Inverters. *Nano Letters*, 15(5), 3261-3266. doi: 10.1021/acs.nanolett.5b00477. PMID: 25830693.

Clifford, J. P., Konstantatos, G., Johnston, K. W., Hoogland, S., Levina, L. & Sargent, E. H. (2008). Fast, sensitive and spectrally tuneable colloidal- quantum-dot photodetectors. *Nature Nanotechnology Letters*.

Cook, B. S., Tehrani, B., Cooper, J. R. & Tentzeris, M. M. (2013). Multilayer Inkjet Printing of Millimeter-Wave Proximity-Fed Patch Arrays on Flexible Substrates. *IEEE Antennas and Wireless Propagation Letters*, 12, 1351-1354. doi: 10.1109/LAWP.2013.2286003.

David, J., Ralph, E., Maximilian, S. L., Norman, B., Gerardo, H., C., B. J., Ibraheem, A., Uli, L. & Martin, K. Digital Aerosol Jet Printing for the Fabrication of Terahertz Metamaterials. *Advanced Materials Technologies*, 3(2), 1700236. doi: 10.1002/admt.201700236.

Deegan, R. D., Bakajin, O., Dupont, T. F., Huber, G., Nagel, S. R. & Witten, T. A. (1997). Capillary flow as the cause of ring stains from dried liquid drops. *Nature*.

Dongre, G., van Weerd, J., Besselink, G. A. J., Vazquez, R. M., Osellame, R., Cerullo, G., van Weeghel, R., van den Vlekkert, H. H., Hoekstraa, H. J. W. M. & Pollnau, M. (2010). Modulation-frequency encoded multi-color fluorescent DNA analysis in an optofluidic chip. *RCS Lab on a Chip*.

Essien, M. (2011). Sources of and Minimization of Line Defects. *AJ International Users Group Presentations*.

Ghalichechian, N. & Sertel, K. (2015). Permittivity and Loss Characterization of SU-8 Films for mmW and Terahertz Applications. *IEEE Antennas and Wireless Propagation Letters*, 14, 723-726. doi: 10.1109/LAWP.2014.2380813.

Ghannam, A., Viallon, C., Bourrier, D. & Parra, T. (2009, Sept). Dielectric microwave characterization of the SU-8 thick resin used in an above IC process. *2009 European Microwave Conference (EuMC)*, pp. 1041-1044. doi: 10.23919/EUMC.2009.5295989.

Ghosh, T. & Basak, D. (2010). Highly efficient ultraviolet photodetection in nanocolumnar RF sputtered ZnO films: a comparison between sputtered, solgel and aqueous chemically grown nanostructures. *Nanotechnology*, 21(37), 375202. Consulted at http://stacks.iop.org/0957-4484/21/i=37/a=375202.

Gonzalez, G. (1997). *Microwave Transistor Amplifiers: Analysis and Design*. Prentice Hall. Consulted at https://books.google.ca/books?id=-AVTAAAAMAAJ.

Goth, C., Putzo, S. & Franke, J. (2011). Aerosol Jet Printing on Rapid Prototyping Materials for Fine Pitch Electronic Applications. *IEEE Electronic Components and Technology Conference*.

Greig, W. (2007). *Integrated Circuit Packaging, Assembly and Interconnections*. Springer US. Consulted at https://books.google.ca/books?id=g29xoTAyAMgC.

Grunwald, I., Groth, E., Wirth, I., Schumacher, J., Maiwald, M., Zoellmer, V. & Busse, M. (2010). Surface biofunctionalization and production of miniaturized sensor structures using aerosol printing technologies. *Biofabrication*.

Gunes, S., Neugebauer, H. & Sariciftci, N. S. (2007). Conjugated Polymer-Based Organic Solar Cells. *Chemical Reviews*.

Gupta, A. A., Bolduc, A., Cloutier, S. G. & Izquierdo, R. (2016, May). Aerosol Jet Printing for printed electronics rapid prototyping. *2016 IEEE International Symposium on Circuits and Systems (ISCAS)*, pp. 866-869. doi: 10.1109/ISCAS.2016.7527378.

Gupta, A. A., Arunachalam, S., Cloutier, S. G. & Izquierdo, R. (2018). Fully Aerosol-Jet Printed, High-Performance Nanoporous ZnO Ultraviolet Photodetectors. *ACS Photonics*, 5(10), 3923-3929. doi: 10.1021/acsphotonics.8b00829.

Gupta, A. A., Rahmani, M. H., Soer, M. C. M., Taherzadeh-Sani, M., Cloutier, S. G. & Izquierdo, R. (2019a). Aerosol Jet Printed, Microwave Microstrip Ring Resonators for Sensing Applications. *Submitted to IEEE Transactions on Components, Packaging and Manufacturing Technology*.

Gupta, A. A., Soer, M. C. M., Taherzadeh-Sani, M., Cloutier, S. G. & Izquierdo, R. (2019b). Aerosol-Jet Printed Transmission Lines for Microwave Packaging Applications. *Submitted to IEEE Transactions on Components, Packaging and Manufacturing Technology*.

Ha, M., Seo, J.-W., Prabhumirashi, P., Zhang, W., Geier, M., Renn, M., Kim, C., Hersam, M. & Frisbie, C. (2013a). Aerosol jet printed, low voltage, electrolyte gated carbon nanotube ring oscillators with sub-5 μs stage delays. *Nano Letters*.

Ha, M., Zhang, W., Braga, D., Renn, M., Kim, C. & Frisbie, C. (2013b). Aerosol-jet-printed, 1 volt h-bridge drive circuit on plastic with integrated electrochromic pixel. *ACS Applied Materials and Interfaces*.

Hassan, N., Hashim, M. & Allam, N. K. (2013). Low power UV photodetection characteristics of cross-linked ZnO nanorods/nanotetrapods grown on silicon chip. *Sensors and Actuators A: Physical*, 192, 124 - 129. doi: http://dx.doi.org/10.1016/j.sna.2012.12.040.

Hauhe, M. S. & Wooldridge, J. J. (1997). High density packaging of X-band active array modules. *IEEE Transactions on Components, Packaging, and Manufacturing Technology: Part B*, 20(3), 279-291. doi: 10.1109/96.618228.

Haverinen, H. M., Myllyla, R. A. & Jabbour, G. E. (2010). Inkjet Printed RGB Quantum Dot-Hybrid LED. *Journal of Display Technology*, 6(3), 87-89. doi: 10.1109/JDT.2009.2039019.

Hedges, M. & Marin, A. (2012). 3D Aerosol Jet Printing - Adding Electronics Functionality to RP/RM. *Direct Digital Manufacturing Conf.*

Herrojo, C., Mata-Contreras, J., Paredes, F. & Martin, F. (2017). Microwave Encoders for Chipless RFID and Angular Velocity Sensors Based on S-Shaped Split Ring Resonators. *IEEE Sensors Journal*, 17(15), 4805-4813. doi: 10.1109/JSEN.2017.2715982.

Higashi, Y., Kim, K.-S., Jeon, H.-G. & Ichikawa, M. (2010). Enhancing spectral contrast in organic red-light photodetectors based on a light- absorbing and exciton-blocking layered system. *Journal of Applied Physics*.

Hoerber, J., Goth, C., Franke, J. & Hedges, M. (2011). Electrical Functionalization of Thermoplastic Materials by Aerosol Jet Printing. *IEEE Electronics Packaging Technology Conference*.

Hong, K., Kim, S. H., Lee, K. H. & Frisbie, C. D. (2013). Printed, sub-2V ZnO Electrolyte Gated Transistors and Inverters on Plastic. *Wiley Advanced Materials*.

Horowitz, G. (1999). Field-effect transistors based on short organic molecules. *Journal of Materials Chemistry*.

Huh, J., Kim, Y., Park, Y., Choi, J., Lee, J., Lee, J., Yang, J., Ju, S., Paek, K. & Ju, B. (2008). Characteristics of organic light-emitting diodes with conducting polymer anodes on plastic substrates. *Journal of Applied Physics*.

Hullavarad, S., Hullavarad, N., Look, D. & Claflin, B. (2009). Persistent Photoconductivity Studies in Nanostructured ZnO UV Sensors. *Nanoscale Research Letters*, 4(12), 1421–1427.

Hullavarad, S., Hullavarad, N., Karulkar, P., Luykx, A. & Valdivia, P. (2007). Ultra violet sensors based on nanostructured ZnO spheres in network of nanowires: a novel approach. *Nanoscale Research Letters*, 2(3), 161–167. doi: 10.1007/s11671-007-9048-6.

IDTechEx Research. (2018). *Flexible, Printed and Organic Electronics 2019-2029: Forecasts, Players and Opportunities*.

J. Renn, M., King, B., Oreilly, M., Leal, J. & Pangrle, S. (2010). Aerosol Jet Printing of High Density, 3-D Interconnects for Multi-Chip Packaging. *Additional Conferences (Device Packaging, HiTEC, HiTEN, CICMT)*, 2010, 002131-002152. doi: 10.4071/2010DPC-tha15.

Jain, N. (2000, June). Designing commercially viable MM-wave modules. *2000 IEEE MTT-S International Microwave Symposium Digest (Cat. No.00CH37017)*, 1, 565-568 vol.1. doi: 10.1109/MWSYM.2000.861126.

Jiang, D., Zhang, J., Lu, Y., Liu, K., Zhao, D., Zhang, Z., Shen, D. & Fan, X. (2008). Ultraviolet Schottky detector based on epitaxial ZnO thin film. *Solid-State Electronics*, 52(5), 679 - 682. doi: http://dx.doi.org/10.1016/j.sse.2007.10.040.

Jin, Y., Wang, J., Sun, B., Blakesley, J. C. & Greenham, N. C. (2008). Solution-Processed Ultraviolet Photodetectors Based on Colloidal ZnO Nanoparticles. *Nano Letters*, 8(6), 1649-1653. doi: 10.1021/nl0803702. PMID: 18459745.

Jing, D., Mingliang, H. & Wei, Z. (2017, Oct). A well-designed sensor based on split-ring resonators at microwave frequencies. *2017 7th IEEE International Symposium on Microwave, Antenna, Propagation, and EMC Technologies (MAPE)*, pp. 47-48. doi: 10.1109/MAPE.2017.8250793.

Jung, S., Sou, A., Gili, E. & Sirringhaus, H. (2013). Inkjet-printed resistors with a wide resistance range for printed read-only memory applications. *Organic Electronics*, 14(3), 699 - 702. doi: https://doi.org/10.1016/j.orgel.2012.12.034.

Kahn, B. E. (2007). The M3D Aerosol Jet System, an Alternative to Inkjet Printing for Printed Electronics. *Organic & Printed Electronics*.

Kamyshny, A. & Magdassi, S. (2014). Conductive Nanomaterials for Printed Electronics. *Small*, 10(17), 3515–3535.

Kang, B. J., Lee, C. K. & Oh, J. H. (2012). All-inkjet-printed electrical components and circuit fabrication on a plastic substrate. *Microelectronic Engineering*, 97, 251 - 254. doi: https://doi.org/10.1016/j.mee.2012.03.032. Micro- and Nano-Engineering (MNE) 2011, selected contributions: Part I.

Karimi, M. A., Arsalan, M. & Shamim, A. (2017, June). A low cost, printed microwave based level sensor with integrated oscillator readout circuitry. *2017 IEEE MTT-S International Microwave Symposium (IMS)*, pp. 1742-1745. doi: 10.1109/MWSYM.2017.8058980.

Khan, S., Lorenzelli, L. & Dahiya, R. (2015). Technologies for Printing Sensors and Electronics Over Large Flexible Substrates: A Review. *Sensors Journal, IEEE*, 15(6), 3164-3185.

Kim, B. H., Lee, Y. J., Lee, H. J., Hong, Y., Yook, J. G., Chung, M. H., Cho, W. & Choi, H. H. (2014, Nov). A gas sensor using double split-ring resonator coated with conducting polymer at microwave frequncies. *IEEE SENSORS 2014 Proceedings*, pp. 1815-1818. doi: 10.1109/ICSENS.2014.6985379.

Kim, J.-Y., Lee, H.-Y., Lee, J.-H. & Chang, D.-P. (2000). Wideband characterization of multiple bondwires for millimeter-wave applications. *2000 Asia-Pacific Microwave Conference. Proceedings (Cat. No.00TH8522)*, pp. 1265-1268. doi: 10.1109/APMC.2000.926064.

Kim, S. H., Hong, K., Xie, W., Lee, K. H., Zhang, S., Lodge, T. P. & Frisbie, C. D. (2013a). Electrolyte-Gated Transistors for Organic and Printed Electronics. *Wiley Advanced Materials*.

Kim, S., Hong, K., Lee, K. & Frisbie, C. (2013b). Performance and stability of aerosol-jet-printed electrolyte-gated transistors based on poly(3-hexylthiophene). *ACS Applied Materials and Interfaces*.

Kind, H., Yan, H., Messer, B., Law, M. & Yang, P. (2002). Nanowire Ultraviolet Photodetectors and Optical Switches. *Advanced Materials*, 14(2), 158–160. doi: 10.1002/1521-4095(20020116)14:2<158::AID-ADMA158>3.0.CO;2-W.

Kitazawa, K., Koriyama, S., Minamiue, H. & Fujii, M. (2000). 77-GHz-band surface mountable ceramic package. *IEEE Transactions on Microwave Theory and Techniques*, 48(9), 1488-1491. doi: 10.1109/22.868999.

Konstantatos, G. & Sargent, E. H. (2010). Nanostructured materials for photon detection. *Nat Nano*, 5(6), 391–400. Consulted at http://dx.doi.org/10.1038/nnano.2010.78.

Konstantatos, G., Badioli, M., Gaudreau, L., Osmond, J., Bernechea, M., de Arquer, F. P. G., Gatti, F. & Koppens, F. H. L. (2012). Hybrid graphene quantum dot phototransistors with ultrahigh gain. *Nature Nanotechnology Letters*.

Kopola, P., Zimmermann, B., Filipovic, A., Schleiermacher, H.-F., Greulich, J., Rousu, S., Hast, J., Myllylä, R. & Würfel, U. (2012). Aerosol jet printed grid for ITO-free inverted organic solar cells. *Wiley Solar Energy Materials and Solar Cells*.

Lavery, L. L., Whiting, G. L. & Arias, A. C. (2011). All ink-jet printed polyfluorene photosensor for high illuminance detection. *Elsevier Organic Electronics*.

Law, J. B. K. & Thong, J. T. L. (2006). Simple fabrication of a ZnO nanowire photodetector with a fast photoresponse time. *Applied Physics Letters*, 88(13). doi: http://dx.doi.org/10.1063/1.2190459.

Lhuillier, E., Robin, A., Ithurria, S., Aubin, H. & Dubertret, B. (2014). Electrolyte-Gated Colloidal Nanoplatelets-Based Phototransistor and Its Use for Bicolor Detection. *ACS Nano Leters*.

Li, S., Tang, W., Xu, X., Cao, M., Jin, Y. & Guo, X. (2014). Comparative study of encapsulated solution-processed zinc oxide ultraviolet photodetectors with different contacts. *physica status solidi (a)*, 211(9), 2184–2188. doi: 10.1002/pssa.201431220.

Liang, M., Yu, X., Shemelya, C., MacDonald, E. & Xin, H. (2015, May). 3D printed multilayer microstrip line structure with vertical transition toward integrated systems. *2015 IEEE MTT-S International Microwave Symposium*, pp. 1-4. doi: 10.1109/MWSYM.2015.7167016.

Liang, S., Sheng, H., Liu, Y., Huo, Z., Lu, Y. & Shen, H. (2001). ZnO Schottky ultraviolet photodetectors. *Journal of Crystal Growth*, 225, 110 - 113. doi: http://dx.doi.org/10.1016/S0022-0248(01)00830-2. Proceedings of the 12th American Conference on Crystal Growth and Epitaxy.

Liu, D., Pfeiffer, U., Grzyb, J. & Gaucher, B. (2009). *Advanced Millimeter-wave Technologies: Antennas, Packaging and Circuits*. Wiley. Consulted at https://books.google.ca/books?id=iVtrwmDCn7oC.

Liu, K., Sakurai, M. & Aono, M. (2010). ZnO-Based Ultraviolet Photodetectors. *Sensors*, 10(9), 8604. doi: 10.3390/s100908604.

Liu, R., Shen, F., Ding, H., Lin, J., Gu, W., Cui, Z. & Zhang, T. (2013). All-carbon-based field effect transistors fabricated by aerosol jet printing on flexible substrates. *Journal of Micromechanics and Microengineering*.

Liu, X., Gu, L., Zhang, Q., Wu, J., Long, Y. & Fan, Z. (2014). All-printable band-edge modulated ZnO nanowire photodetectors with ultra-high detectivity. *Nat Commun*, 5. Consulted at http://dx.doi.org/10.1038/ncomms5007.

Liu, Y., Varahramyan, K. & Cui, T. (2005). Low-Voltage All-Polymer Field-Effect Transistor Fabricated Using an Inkjet Printing Technique. *Macromolecular Rapid Communications*.

Luo, S. & Zhu, L. (2009). A Novel Dual-Mode Dual-Band Bandpass Filter Based on a Single Ring Resonator. *IEEE Microwave and Wireless Components Letters*, 19(8), 497-499. doi: 10.1109/LMWC.2009.2024826.

Lupan, O., Chow, L., Chai, G., Chernyak, L., Lopatiuk-Tirpak, O. & Heinrich, H. (2008). Focused-ion-beam fabrication of ZnO nanorod-based UV photodetector using the in-situ lift-out technique. *physica status solidi (a)*, 205(11), 2673–2678. doi: 10.1002/pssa.200824233.

Lupo, D., Clemens, W., Breitung, S. & Hecker, K. (2013). OE-A Roadmap for Organic and Printed Electronics. In Cantatore, E. (Ed.), *Applications of Organic and Printed Electronics* (pp. 1-26). Springer US.

Ma, X., Xu, F., Benavides, J. & Cloutier, S. (2011). Hybrid Polymer-Nanocrystal Heterostructures for High-Performance Chip-Integrated Near-Infrared LEDs. *IEEE International Conference on Group IV Photonics*.

Ma, Z., Cai, P., Guan, X., Kobayashi, Y. & Anada, T. (2007, June). A Novel Millimeter-Wave Ultra-Wideband Bandpass Filter Using Microstrip Dual-Mode Ring Resonators Loaded with Open Tuning Stubs of Different Lengths. *2007 IEEE/MTT-S International Microwave Symposium*, pp. 743-746. doi: 10.1109/MWSYM.2007.380046.

Mahdi, N., Kisslinger, R., Sharma, H., Zarifi, M. H., Daneshmand, M. & Shankar, K. (2016, Oct). Microwave resonator sensor integrated with nanostructured semiconductor membranes for photodetection and carrier lifetime measurement. *2016 IEEE SENSORS*, pp. 1-3. doi: 10.1109/ICSENS.2016.7808782.

Maiellaro, G. & et al. (2014). Ambient Light Organic Sensor in a Printed Complementary Organic TFT Technology on Flexible Plastic Foil. *Circuits and Systems I: Regular Papers, IEEE Transactions on*, 61(4), 1036-1043. doi: 10.1109/TCSI.2013.2286031.

Maiellaro, G., Ragonese, E., Gwoziecki, R., Jacobs, S., Marjanovic, N., Chrapa, M., Schleuniger, J. & Palmisano, G. (2014). Ambient Light Organic Sensor in a Printed Complementary Organic TFT Technology on Flexible Plastic Foil. *IEEE Transactions on Circuits and Systems - I.*

Maksimenko, I., Kilian, D., Mehringer, C., Voigt, M., Peukert, W. & Wellmann, P. (2011). Fabrication, charge carrier transport, and application of printable nanocomposites based on indium tin oxide nanoparticles and conducting polymer 3,4-ethylenedioxythiopene/polystyrene sulfonic acid. *Journal of Applied Physics*.

Mandić, T. (2013). *Modelling of integrated Circuit Packages and Electromagnetic Coupling to Interconnects*. (Ph.D. thesis, Department of Electrical Engineering; Faculty of Electrical Engineering and Computing, KU Leuven; Sveučilište u Zagrebu).

Maria, A., Cyr, P., Klem, E., Levina, L. & Sargent, E. (2005). Solution-processed infrared photovoltaic devices with >10% monochromatic internal quantum efficiency. *Applied Physics Letters*.

Mariotti, C., Su, W., Cook, B. S., Roselli, L. & Tentzeris, M. M. (2015). Development of Low Cost, Wireless, Inkjet Printed Microfluidic RF Systems and Devices for Sensing or Tunable Electronics. *IEEE Sensors Journal*, 15(6), 3156-3163. doi: 10.1109/JSEN.2014.2374874.

Markets and markets. (2018). *Printed electronics Market by Material (Inks and Substrates), Technology (Inkjet, Screen, Gravure, and Flexographic), Device (Sensors, Displays, Batteries, RFID tags, Lighting solutions/panels, and PV Cells), Industry, and Geography - Global Forecast to 2023*.

Marroncelli, M., Trinchero, D. & Tentzeris, M. M. (2011, Aug). Paper-based, inkjet-printed, text-meandered UHF resonant antennas for RFID applications. *2011 XXXth URSI General Assembly and Scientific Symposium*, pp. 1-4. doi: 10.1109/URSIGASS.2011.6050582.

Matsuo, M., Yabuki, H. & Makimoto, M. (2001). Dual-mode stepped-impedance ring resonator for bandpass filter applications. *IEEE Transactions on Microwave Theory and Techniques*, 49(7), 1235-1240. doi: 10.1109/22.932241.

McDonald, S. A., Konstantato, G., Zhang, S., Cyr, P. W., Klem, E. J. D., Levina, L. & Sargent, E. H. (2005). Solution-processed PbS quantum dot infrared photodetectors and photovoltaics. *Nature Materials*.

McQuiddy, D. N., Wassel, J. W., LaGrange, J. B. & Wisseman, W. R. (1984). Monolithic Microwave Integrated Circuits: An Historical Perspective. *IEEE Transactions on Microwave Theory and Techniques*, 32(9), 997-1008. doi: 10.1109/TMTT.1984.1132813.

Meyers, S. T., Anderson, J. T., Hung, C. M., Thompson, J., Wager, J. F. & Keszler, D. A. (2008). Aqueous Inorganic Inks for Low-Temperature Fabrication of ZnO TFTs. *Journal of the American Chemical Society*, 130(51), 17603-17609. doi: 10.1021/ja808243k. PMID: 19053193.

Midford, T. A., Wooldridge, J. J. & Sturdivant, R. L. (1995). The evolution of packages for monolithic microwave and millimeter-wave circuits. *IEEE Transactions on Antennas and Propagation*, 43(9), 983-991. doi: 10.1109/8.410215.

Mishra, Y. K., Modi, G., Cretu, V., Postica, V., Lupan, O., Reimer, T., Paulowicz, I., Hrkac, V., Benecke, W., Kienle, L. & Adelung, R. (2015). Direct Growth of Freestanding ZnO Tetrapod Networks for Multifunctional Applications in Photocatalysis, UV Photodetection, and Gas Sensing. *ACS Applied Materials & Interfaces*, 7(26), 14303-14316. doi: 10.1021/acsami.5b02816. PMID: 26050666.

Molesa, S. E. (2006). *Ultra-Low-Cost Printed Electronics*. (Ph.D. thesis, EECS Department, University of California, Berkeley). Consulted at http://www2.eecs.berkeley.edu/Pubs/TechRpts/2006/EECS-2006-55.html.

Monroy, E., Calle, F., Pau, J., Muoz, E., Omns, F., Beaumont, B. & Gibart, P. (2001). AlGaN-based {UV} photodetectors. *Journal of Crystal Growth*, 230, 537 - 543. doi: http://dx.doi.org/10.1016/S0022-0248(01)01305-7. Proceedings of the Fourth European Workshop on Gallium Nitride.

Oakley, C., Kaur, A., Byford, J. A. & Chahal, P. (2017, May). Aerosol-Jet Printed Quasi-Optical Terahertz Filters. *2017 IEEE 67th Electronic Components and Technology Conference (ECTC)*, pp. 248-253. doi: 10.1109/ECTC.2017.233.

Occhipinti, L. & Fortuna, L. (2002). Organic molecules and composites with applications in micro and nanoelectronic systems. *ISCAS 2002.*, 4, IV-297-IV-300 vol.4.

Olukoya, O. & Budimir, D. (2016, Dec). Inkjet-printed bandstop filters for interference suppression in multi-standard wireless systems. *2016 Asia-Pacific Microwave Conference (APMC)*, pp. 1-4. doi: 10.1109/APMC.2016.7931399.

Oppermann, M. (1998, Apr). Multichip-modules (MCMs) for micro- and millimeter-wave applications-a challenge? *Proceedings. 1998 International Conference on Multichip Modules and High Density Packaging (Cat. No.98EX154)*, pp. 279-284. doi: 10.1109/ICMCM.1998.670794.

Ozgur, U., Alivov, Y. I., Liu, C., Teke, A., Reshchikov, M. A., Dogan, S., Avrutin, V., Cho, S. & Morkoc, H. (2005). A comprehensive review of ZnO materials and devices. *Journal of Applied Physics*, 98(4). doi: http://dx.doi.org/10.1063/1.1992666.

Palesko, C. A. & Vardaman, E. J. (2010, June). Cost comparison for flip chip, gold wire bond, and copper wire bond packaging. *2010 Proceedings 60th Electronic Components and Technology Conference (ECTC)*, pp. 10-13. doi: 10.1109/ECTC.2010.5490877.

Panigrahi, S. & Basak, D. (2012). Solution-processed novel core-shell n-p heterojunction and its ultrafast UV photodetection properties. *RSC Adv.*, 2, 11963-11968. doi: 10.1039/C2RA21518G.

Park, J., & Moon*, J. (2006). Control of Colloidal Particle Deposit Patterns within Picoliter Droplets Ejected by Ink-Jet Printing. *Langmuir*, 22(8), 3506-3513.

Parker, D. (2002). Microwave industry outlook - defense applications. *IEEE Transactions on Microwave Theory and Techniques*, 50(3), 1039-1041. doi: 10.1109/22.989990.

Paulsen, J., Renn, M., Christenson, K. & Plourde, R. (2012). Printing conformal electronics on 3D structures with aerosol jet technology. *Future of Instrumentation International Workshop*.

Pennathur, S. & Fygenson, D. K. (2008). Improving fluorescence detection in lab on chip devices. *RCS Lab on a Chip*.

Pozar, D. (2004). *Microwave Engineering*. Wiley. Consulted at https://books.google.ca/books?id=4wzpQwAACAAJ.

Qi, D., Fischbein, M., Drndi, M. & Selmi, S. (2005). Efficient polymer-nanocrystal quantum-dot photodetectors. *Applied Physics Letters*.

Rajabi, M., Dariani, R. & Zad, A. I. (2012). {UV} photodetection of laterally connected ZnO rods grown on porous silicon substrate. *Sensors and Actuators A: Physical*, 180, 11 - 14. doi: http://dx.doi.org/10.1016/j.sna.2012.04.003.

Renn, M. J. (1998). Apparatuses and methods for maskless mesoscale material deposition. US Patent 7,485,345B2.

Renn, M. (2011a). Process Optimization. *AJ International Users Group Presentations*.

Renn, M. (2011b). New Materials and Processes for Aerosol Jet. *AJ International Users Group Presentations*.

Renn, M. (2007). Direct Write System. US Patent 7,270,844.

Research, B. (2012). *Printed Electronics: The Global Market*.

Rida, A., Yang, L., Vyas, R. & Tentzeris, M. M. (2009). Conductive Inkjet-Printed Antennas on Flexible Low-Cost Paper-Based Substrates for RFID and WSN Applications. *IEEE Antennas and Propagation Magazine*, 51(3), 13-23. doi: 10.1109/MAP.2009.5251188.

Rida, A., Shaker, G., Nasri, F., Reynolds, T., Nikolaou, S. & Tenzeris, M. (2010, Jan). Inkjet printing of dual band conformal antenna for use in wifi frequency bands. *2010 IEEE Radio and Wireless Symposium (RWS)*, pp. 65-67. doi: 10.1109/RWS.2010.5434212.

Roberts, R. & Tien, N. (2013). Multilayer passive RF microfabrication using jet-printed au nanoparticle ink and aerosol-deposited dielectric. *IEEE International Conference on Solid-State Sensors, Actuators and Microsystems*.

Samant, H., Jha, A. K. & Akhtar, M. J. (2015, Dec). Design of coplanar dual band resonator sensor for microwave characterization of dispersive liquids. *2015 IEEE MTT-S International Microwave and RF Conference (IMaRC)*, pp. 249-252. doi: 10.1109/IMaRC.2015.7411388.

Sang, L., Liao, M. & Sumiya, M. (2013). A Comprehensive Review of Semiconductor Ultraviolet Photodetectors: From Thin Film to One-Dimensional Nanostructures. *Sensors*, 13(8), 10482. doi: 10.3390/s130810482.

Sargent, E. (2012). Photodetectors: A sensitive pair. *Nature Nanotechnology Letters*.

Schepps, J. & Rosen, A. (2002). Microwave industry outlook - wireless communications in healthcare. *IEEE Transactions on Microwave Theory and Techniques*, 50(3), 1044-1045. doi: 10.1109/22.989992.

Seifert, T., Sowade, E., Roscher, F., Wiemer, M., Gessner, T. & Baumann, R. R. (2015). Additive Manufacturing Technologies Compared: Morphology of Deposits of Silver Ink Using Inkjet and Aerosol Jet Printing. *Industrial & Engineering Chemistry Research*, 54(2), 769-779. doi: 10.1021/ie503636c.

Sette, D., Blayo, A., Poulain, C. & Mercier, D. (2013, June). Silver nanoparticle inkjet printed 17 GHz filter. *2013 IEEE MTT-S International Microwave Symposium Digest (MTT)*, pp. 1-4. doi: 10.1109/MWSYM.2013.6697350.

Shaman, H., Almorqi, S., Haraz, O., Alshebeili, S. & Sebak, A. (2014, Dec). Millimeter-wave microstrip diplexer using elliptical open-loop ring resonators for next generation 5G wireless applications. *Proceedings of 2014 Mediterranean Microwave Symposium (MMS2014)*, pp. 1-4. doi: 10.1109/MMS.2014.7088988.

Sharafadinzadeh, N., Abdolrazzaghi, M. & Daneshmand, M. (2017, Sept). Highly sensitive microwave split ring resonator sensor using gap extension for glucose sensing. *2017 IEEE MTT-S International Microwave Workshop Series on Advanced Materials and Processes for RF and THz Applications (IMWS-AMP)*, pp. 1-3. doi: 10.1109/IMWS-AMP.2017.8247400.

Shimoda, T. & Kawase, T. (2004). All-polymer thin film transistor fabricated by high-resolution ink-jet printing. *IEEE International Solid-State Circuits Conference*.

Shirasaki, Y., Supran, G. J., Bawendi, M. G. & Bulovic, V. (2012). Emergence of colloidal quantum-dot light-emitting technologies. *Nature Photonics*.

Siden, J., Fein, M. K., Koptyug, A. & Nilsson, H. E. (2007). Printed antennas with variable conductive ink layer thickness. *IET Microwaves, Antennas Propagation*, 1(2), 401-407. doi: 10.1049/iet-map:20060021.

Sirringhaus, H., Kawase, T., Friend, R. H., Shimoda, T., Inbasekaran, M., Wu, W. & Woo, E. P. (2000). High-Resolution Inkjet Printing of All-Polymer Transistor Circuits. *Science*.

Soltman, D. & Subramanian, V. (2008). Inkjet-Printed Line Morphologies and Temperature Control of the Coffee Ring Effect. *ACS Langmuir*.

Sondergaard, R. R., Hosel, M. & Krebs, F. C. (2013). Roll-to-Roll fabrication of large area functional organic materials. *Journal of Polymer Science Part B: Polymer Physics*, 51(1), 16–34.

Subramanian, V. & et al. (2008, Sept). Printed electronics for low-cost electronic systems: Technology status and application development. *ESSDERC 2008. 38th European*, pp. 17-24. doi: 10.1109/ESSDERC.2008.4681691.

Subramanian, V., Chang, J., Vornbrock, A. d. l. F., Huang, D., Jagannathan, L., Liao, F., Mattis, B., Molesa, S., Redinger, D., Soltman, D., Volkman, S. & Zhang, Q. (2008, Sept). Printed electronics for low-cost electronic systems: Technology status and application development. *Solid-State Device Research Conference, 2008. ESSDERC 2008. 38th European*, pp. 17-24. doi: 10.1109/ESSDERC.2008.4681691.

Suganuma, K. (2014). *Introduction to Printed Electronics*. Springer New York. Consulted at https://books.google.ca/books?id=7HG8BAAAQBAJ.

Sze, S. & Ng, K. (2006). *Physics of Semiconductor Devices*. Wiley. Consulted at https://books.google.ca/books?id=o4unkmHBHb8C.

Tantec. (2019). *What is surface treatment?* Consulted at https://tantec.com/what-is-surface-treatment.html.

Thompson, B. & Yoon, H. (2013). Aerosol-Printed Strain Sensor Using PEDOT:PSS. *IEEE Sensors Journal*.

Threm, D., Gugat, J., Pradana, A., Radler, M., Mikat, J. & Gerken, M. (2012). Self-Aligned Integration of Spin-Coated Organic Light-Emitting Diodes and Photodetectors on a Single Substrate. *IEEE Photonics Technology Letters*.

Torun, H., Top, F. C., Dundar, G. & Yalcinkaya, A. D. (2014, Aug). A split-ring resonator-based microwave sensor for biosensing. *2014 International Conference on Optical MEMS and Nanophotonics*, pp. 159-160. doi: 10.1109/OMN.2014.6924571.

Tseng, H. Y. & Subramanian, V. (2009, Dec). All inkjet printed self-aligned transistors and circuits applications. *2009 IEEE International Electron Devices Meeting (IEDM)*, pp. 1-4. doi: 10.1109/IEDM.2009.5424343.

Varenne, C., Mazet, L., Brunet, J., Wierzbowska, K., Pauly, A. & Lauron, B. (2008). Improvement in lifetime of pseudo-Schottky diode sensor: Towards selective detection of {O3} in a gaseous mixture (O3, NO2). *Thin Solid Films*, 516(8), 2237 - 2243. doi: http://dx.doi.org/10.1016/j.tsf.2007.08.008.

Velez, P., Su, L., Grenier, K., Mata-Contreras, J., Dubuc, D. & Martin, F. (2017). Microwave Microfluidic Sensor Based on a Microstrip Splitter/Combiner Configuration and Split Ring Resonators (SRRs) for Dielectric Characterization of Liquids. *IEEE Sensors Journal*, 17(20), 6589-6598. doi: 10.1109/JSEN.2017.2747764.

Verheecke, W., Dyck, M. V., Vogeler, F., Voet, A. & Valkenaers, H. (2012). Optimizing aerosol jet printing of silver interconnections on polyimide film for embedded electronics applications. *International DAAAM Baltic Conference*.

Verilhac, J. (2012, Sept). Recent developments of solution-processed organic photodetectors. *2012 International Semiconductor Conference Dresden-Grenoble (ISCDG)*, pp. 101-106. doi: 10.1109/ISCDG.2012.6359980.

Wang, F.-X., Lin, J., Gu, W.-B., Liu, Y.-Q., Wu, H.-D. & Pan, G.-B. (2013). Aerosol-jet printing of nanowire networks of zinc octaethylporphyrin and its application in flexible photodetectors. *Chem. Communications*.

Wang, Z. L. (2004). Zinc oxide nanostructures: growth, properties and applications. *Journal of Physics: Condensed Matter*, 16(25), R829. Consulted at http://stacks.iop.org/0953-8984/16/i=25/a=R01.

Winarski, D. J., Kreit, E., Heckman, E. M., Flesburg, E., Haseman, M., Aga, R. S. & Selim, F. A. (2018). Photoconductive ZnO Films Printed on Flexible Substrates by Inkjet and Aerosol Jet Techniques. *Journal of Electronic Materials*, 47(2), 949–954.

Wu, J. & Lin, L. Y. (2014). Inkjet Printable Flexible Thin-Film NCQD Photodetectors on Unmodified Transparency Films. *IEEE Photonics Technology Letters*.

Xia, Y., Zhang, W., Ha, M., Cho, J. H., Renn, M. J., Kim, C. H. & Frisbie, C. D. (2010). Printed Sub-2 V Gel-Electrolyte-Gated Polymer Transistors and Circuits. *Wiley Advanced Functional Materials*.

Xia, Z., Eftekhar, A. A., Soltani, M., Momeni, B., Li, Q., Chamanzar, M., Yegnanarayanan, S. & Adibi, A. (2011). High resolution on-chip spectroscopy based on miniaturized microdonut resonators. *Optics Express*.

Xu, K., Liu, Y., Chen, S., Zhao, P., Peng, L., Dong, L., Dong, L. & Wang, G. (2018). Novel Microwave Sensors Based on Split Ring Resonators for Measuring Permittivity. *IEEE Access*, 1-1. doi: 10.1109/ACCESS.2018.2834726.

Yadav, H. K., Sreenivas, K. & Gupta, V. (2007). Enhanced response from metal/ZnO bilayer ultraviolet photodetector. *Applied Physics Letters*, 90(17). doi: http://dx.doi.org/10.1063/1.2733628.

Yang, Z., Wang, M., Song, X., Yan, G., Ding, Y. & Bai, J. (2014). High-performance ZnO/Ag Nanowire/ZnO composite film UV photodetectors with large area and low operating voltage. *J. Mater. Chem. C*, 2, 4312-4319. doi: 10.1039/C4TC00394B.

Zarifi, M. H., Deif, S., Abdolrazzaghi, M., Chen, B., Ramsawak, D., Amyotte, M., Vahabisani, N., Hashisho, Z., Chen, W. & Daneshmand, M. (2018). A Microwave Ring Resonator Sensor for Early Detection of Breaches in Pipeline Coatings. *IEEE Transactions on Industrial Electronics*, 65(2), 1626-1635. doi: 10.1109/TIE.2017.2733449.

Zarifi, M. H. & Daneshmand, M. (2015). Non-Contact Liquid Sensing Using High Resolution Microwave Microstrip Resonator. *IEEE MTT-S International Microwave Symposium*.

Zhou, J., Gu, Y., Hu, Y., Mai, W., Yeh, P.-H., Bao, G., Sood, A. K., Polla, D. L. & Wang, Z. L. (2009). Gigantic enhancement in response and reset time of ZnO UV nanosensor by utilizing Schottky contact and surface functionalization. *Applied Physics Letters*, 94(19). doi: http://dx.doi.org/10.1063/1.3133358.

Zhou, L., Zhuang, J., Song, M., Su, W. & Cui, Z. (2014). Enhanced performance for organic light-emitting diodes by embedding an aerosol jet printed conductive grid. *Journal of Physics D: Applied Physics*.

Zwick, T., Chandrasekhar, A., Baks, C. W., Pfeiffer, U. R., Brebels, S. & Gaucher, B. P. (2006). Determination of the complex permittivity of packaging materials at millimeter-wave frequencies. *IEEE Transactions on Microwave Theory and Techniques*, 54(3), 1001-1010. doi: 10.1109/TMTT.2005.864140.